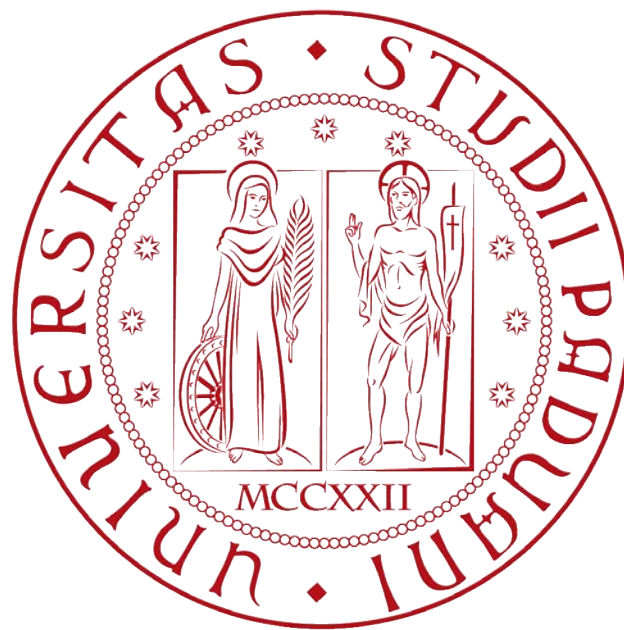# Università degli studi di Padova

Dipartimento di ingegneria industriale

Corso di Laurea Magistrale in Ingegneria dell'Energia Elettrica

Tesi di laurea magistrale

A novel power control strategy for induction cooktops designed by means of analytical, circuital and FEM modelling

Relatore: Prof. Fabrizio Dughiero

Laureando: Dissegna Filippo
N° di matricola: 1139722

Anno accademico 2018/2019

Se non puoi essere un pino sulla vetta del monte,
sii una canna nella valle,
ma sii la migliore piccola canna sulla sponda del ruscello.
Sii sempre il meglio di ciò che sei.
Cerca di scoprire il disegno che sei chiamato ad essere,
poi mettiti a realizzarlo nella vita.

Martin Luter king, da una poesia di Douglas Malloch

Sommario

La tecnologia di riscaldamento ad induzione è diventata molto utilizzata negli anni più recenti. Ad oggi è stata applicata in molte applicazioni mediche, industriali e domestiche. Il principio di funzionamento è basato sull'effetto che hanno le correnti indotte in un materiale ferromagnetico investito da un campo magnetico alternato ad alta frequenza. Tali correnti, scorrendo nel materiale, sviluppano calore per effetto joule.

I principali vantaggi di un sistema di riscaldamento ad induzione sono:

- alta efficienza di trasferimento del calore, che è generato direttamente all'interno del carico;
- elevata velocità di riscaldamento;
- sicurezza: non sono coinvolte fiamme o processi di combustione;
- pulizia, in quanto non sono previsti residui di combustione nel processo;

L'obiettivo principale di questa tesi è quello di studiare e proporre nuovi, veloci e accurati metodi per il design e la modellizzazione del funzionamento di un piano cottura, con focalizzazione sull'inverter, induttore e carico, che rapresentano la parte più importante del sistema.

Il diagramma a blocchi di un sistema di riscaldamento ad induzione è rappresentarto in figura 1.
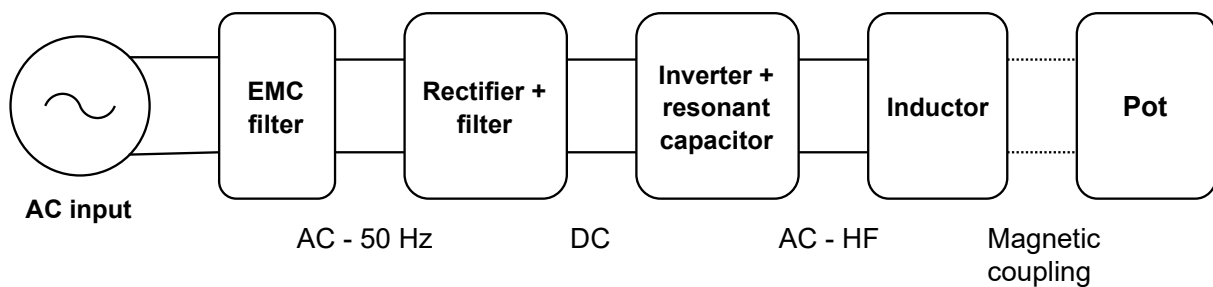

Figure 1: Block diagram of a domestic induction cooking appliance

I modelli FEM elettromagnetici rappresentano una accurata soluzione per la modellizzazione ed analisi del sistema, ma in molti casi richiedono tempi di computazione molto lunghi, anche delle decine di ore. L'approccio intrapreso in questo lavoro di tesi è quello di utilizzare il software FEM nel modo più essenziale cercando di sfruttare poi i modelli circuitali in implementati in Matlab e Simulink dove il tempo di computazione può essere estremamente ridotto.

Quando la quantità di calore richiesta è bassa, la maggior parte dei piani cottura in commercio utilizza una strategia di alimentazione discontinua, di tipo on-off: una potenza di valore medio viene fornita a intervalli di tempo regolari di 4-6 secondi. Lo svantaggio di questa tecnica, però, è che l'utente può notare un'andamento discontinuo del processo di bollitura dell'acqua o del

sugo che sta cuocendo. Con le metodologie sviluppate, si è voluto progettare un controllo che riesca ad evitare un'alimentazione discontinua nel basso range di potenze, tramite una particolare gestione del timing dei transistor nell'inverter.

Un'altro prodotto di questa tesi è stata la modellizzazione e l'upgrade di un concetto innovativo di pentola per piani cottura ad induzione brevettato dall'università di Padova. Le principali caratteristiche sono la presenza di pareti termicamwnte isolanti e la possibilità di alimentarie dei dispositivi ausiliari tramite un trasferimento wireless di energia tra l'induttore del piano cottura e un avvolgimento secondario posto attorno al fondo della pentola.

Nel primo capitolo, vengono presentate le caratteristiche, i pro e i contro del riscaldamento ad induzione, nonchè la struttura e il principio di funzionamente del sistema comprendente il piano cottura e la pentola.

Nel secondo capitolo, l'elettronica di potenza presente nei piani cottura è stata approfonditamente analizzata, a partire dai filtri per le emissioni elettromagnetiche (EMI), passando per il raddrizzatore e concentrandosi poi sul componente principale, che è l'inverter. Vari tipi possono essere presenti in un piano cottura, variando il numero di switch presenti all'interno, da 1 fino a 4. In tutti le forme d'onda sul carico sono state ricavate per via analitica e confrontate poi con una simulazione circuitale fatta su Simulink, dove è stato implementata anche la presenza di un eventuale lossless snubber, che in alcuni tipi di inverter permette di ridurre drasticamente le perdite di switching. Le grandezze del funzionamento a regime sono state ottenute mediante metodi iterativi studiati appositamente per ogni tipo di convertitore.

Nel terzo capitolo, l'analisi si è spostata nel sistema induttore-carico. Differenti tecniche di modellazione sono state investigate. Il sistema può essere visto come una semplice serie di un induttore e un resistore. I valori di tali elementi però, racchiudono al loro interno una molteplicità di fenomeni che non è facile modellizzare accuratamente. Dopo una spegazione del background teorico che sta alla base dell'accoppiamento induttore-carico, un metodo analitico di calcolo dell'impedenza equivalente, ma anche delle correnti indotte sulla pentola, è presentato, e i risultati comparati con una simulazione agli elementi finiti. Successivamente, per tener conto della saturazione del materiale con cui è fatta la pentola, è stato sviluppato un metodo iterativo che mira alla ricerca di una permeabilità equivalente uniforme. I risultati ottenuti sono poi adeguatamente corroborati e discussi nella parte finale del capitolo.

Nel quarto capitolo, utilizzando le conoscenze acquisite durante la prima parte del lavoro, sono state analizzate le strategie di controllo adottabili per variare la potenza nel carico con un inverter a mezzo ponte. Dettagliate spiegazioni delle varie fasi del funzionamento sono fornite. Nella seconda parte è stato sviluppato (combinando i tipi di controllo analizzati) un controllo di potenza che permetta di raggiungere i più bassi livelli senza utilizzarne uno di tipo discontinuo, che possa far percepire all'utente un bollore e/o temperatura non uniforme nel tempo.

Nel quinto capitolo, l'analisi si è spostata allo studio e modellizzazione di un concetto di pentola che aggiunga la possibilità di alimentare in modo wireless dei dispositivi ausiliari quali mescolatori, lampade ad infrarosso e pompe a vuoto, inserendo una bobina attorno al fondo della pentola. Inoltre, la parte esterna della pentola è costituita di materiale termicamente isolante. È stato quindi definito e validato un modello circuitale che includa insieme il sistema wireless (trasformatore con nucleo in aria) assieme al fondo magnetico della pentola, dove comunque viene dissipata la maggior quantità di potenza. In seconda fase poi il circuito è stato utilizzato per dimensionare un sistema di conversione di potenza che permetta di ottenere 13 V - 30 W in continua per l'alimentazione di una batteria e di una pompetta a vuoto, indipendentemente dalla frequenza e potenza di alimentazione dell'induttore del piano

cottura, attraverso il dimensionamento di un raddrizzatore, di un convertitore DC/DC e di un controllore PID.

Nel sesto e ultimo capitolo, sono tratte le conclusioni e osservazioni di carattere generale sul lavoro di tesi e sono elencati i possibili scenari futuri di maggior trend su cui saranno focalizzati gli studi relativi al riscaldamento ad induzione in ambito domestico.

Abstract

The main target of this thesis is to provide new, fast and accurate methodologies to model and analyse the operation of a domestic hob, with a focus on the inverter, inductor and load, which represent the cornerstone of all the induction heating systems.

Electromagnetic FEM models are very accurate and straightforward solutions to analyse and design the system, but it can also be very time consuming. The main approach carried out in this thesis tries to make an essential use of the FEM software and exploit as much as possible the use of circuital model implemented in Matlab and Simulink where the computation requires very few amount of time: iterative methods are often used in order to take into account the variations of the parameters in the model.

When low load power level is required, the supply of the most domestic cooktops becomes discontinuous, which means that the user can experience boiling pulses or at least an oscillating temperature value in food. The methodologies for the analysis and modelling developed in the second and third chapter are then used to design a novel power control strategy, which includes a continuous low power supply of the inductor, in order to avoid temperature and boiling pulses, by means of a particular timing management of the switches in the inverter.

In the last chapter, the acquired knowledge is applied to design a model for an innovative concept of pot, patented by the University of Padua. Then a rectifier and a controlled DC/DC buck converter have been designed and simulated. The aim is to supply some auxiliary devices by means of an energy wireless transfer between the inductor in the hob and a secondary coil placed around the bottom of the pan.

Contents

Chapter 1

Introduction

Induction heating technology has become widely popular in recent years. It is nowadays the heating method that has been successfully applied in many industrial, domestic, and medical applications [1]. The working principle of this way of heating is based on the heating effect that eddy currents flow causes in the induction target, that must be made of magnetic material with relatively high resistivity. To obtain this effect, an alternate, high-frequency current flows in a coil (inductor) that generate a time-varying magnetic field. When an object made of ferromagnetic material is placed inside this magnetic field, eddy currents will start to flow, heating it up, due to the joule effect.

Special features of induction heating are:

- efficiency of heat transfer: the heat is generated directly into the workpiece, leading to a 90% overall efficiency of the process. Moreover, since the heat is generated directly inside the workpiece, heat losses in the surrounding environment are reduced;
- fast heating: considerable heat density can be generated inside the load;
- safety: no open flames are involved in the process;
- cleannes: no burned residuals are developed in the process;

In addition, a lot of improvements have been made in power electronics and magnetic component design, leading to high reliable and cost-effective process.

As already mentioned in the abstract, this thesis focuses in the domestic application of induction heating: induction cooking. Traditional gas cookers are going to being replaced more and more these years, since induction hobs can assure the aforementioned advantages. The external aspect of an induction hobs compared to a traditional gas cooker is showed in figure 1.1.

Lots of advantages already described for a general heating system can be applied specifically for a domestic induction cooking process. In addition the flat glass-based induction cooktop is an attractive addition to any kitchen, especially compared to a gas cooker. Moreover, cleaning a conventional gas burner is definitely more difficult and tricky compared to cleaning a flat vitroceramic glass. Howewer, some drawbacks can be listed:

- cost: since induction is still a relatively new technology, an induction cooktop is going to cost more than the same-sized traditional cooktop;
- special cookware is required: magnetic cookware must be used or the induction process won't work correctly and the food won't cook. this may require investing in cookware as well as the induction cooktop;

<table>
<tr><td>(a) Induction hob</td><td>(b) Gas cooker</td></tr>
</table>

Figure 1.1: Appearance comparison between induction hob and gas cooker in a domestic kitchen

- digital food termometer may not work: since an induction cooktop generates an electromagnetic field, the new digital thermometer technology may not be reliable. It can be necessary to use an old analog thermometer to ensure the meal is cooked at the right temperature.

A better view of external aspect of an induction hob can be seen in figure 1.2. It is mainly composed of a vitroceramic glass that includes some circular serigraphies to help the user centering the pan with the inductor (or to delimit a surface where the pan can be put freely in case of square serigraphies) and the user interface which allows the power transfer regulation and the use of some other minor features, like the timer or lock of the cooker settings.
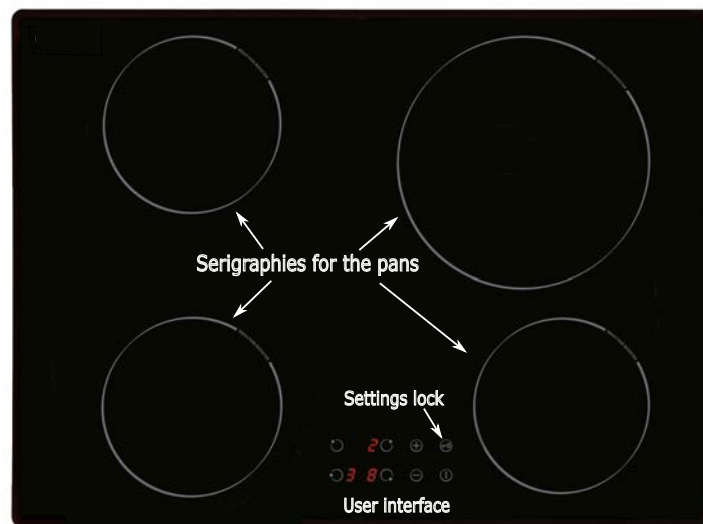
Figure 1.2: Top view of an induction hobs with 4 cooking zones

The block diagram of an induction cooking system is shown in figure 1.3. The mains AC-50 Hz voltage is firstly rectified and then filtered, supplying a DC bus. Then an inverter feeds with an AC high variable frequency (20-100 kHz) current the load which is composed by a capacitor and the inductor. The induction coil is magnetically coupled with the pan, that acts as a load for the system. An EMI filter is placed before the rectifier to reduce electromagnetic emissions.

AC input	EMC filter	Rectifier + filter	Inverter + resonant capacitor	Inductor	Pot
	AC - 50 Hz	DC	AC - HF	Magnetic coupling	

Figure 1.3: Block diagram of a domestic induction cooking appliance

Chapter 2

Power electronics stages

In this chapter, the description and the operation of the different power electronics stages that compose a domestic induction heating appliance will be investigated. The main part is the inverter: different topologies and modulation strategies can be used in order to supply the inductor. Analytical solutions and simulations have been done in order to fully understand the behaviour of different power electronic converters investigated.

2.1 Rectifier stage

After the input EMI filter, the rectifier is connected just afterwards. The circuit is shown in figure 2.1. It is a full bridge rectifier (also called *Graetz Bridge*) so there are 4 diodes and a filter capacitor C_f.The grid and the EMI filter are modelled as a resistance R_S in series with an inductance L_S. The load is a resistance R_L.
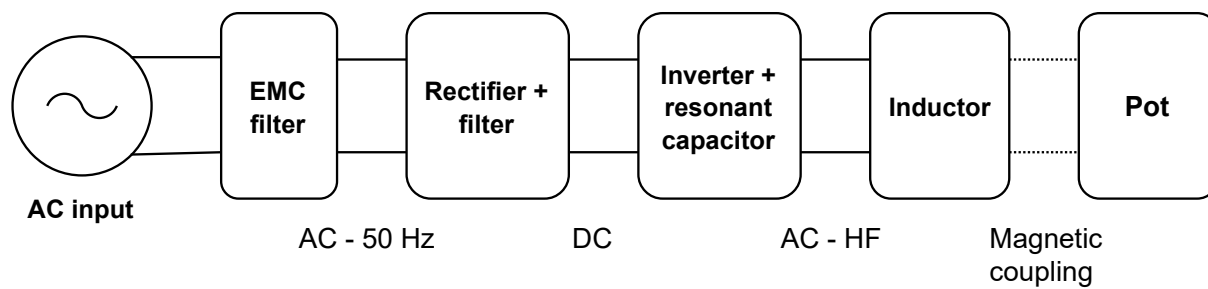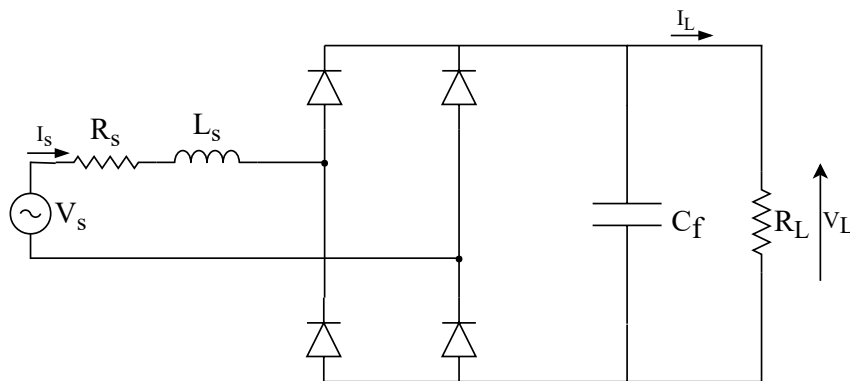

Figure 2.1: Circuit sketch for the rectifier and output filter

It is out of the scope of this thesis to provide a detailed explanation of the circuit (it should be known by the reader), but some simulation results will be provided. The circuit have been simulated with Simulink environment. Three different simulation results will be showed, with components value according to table 2.1. Each diode has a 0.7 V as fixed forward voltage and an on-resistance of 1 $m\Omega$.

As can be seen from the table above, the first simulation is without the input inductor and the output capacitor, while in the second and third simulation they are gradually inserted.

Table 2.1: Simulation references and rectifier specification

Simulation n	ref	$V_{s,rms}$ [V]	R_S [Ω]	L_S [mH]	C [mF]	R_L [Ω]
1	*nothing*	230	1	0	0	30
2	C	230	1	0	1.2	30
3	L_S, C	230	1	1	1.2	30

Components value are taken from some examples in [4]. The results are showed in figure 2.2 where one 50 *Hz* source period is showed.
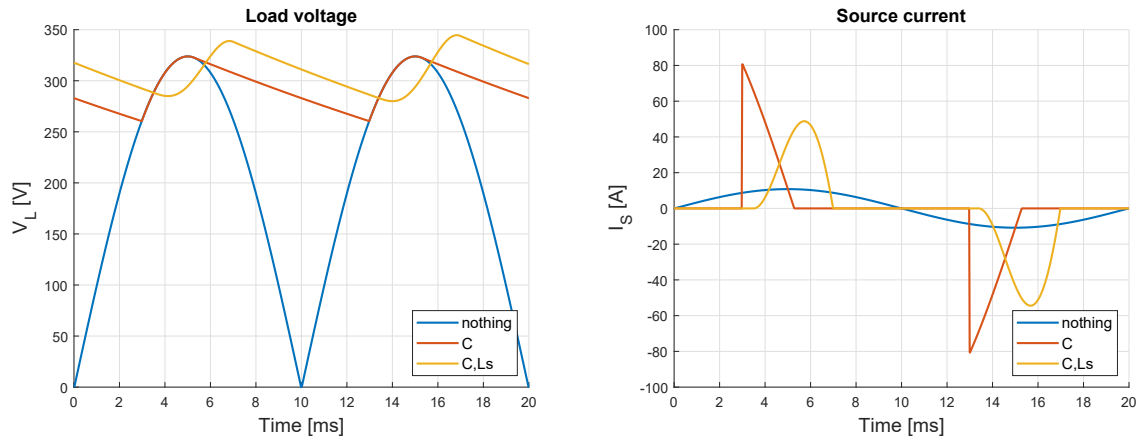
(a) Load voltage for different components value

(b) Source current for different components value

Figure 2.2: Rectifier simulations results

In order to derive some conclusions, in table 2.2 the mean output voltage together with the rms and peak current are showed.

Table 2.2: Simulation results about load voltage and source current

Simulation	V_l mean [A]	I_S rms [A]	I_S peak [A]
1	205.7	7.6	10.8
2	296.6	21.7	80.7
3	310.5	20.2	48.8

It can be concluded that:

- the use of the output capacitor helps improving the output voltage: higher and more flat. When it start charging the presence of a spike in the current is caused and the higher the capacitance, the more is the height of the spike. I_S becomes also discontinuous: when the capacitor voltage V_L is more than $|V_S|$ the load current comes only from the output capacitor.

- When the input inductance L_S is considered, an additional increase in the mean output voltage is obtained. The maximum value of the current is decreased compared to simulation n°2 where only the output capacitor is considered.

- The fundamental component of I_S is lagging behind V_S when L_S is present.

Generally talking, the higher the output capacitance value C_f, the higher is the output mean voltage; consequently, the spike in the current will increase as well and it will get more difficult to filter by EMI chokes. On the other hand, the higher is L_S, the lower is V_L but more stabilized.

2.2 Inverter stage

The aim of the inverter is to convert the input DC waveform in a medium/high frequency $(20 - 100\,kHz)$ voltage, that will be supplied to the load. Multiple topologies are used, depending on multiple factors: output power and cost for example. The mains inverter topology that can be used are essentially three and the main difference between them is the number of switch required for the operation:

- full-bridge topology: it is composed of 4 switches, see section 2.2.2

- half-bridge topology: it is composed of 2 switches, see section 2.2.3

- quasi-resonant topology: it is composed of 1 switch, see section 2.2.4

The most used inverter is the half bridge, due to a good compromise between cost and robustness [5]. Quasi resonant topology is used for low cost product, especially for Asiatic countries where induction heating appliances are designed for an output power of $2\,kW$ [1]. Full bridge topology is the most effective one for reaching high output power with low distortion level, but the cost of 4 switches makes this topology not very attractive for domestic purposes, therefore it is used mainly for industrial applications. More topologies are used for specific purposes, like reaching high efficiencies for examples, as can be seen in [6]

In the next sections each of the three topologies will be described with analytical models and simulations. The input will be a constant voltage source of 310 V, that is a possible average output from the rectifier, according to table 2.2. The output of the inverter is connected to the load (inductor + pot) that is modelled as an equivalent resistance R_{eq} and inductance L_{eq} which can be connected in series or in parallel. In this thesis a series connection will be considered. Together with the $R_{eq} - L_{eq}$ load, a capacitor C_r is connected (in series or parallel, again) to complete the resonant tank. In fact, the inverter works as a resonant converter: the self oscillation produced by the resonant load R_{eq}, $L_{eq}\,C_r$ is "used" in order to drastically decrease the switching losses of the inverter, achieving zero-voltage or zero-current switching (ZVS and ZCV respectively) depending on the topology. The equivalent load value will be just taken from some papers just to show how the inverter works, the load modelling process will be shown in chapter 3.

2.2.1 Resonant load analysis

For each inverter topology, the analytical formula for current and voltage in the load have been calculated. In this section the approach used will be shown as reference for what will be explained below. It consists mainly on solving an RLC series circuit similar to what shown in figure 2.3. The Kirchoff's voltage law for this circuit is (for the sake of brevity, R_{eq} is substitute by R, L_{eq} by L, C_r by C, I_L by I):
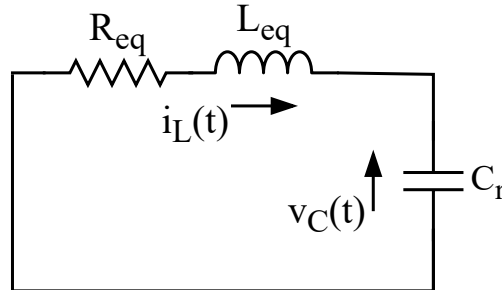
$$v_R(t) + v_L(t) + v_c(t) = 0 \tag{2.1}$$

Figure 2.3: Series RLC circuit diagram

Since $v_R = R\,i$, $v_L = \frac{di}{dt}$, $v_c(t) = v(t)$, equation 2.1 becomes

$$R\,i(t) + L\frac{di}{dt} + v(t) = 0 \tag{2.2}$$

Since $i(t) = C\frac{dv}{dt}$, after dividing all the equation by LC the final second order differential equation that describe the circuit is:

$$\frac{d^2v}{dt^2} + \frac{R}{L}\frac{dv}{dt} + \frac{1}{LC}v(t) = 0 \tag{2.3}$$

The solutions of the characteristic equation $s^2 + \frac{R}{L}s + \frac{1}{LC} = 0$ associated to eq. 2.3 are

$$s_{1/2} = -\alpha \pm \sqrt{\alpha^2 - \omega_0^2} \tag{2.4}$$

where two quantities have been defined:

$$\omega_0 = \frac{1}{\sqrt{(LC)}} \tag{2.5a}$$

$$\alpha = \frac{R}{2L} \tag{2.5b}$$

ω_0 is called *natural resonance frequency (rad/s)* which is the frequency at which an LC circuit would oscillate, without any damping factor. Depending on the value of $\alpha^2 - \omega_0^2$ the response of the circuit is different:

- $\alpha^2 - \omega_0^2 > 0$: overdamped case

- $\alpha^2 - \omega_0^2 > 0$: critical damped case

- $\alpha^2 - \omega_0^2 < 0$: underdamped case

In the induction heating context, the load equivalent parameters give always the underdamped one. The general solutions showed in 2.4 becomes

$$s_{1/2} = -\alpha \pm j\,\omega_d \tag{2.6}$$

where $\omega_d = \sqrt{\omega_0^2 - \alpha^2}$ is called *damped frequency* and it is the frequency of the resulting waveform: so, when a resistance is present toghether with C and L, the frequency of the voltage/current is no more ω_0 but ω_d that is slightly lower. The solution of the transient regime is

then:
$$v(t) = k_1 \, e^{s_1 \, t} + k_2 \, e^{s_2 \, t} = ... = e^{-\alpha \, t}[A_1 \, cos(\omega_d \, t) + A_2 \, cos(\omega_d \, t)] \quad A_1, A_2 \in \mathbb{R} \qquad (2.7)$$

That waveform is a sinusoidal damped function. The oscillating behaviour happens due to the energy exchange between capacitor and inductor that is dissipated through the resistance. A_1 and A_2 must be found using the boundary conditions of the system, like the starting capacitor voltage, or the starting inductor current value. The damping component $e^{-\alpha \, t}$ has a time constant of $1/\alpha$. One example of such underdamped behaviour is showed in figure 2.4 for the capacitor voltage: in this example the capacitor is precharged so even if the inductor is discharged (the initial current is zero) the oscillation can start.
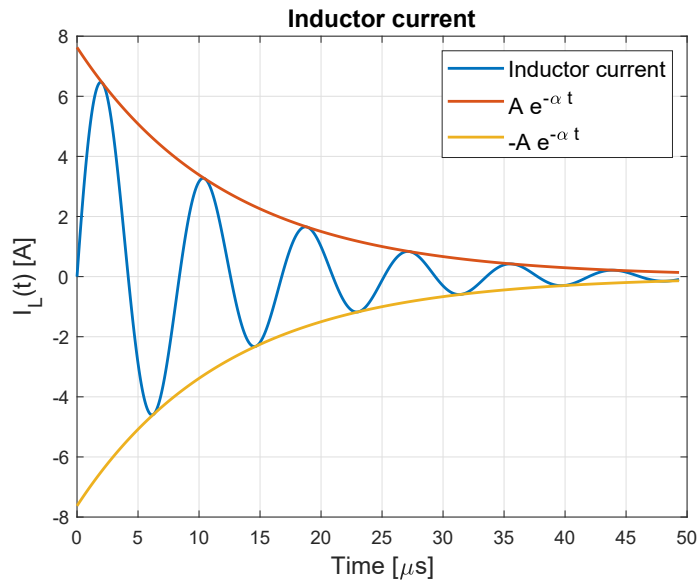
Figure 2.4: Example current waveform in a RLC underdamped circuit

When a source is present in the circuit, like a constant voltage generator, the total solution is the sum of the transient behaviour showed above with the steady-state value. For example, if a battery of value V_{dc} is placed in series with the RLC load, the steady-state regime ($t \to \infty$) will be:

$$v(\infty) = V_{dc} \qquad (2.8a)$$
$$i(\infty) = 0 \qquad (2.8b)$$

Once the capacitor voltage have been found (transient+steady state solution) the capacitor current is found knowing that $i(t) = C\frac{dv}{dt}$. Since the capacitor is in series with the inductor, capacitor current is also the inductor one.

2.2.2 Full-bridge topology

2.2.2.1 Introduction

The full bridge inverter consists of two legs, each comprising of two switches and their anti-parallel diodes. The two switches in each leg are switched in such a way that one of them is in its off state, while the other is switched on. Some literature about this topology can also be

found in [7], [8]. The circuit diagram is shown in figure 2.5. The value of the equivalent load is: $R_{eq} = 13\,\Omega$, $L_{eq} = 80\,\mu H$, $C_r = 300nF$ (taken from [7]) which gives $f_d = \frac{\omega_d}{2\pi} = 29.8\,kHz$.
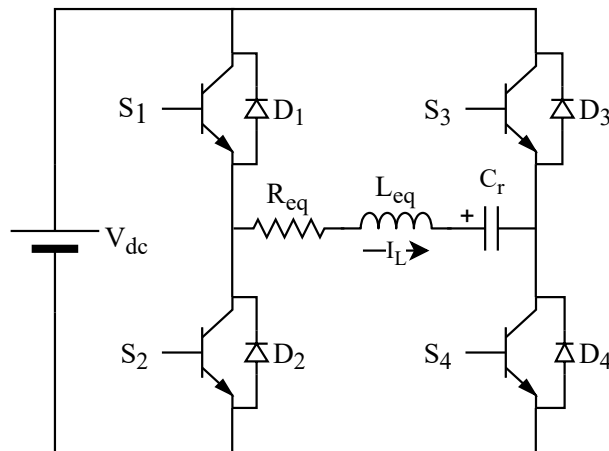
Figure 2.5: Circuit diagram of the full bridge inverter

The working operation of this inverter will be analyzed step by step considering the different state of the switches and the diodes. In figure 2.6 all the states are shown enhancing which components is working (continuous line) and which not (dotted line). In table 2.3 all the states are summarized. For each mode, the procedure to find the voltage/current waveforms of an RLC load described in section 2.2.1 will be performed.

(a) Mode A (b) Mode B (c) Mode C

(d) Mode D (e) Mode E (f) Mode F
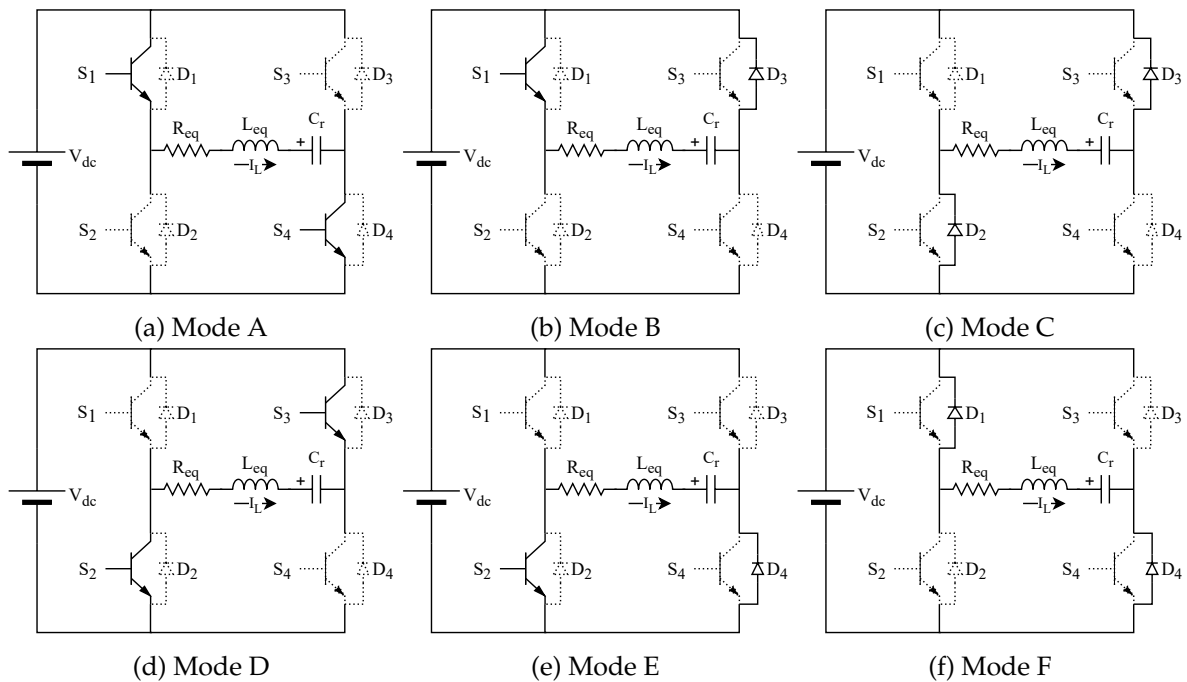
Figure 2.6: Operation modes of the resonant full-bridge inverter

2.2.2.2 Mode A: S$_1$ and S$_4$ On

Mode A (figure 2.6a) starts when I_L, that is increasing, becomes zero: its conduction move from D_1, D_4 to S_1, S_4 that have been switched on previuosly, achieving a ZVS turn on. Boundary

Table 2.3: Operations mode summary of the full-bridge inverter

MODE	I_L	S_1	S_2	S_3	S_4	D_1	D_2	D_3	D_4
A	> 0	x			x				
B	> 0	x						x	
C	> 0						x	x	
D	< 0		x	x					
E	< 0		x						x
F	< 0	x							x

conditions are:

$$v_c(0) = -V_{c0} \tag{2.9a}$$

$$i_L(0) = 0 \tag{2.9b}$$

One thing that must be underlined is that the time istant $t = 0$ is the beginning of a steady state period, not the time istant at which the circuit starts operating, the transient regime is already ended. So the capacitor voltage and inductor current analytical expressions for mode A are $(0 < t < t_1)$:

$$v_c(t) = V_{dc} - (V_{c0} + V_{dc}) e^{-\alpha t} [cos(\omega_d t) + \frac{\alpha}{\omega_d} sin(\omega_d t)] \tag{2.10a}$$

$$i_L(t) = \frac{V_{dc} + V_{c0}}{L_{eq} \omega_d} e^{-\alpha t} sin(\omega_d t) \tag{2.10b}$$

t_1 is the time istant when mode A ends, i.e. S_4 is opened. Considering the circuit as it is presented in figure 2.5, when S_4 switches off, since the current is still positive and so flowing into it, the switching is *hard*, with consequent switching losses. On the other hand, this turn-off losses are drastically reduced by using a lossless snubber, see section 2.2.2.5. V_{c1} and I_1 are the capacitor voltage and inductor current at the time t_1.

2.2.2.3 Mode B: S_1 and D_3 On

Since the current is still positive and S_4 is off, D_3 will conduct. In this phase, the capacitor is charging but the current is decreasing. The analytical expressions for voltage and current are found by using the boundary condition at time $t_1 (t_1 < t < t_2)$:

$$v_c(t) = e^{-\alpha(t-t_1)} [V_{c1} cos(\omega_d(t - t_1)) + \frac{1}{\omega_d}(\alpha V_{c1} + \frac{I_1}{C_r}) sin(\omega_d(t - t_1))] \tag{2.11a}$$

$$i_L(t) = e^{-\alpha(t-t_1)} [I_1 cos(\omega_d (t - t_1)) - \frac{1}{\omega_d}(\alpha I_1 + \frac{V_{c1}}{L_{eq}}) sin(\omega_d(t - t_1))] \tag{2.11b}$$

t_2 is the time instant when mode A ends, i.e. S_1 is opened. It is important that i_L is still positive allowing diodes D_2 to conduct: in this situation also S_2 will have a ZVS turn-on. V_{c2} and I_2 are the capacitor voltage and inductor current at the time t_2.

2.2.2.4 Mode C: D_2 and D_3 On

Both diodes are conducting, since the current is positive and both switches are turned off. The current is decreasing while the capacitor is reaching the maximum voltage. The analytical expressions for voltage and current are found by using the boundary conditions at time $t_2(t_2 < t < t_3)$:

$$v_c(t) = -V_{dc} + e^{-\alpha(t-t_2)}\left[(V_{dc} + V_{c2})\cos(\omega_d(t-t_2))+ \right. \tag{2.12a}$$
$$\left. \frac{1}{\omega_d}[\alpha(V_{dc} + V_{c2}) + \frac{I_2}{C_r}]\sin(\omega_d(t-t_2))\right]$$

$$i_L(t) = e^{-\alpha(t-t_2)}\left[I_2\cos(\omega_d(t-t_2)) - \frac{1}{\omega_d}(\alpha\, I_2 + \frac{V_{dc} + V_{c2}}{L_{eq}})\sin(\omega_d(t-t_2))\right] \tag{2.12b}$$

Mode E ends when the current reaches zero at time t_3 which can be found by solving the equation 2.12b $i_L(t_3) = 0$ which gives:

$$t_3 = \frac{1}{\omega_d}\,atan\left(\frac{\omega_d\, I_2}{\alpha\, I_2 + \frac{V_{dc}+V_{c2}}{Leq}}\right) + t_2 \tag{2.13}$$

once t_3 have been found, the switching frequency is $f_s = \frac{1}{2\,t_3}$.

2.2.2.5 Overall considerations

The switching frequency f_s is determined by the value of t_1 and t_2 when S_4 and S_1 are respectively switched off: the earlier are the two transistors turned off, the higher will be the switching frequency. As can be understood, $f_s > f_d$ in order to have a ZVS turn-on. With the load value already mentioned, with $t_1 = \frac{1}{4.5\,f_d}$ and $t_2 = \frac{1}{3.5\,f_d}$, a steady state solution of half period is showed in figure 2.7. As can be seen, $V_{c0} = 253.5\,V$: to find the steady state value, an iterative process have been used:

1. A first attempt value of V_{c0} is set.

2. $v_c(t)$ is calculated for $0 < t < t_3$

3. If steady state regime is achieved, $v_c(t_3) = -v_c(0)$, if not, $-v_c(t_3)$ is used as V_{c0} and the process starts again from step n°2.

4. When $v_c(t_3) + v_c(0) < threshold$, the steady state value of V_{c0} is found. In this case, the threshold value is set to 0.1 V. The more is the threshold value small, the more V_{c0} is accurate.

The graphic result of the calculation for half period is shown in figure 2.7.

One full period of the resulting waveform can be seen in figure 2.8. The second half period is the opposite sign of the first one due to the symmetry of the circuit and the driving technique. This is valid because the duty cycle of opposite switches S_1 and S_4, along with S_2 and S_3, is the same. When the inverter control is not symmetric anymore, the full period must be studied.

It's worth saying that mode B or D are not mandatory: if $t_1 = t_2$ that modes are not present but the inverter can work in any case, and all the switches work symmetrically. In the example showed above, the duty cycle for switches 1 and 2 is $D_{12} = \frac{t_3}{2\,t_3} = 0.5$, while for S_3 and S_4
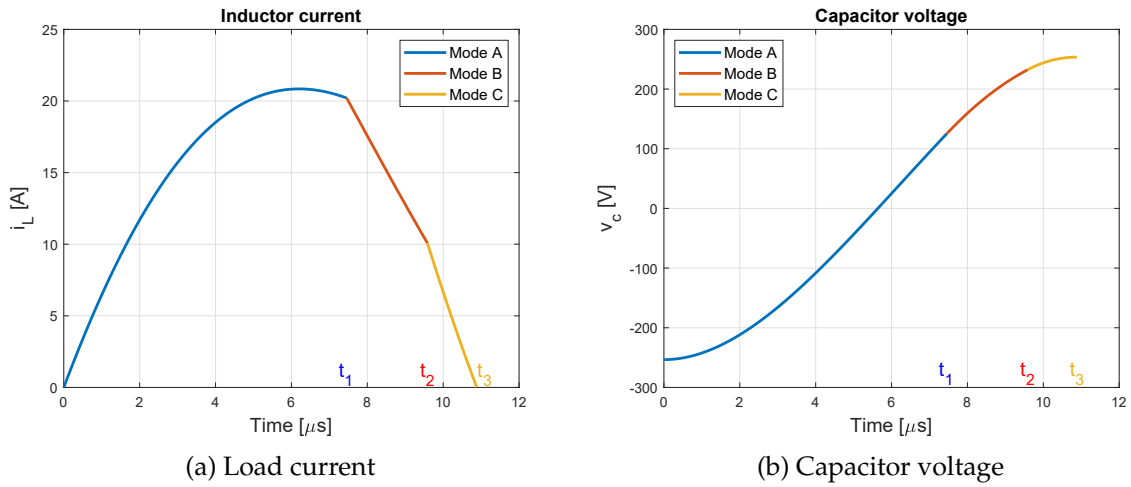
(a) Load current   (b) Capacitor voltage

Figure 2.7: Half period calculated full-bridge waveforms, with $t_1 = \frac{1}{4.5\,f_d}$ and $t_2 = \frac{1}{3.5\,f_d}$, $V_{c0} = 253.5\,V$.

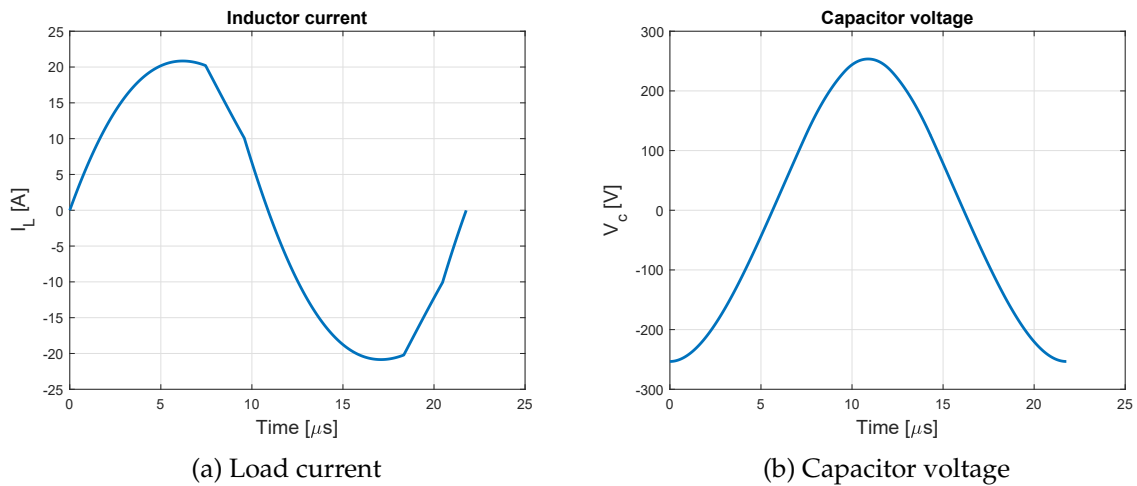(a) Load current   (b) Capacitor voltage

Figure 2.8: One period calculated full-bridge waveforms, with $t_1 = \frac{1}{4.5\,f_d}$ and $t_2 = \frac{1}{3.5\,f_d}$, $V_{c0} = 253.5\,V$.

is $D_{34} = \frac{t_1 + (t_3 - t_2)}{2\,t_3} = 0.402$. If $t_1 = t_2$ all the switches have a duty cycle of 0.5. A full-bridge model have been created in Simulink too. With the same parameters as the analytical model ($t_1, t_2, load...$) the simulation gives exactly the same results. On the other hand, the simulation is useful to investigate how the lossless snubber works. In fact, as already mentioned, if the circuit is built as showed in figure 2.5, all the turn off periods cause losses in the switch, since a certain amount of current is flowing through the switch that must "transfer" all the current to the antiparallel diode of the other switch in the same leg: during this process both current and voltage across the transistor aren't zero so an amount of power is lost during the switching. This is also why a suitable deadtime is required between the turn off of one switch and the turn on of the other switch in the same leg. For further details about hard commutation, see [4]. A lossless snubber is just a capacitor of suitable value that is placed in parallel to each switch, as shown in figure 2.9. Its task is to maintain the voltage limited across the switch during the turn off time in such a way that the switching losses are drastically reduced.
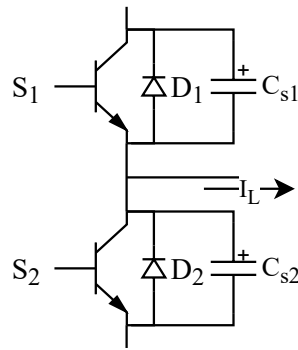
Figure 2.9: Lossless snubber applied to an inverter leg

When the off signal is sent to the gate of the switch, it takes the *turn off time* before in order that no current is flowing anymore. Meanwhile, the capacitor starts charging through the load current while the lossless snubber of the other switch (same leg) starts discharging. If the charging time is quite higher compared to the turn off time, very few volts fall across the switch that is turning on. It is worth underlying that the use of the lossless snubber can be done theoretically only if $f_s > f_d$ but in practice is used only when $f_s > f_0$. On the other hand, some requirements must be satisfied to assure a correct switching phase:

- A sufficient amount of output current must be flowing at the switching time in order to discharge one capacitor from rail voltage (V_{dc}) to zero and at the same time to charge the opposite capacitor.

- Sufficient deadtime must be considered in order to completely charge/discharge the capacitors.

In figure 2.10 two examples of commutation with a snubber $C_s = 35\,nF$ are showed:

- In figure 2.10a the output current at the time when the switch is turned off is not enough to complete the charging of C_{s2} and the discharging of C_{s1}. As can be seen, the voltage across the switch (i.e. the snubber voltage) reach its minimum when the output current goes to zero. Once (at the end of the deadtime) the gate signal of S_1 goes to 1, the voltage across the switch is forced to be zero but since C_{s1} is not completely discharged, a huge spike of current involve the switch (instantaneous discharge of C_s through the transistor).

- In figure 2.10b soft commutation is not happening because the deadtime is not enough to allow the complete commutation to rail voltage of C_{s2} and the full discharging of C_{s1}, in fact it can be seen that the voltage reaches a certain value lower than V_{dc}, which is reached only after the deadtime, when the gate signal force the switch to conduct. Also in this situation a spike in the current can be seen when the switch turns on.

Supposing that the output current is constant ($I_L = i_L(t_2)$) during deadtime, a formula for its minimum value can be found. During the deadtime is necessary an amount of charge equal to $2\,C_s\,V_{dc}$ necessary to completely "swap" the voltage between the two snubbers. So the charge balance is:

$$I_L\,t_{dt} = 2\,C_s\,V_{dc} \tag{2.14}$$

So the minimum deadtime required is:

$$t_{dt,min} = \frac{2\,C_s\,V_{dc}}{I_L} \tag{2.15}$$

(a) Insufficient amount of output current,
$t_1 = t_2 = \frac{1}{2.4\, f_d}$, $t_{dt} = 2.5\,\mu s$

(b) Insufficient dead-time,
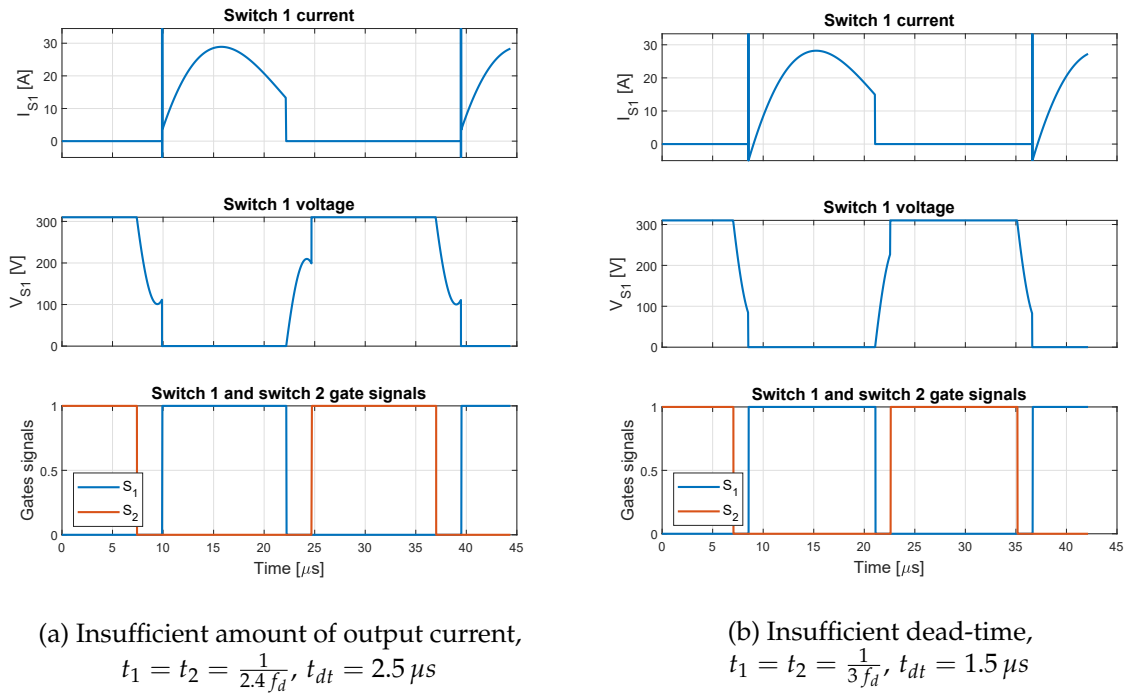$t_1 = t_2 = \frac{1}{3\, f_d}$, $t_{dt} = 1.5\,\mu s$

Figure 2.10: Examples of hard commutations with snubber capacitors $C_s = 35\,nF$

Actually, the current during deadtime is decreasing and not constant, so less charge is removed from capacitors compared to the case where the current $i_L(t)$ is constant, this is why the deadtime value found with equation 2.15 is the minimum, higher value must be taken. More complex formulation to find an exact value of deadtime to set can be found in the literature, for example in [9].

In addition, deadtime mustn't be too high, because the switch must be turned on while its antiparallel diode is still conducting. If t_{dt} is too high, the current reaches zero value before the switch turns on, so the diodes conduction is ended (no ZVS available anymore) and the capacitor starts charging again, then when the gate signal comes to the switch, it will short-circuit a capacitor that is partially charged (short circuit).

2.2.3 Half-bridge topology

2.2.3.1 Introduction

The half bridge inverter circuit consists of one leg. Several topics that have been covered in section 2.2.2 are very similar and valid also for this inverter topology. There are two possible circuital configurations, depending on how the resonant capacitor(s) is connected, as shown in figure 2.11. The resonant capacitor C_r can be connected in series with the load or split in two equal capacitance $C_r/2$ which are connected between the load and the DC bus.

There are no such big differences between the two circuits. In fact, in figure 2.11b the two resonance capacitors are in parallel so the equivalent capacitance "seen" by the load is C_r, so the load current is exactly the same if the two circuits of figure 2.11 are compared. The configuration with two resonant capacitor is preferred because the current equally splits between them and return through the DC link. But, since we are interested mainly in the inductor current, in the

(a) One resonant capacitor
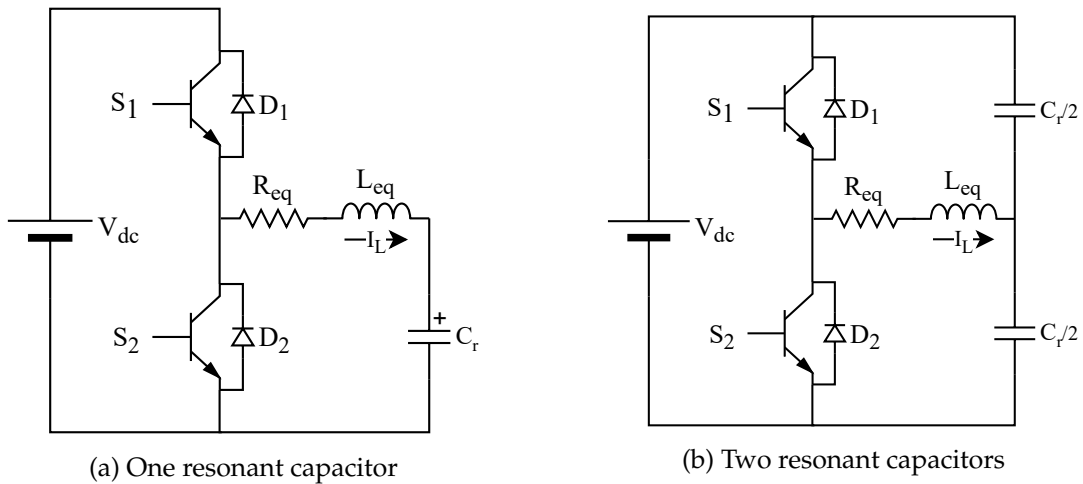
(b) Two resonant capacitors

Figure 2.11: Circuit diagrams of the half bridge inverter

analytical solution the circuit of figure 2.11a will be considered. The analysis of the converter will be done similarly to what already done with the full bridge inverter. The value of the equivalent load is the same used for the full bridge: $R_{eq} = 13\,\Omega$, $L_{eq} = 80\,\mu H$, $C_r = 300nF$ which gives $f_d = \frac{\omega_d}{2\pi} = 29.8\,kHz$.

The working operation of this inverter will be analysed step by step considering the different states of switches and diodes. In figure 2.12 all the states are showed enhancing which components is working (continuous line) and which not (dotted line). Compared to what have been done with the full bridge a slightly different approach have been used, the switch state won't be separated from its antiparallel diode one, so a unique mode will be considered when the current flow first in the diode and then in its switch. In table 2.4 all the states are summarized. For each mode, what already described in section 2.2.1 will be done.

(a) Mode A

(b) Mode B
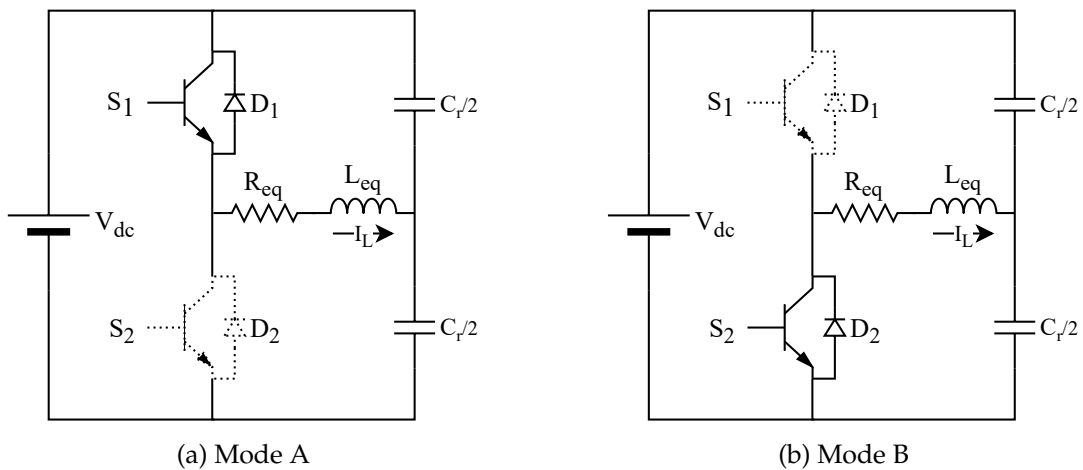
Figure 2.12: Operation modes of the resonant full-bridge inverter

In the full bridge analysis, the duty cycle and the switching frequency were found afterwards, the "control knobs" for the converter were the time instants t_1 and t_2. To give an alternative way of investigation, in this analysis the variables that influence the system will be the switching frequency f_s and the duty cycle D (i.e. the on-time of S_1 divided by the switching period).

Table 2.4: Operations mode summary of the half-bridge inverter

MODE	I_L	S_1	S_2	D_1	D_2
A	< 0			x	
	> 0	x			
B	> 0				x
	< 0		x		

2.2.3.2   Mode A: D_1 and then S_1 On

Mode A starts when S_2 is switched off, and since the load current is negative, D_1 starts conducting. The boundary conditions for this phase are:

$$v_c(0) = -V_{c0} \tag{2.16a}$$

$$i_L(0) = -I_0 \tag{2.16b}$$

The rail voltage V_{dc} is applied to the load so the current is raising: before it becomes positive, the switch S_1 must be switched on (ZVS) to carry the positive current. The analytical expressions for capacitor voltage and inductor current during mode A are ($0 < t < t_1$):

$$v_c(t) = V_{dc} + e^{-\alpha t} [-(V_{c0} + V_{dc}) \cos(\omega_d t) - \frac{1}{\omega_d} (\frac{I_0}{C_r} + \alpha(V_{c0} + V_{dc})) \sin(\omega_d t)] \tag{2.17a}$$

$$i_L(t) = e^{-\alpha t} [-I_0 \cos(\omega_d t) + \frac{1}{\omega_d} (\alpha I_0 + \frac{V_{c0} + V_{dc}}{L_{eq}} \sin(\omega_d t))] \tag{2.17b}$$

t_1 is the time instant when mode A ends, i.e. S_1 is opened, its value depends on the duty cycle D. With the introduction of the lossless snubber the losses associated to this switching are reduced, as already explained above. V_{c1} and I_1 are the capacitor voltage and inductor current at the time t_1.

2.2.3.3   Mode B: D_2 and then S_2 On

This mode is quite "specular" to mode A: the load is short circuited since D_2 conduct first and then, as soon as the current becomes negative, it flows through S_2 that has been switched on during the conduction time of D_2 (ZVS). The analytical expressions for voltage and current are found by using the boundary conditions at time t_1 ($t_1 < t < t_2$):

$$v_c(t) = e^{-\alpha(t-t_1)} [V_{c1} \cos(\omega_d(t-t_1)) + \frac{1}{\omega_d} (\frac{I_1}{C_r} + \alpha(V_{c1}) \sin(\omega_d(t-t_1))] \tag{2.18a}$$

$$i_L(t) = e^{-\alpha(t-t_1)} [I_1 \cos(\omega_d(t-t_1)) - \frac{1}{\omega_d} (\alpha I_1 + \frac{V_{c1}}{L_{eq}}) \sin(\omega_d(t-t_1))] \tag{2.18b}$$

Mode B is ended at the time t_2 when S_2 is turned off.

2.2.3.4   Overall considerations

If the steady state regime is achieved, $v_c(t_2) = v_c(t_1) = V_{c0}$ and $i_L(t_2) = i_L(t_1) = I_0$. V_{c0} and I_0 can be iteratively found similarly to what shown in section 2.2.2.5 for the full bridge converter. A flow chart that describe this process (implemented in Matlab) is depicted in figure 2.13.
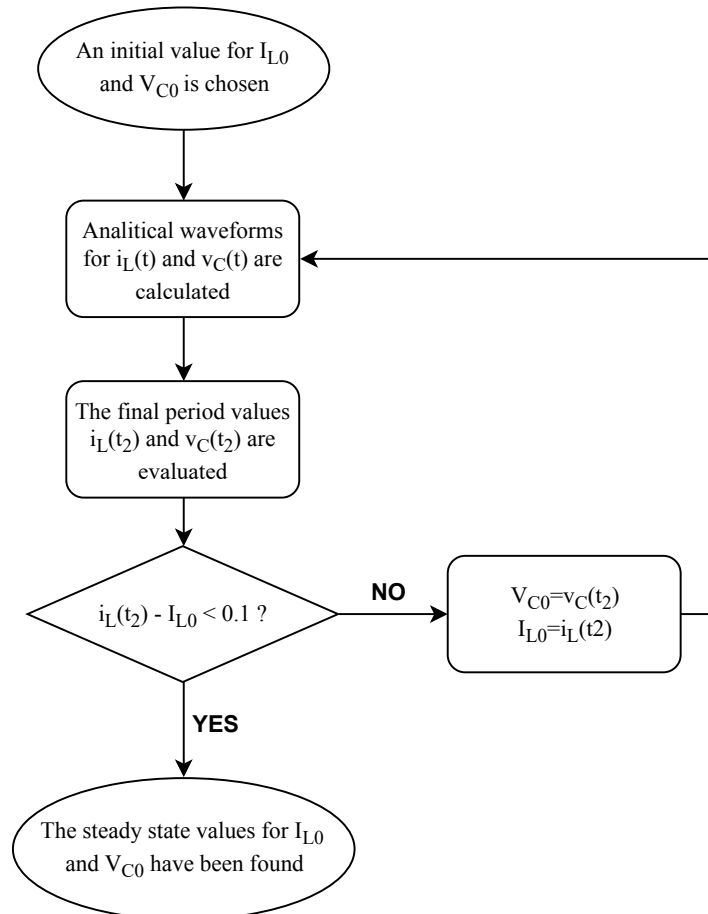

Figure 2.13: Description of the iterative process implemented to find the initial steady state value for capacitor voltage and inductor current.

An example of load waveforms can be found in figure 2.14. This time the "knobs" of the converter (the parameters that the user can set) are the switching frequency f_s and the duty cycle of S_1 (D). The duty cycle of the switch S_2 will be obviously $1 - D$. The time instants t_1 and t_2 are found by:

$$t_1 = \frac{D}{f_s} \tag{2.19a}$$

$$t_2 = \frac{1}{f_s} \tag{2.19b}$$

Also in the half bridge converter, lossless snubbers are used with exactly the same aim as described above in the case of a full bridge, with the same issues. In figure 2.15 the current and voltage across the switch S_1 when the deadtime and snubber capacitor size is properly set is showed.

(a) Load current
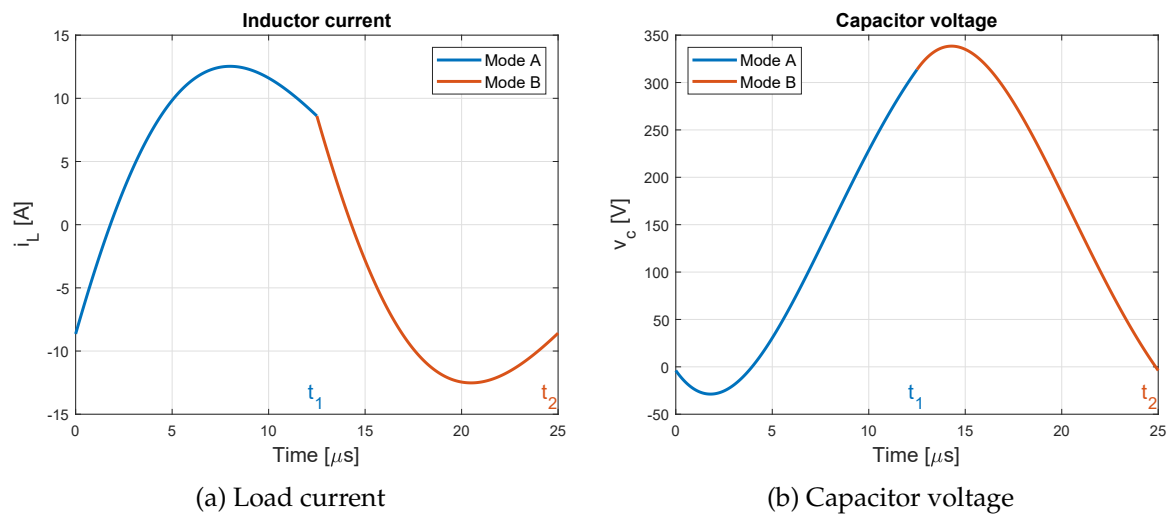
(b) Capacitor voltage

Figure 2.14: One period calculated half-bridge waveforms, with $D = 0.5$ and $f_s = 40\,kHz$, $v_c(0) = -V_{c0} = -3.87\,V$, $i_L(0) = -I_0 = -8.58\,A$.
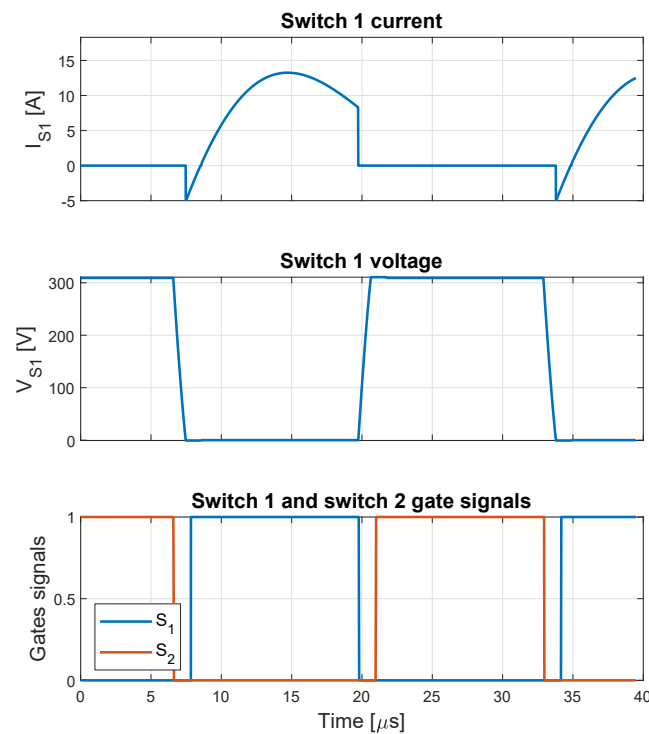

Figure 2.15: Examples of commutation with snubber capacitors $f_s = 38kHz, 1, D = 0.5, t_{dt} = 1.2\,\mu s, C_s = 10\,nF$

Some literature about the half bridge operation and modelling can be found in [10–12].

2.2.4   Quasi-resonant topologies

This topology uses only one switch to produce an high frequency waveform that is needed to "feed" the load. Multiple configurations for the inverter circuit have been found in the literature, and the three showed in [13] will be analysed and simulated in this section. Each topology have been studied analytically, and then the results have been validated with a simulink model.

2.2.4.1   First topology

In figure 2.16 the circuit diagram of the first topology of quasi resonant inverter analysed is showed. As can be seen, there isn't an antiparallel diode but it is connected in series with the switch. Also an external input inductor L_i is needed in this circuit. The analysis of this topolgy will be done with this circuital parameters: $R_{eq} = 8\,\Omega$, $L_{eq} = 40\,\mu H$, $L_i = 250\,\mu H$, $C_r = 110nF$ (taken from [13]).
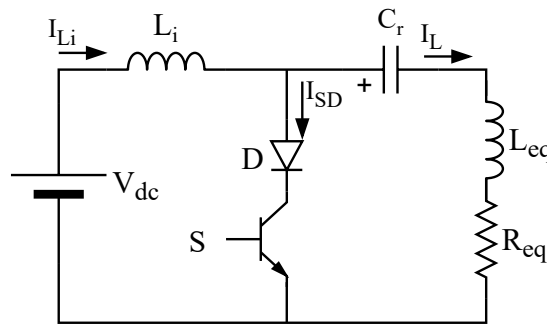
Figure 2.16: Circuit diagram for the first topology of quasi resonant inverter

The working operation of this circuit can be splitted into two modes, taking into account only the switch state. The switch and diode current is related to the current of both inductors through the relation $I_{SD} = I_{Li} - I_L$.

Mode A: switch On   When the switch is open, $I_{Li} = I_L$ so when the switch is closed $I_{SD}(0) = 0$ and a short circuit separate the circuit: L_i and the series L_{eq}, R_{eq}, C_R follow two independent behaviours. The capacitor is charged at V_{c0} at the begginning of the period. The voltage across L_i is costant so the current increase linearly while the RLC load starts oscillating itself as explained in section 2.2.1. The oscillation frequency for $(0 < t < t_1)$ is $f_{d1} = 74.2\,kHz$. Boundary conditions at the beginning of a steady state periods are:

$$v_c(0) = V_{c0} \tag{2.20a}$$
$$i_L(0) = I_0 \tag{2.20b}$$

The analytical expressions for the voltages and the currents in the circuit are $(0 < t < t_1)$:

$$i_{Li}(t) = I_0 + \frac{V_{dc}}{L_i} t \tag{2.21a}$$

$$v_c(t) = e^{-\alpha t}[V_{c0} \cos(\omega_{d1} t) + \frac{1}{\omega_{d1}}(\frac{I_0}{C_r} + \alpha V_{c0}) \sin(\omega_{d1} t)] \tag{2.21b}$$

$$i_L(t) = e^{-\alpha t}[I_0 \cos(\omega_{d1} t) - \frac{1}{\omega_{d1}}(\alpha I_0 + \frac{V_{c0}}{L_{eq}}) \sin(\omega_{d1} t)] \tag{2.21c}$$

Mode A ends at time t_1 when $i_L(t_1) = i_{Li}(t_1) = I_1$, so $I_{SD}(t_1) = 0$: the voltage across the diode ($V_{Cr} + V_{Leq} + V_{Req}$) becomes negative so D is blocking and the switch can be turned off achieving a *zero-current switching* (ZCS). It is important to say that the switch must be turned off before the voltage across the diode becomes positive again. In figure 2.17 the inductors current and the voltage across the diode are showed: it can be see that for this case after t_1 there are more or less $2\,\mu s$ (from t_1 to $10\,\mu s$) to switch off the transistor (the diode is inversely polarized). $-V_{c1}$ and I_1 are the capacitor voltage and inductors current at the time t_2.
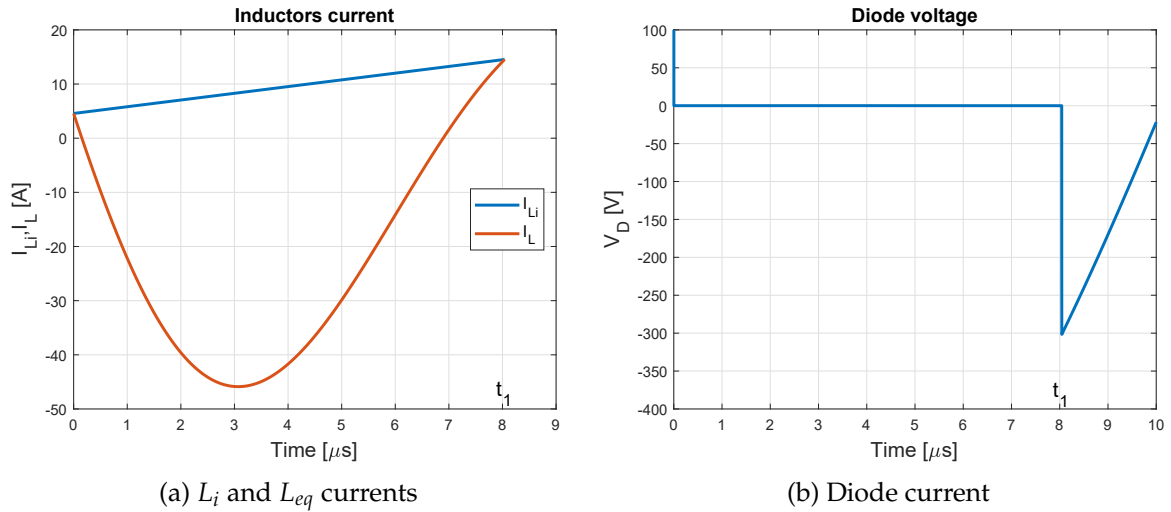
Figure 2.17: Some waveforms during mode A.

Mode B: switch Off   The switch is now open so the generator V_{dc} is now directly connected to all the R_{eq}, L_{tot}, C_r load, where $L_{tot} = L_i + L_{eq}$: the oscillation frequency is not f_{d1} anymore but it's lower due to the increase of the inductance. In this case is $f_{d2} = 28\,kHz$. During this phase, the current is positive so the capacitor voltage is increasing. Mode B ends at the time $t_2 = \frac{1}{f_s}$. The analytical expressions for the voltages and the currents in the circuit are $(t_1 < t < t_2)$:

$$i_{Li}(t) = i_L(t) \tag{2.22a}$$

$$v_c(t) = V_{dc} + e^{-\alpha\,(t-t_1)}[-(V_{dc} + V_{c1})\,cos(\omega_{d2}\,(t-t_1))+$$

$$\frac{1}{\omega_{d2}}(\frac{I_1}{C_r} - \alpha(V_{dc} + V_{c1}))sin(\omega_{d2}\,(t-t_1))] \tag{2.22b}$$

$$i_L(t) = e^{-\alpha\,(t-t_1)}[I_1\,cos(\omega_{d2}\,(t-t_1)) + \frac{1}{\omega_{d2}}(-\alpha\,I_1 + \frac{1}{L_{tot}}(V_{dc} + V_{c1}))\,sin(\omega_{d2}\,(t-t_1))] \tag{2.22c}$$

The steady state initial capacitor voltage and inductor current are found similarly to what already showed in figure 2.13, in such a way that $i_L(t_2) = i_{Li}(t_2) = I_0$ and $v_c(t_2) = V_{c0}$. At the time t_2 the switch is closed. This is also a ZCS because the current in the inductor must be continuous and since $i_{Li}(t_2) = i_L(t_2)$, $i_{SD}(t_2) = 0$. This is valid also at the time t_2^+ (just after t_2) because currents in inductors cannot make a step, so $i_{SD}(t_2^+) = 0$.

Overall considerations   Once the switching frequency is chosen, the operation of the converter is completely defined, since the duty cycle depends on the circuit parameters. A full period of load inductor and capacitor voltage is showed in picture 2.18 considering the load parameters already mentioned.

(a) Load current   (b) Capacitor voltage
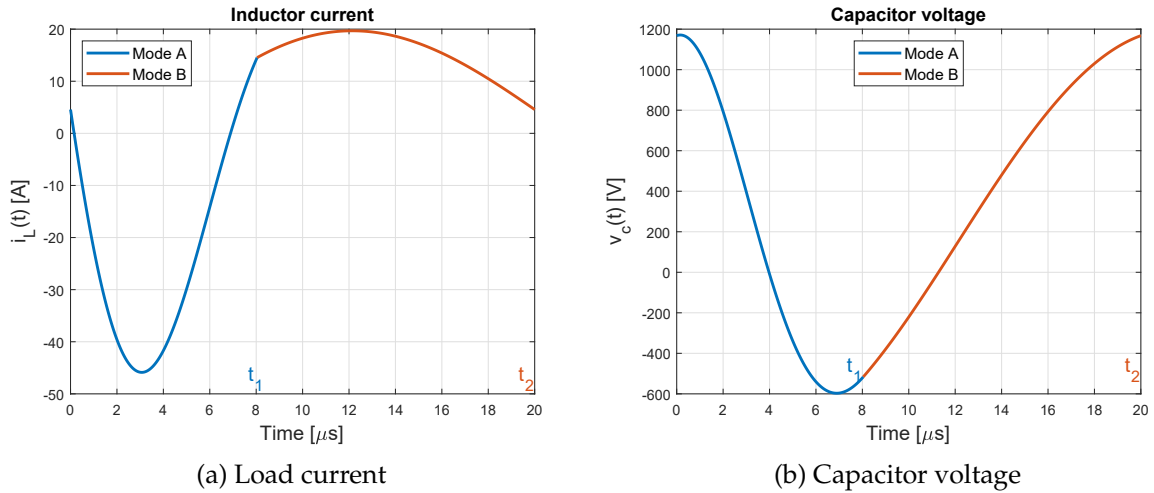
Figure 2.18: One period, calculated waveforms, for the first topology of quasi resonant inverter, with $f_s = 50\,kHz$

One more aspect to consider is the relationship between the duty cycle with the switching frequency as can be seen in figure 2.19a. The more the frequency increases, the more the duty cycle is high. This happens because $f_{d2} < f_s < f_{d1}$: the more f_s increase, the more the operation at $f_d 1$ (Mode A) must be enhanced. In addition, in figure 2.19b the current shape at different frequencies is showed. With the load values used in these examples, the frequency boundaries are around 30 and 50 kHz, the circuit cannot be operated outside of those limits. If they are not respected, ZCS will be lost.

If the switching frequency is outside of the boundaries, during Mode A the load current cannot reach the input inductor current so there won't be any t_1 time where $i_L(t) = i_{Li}(t)$. Consequently, when the switch turns off, $i_{SD}(t_1) = I_{Li}(t_1) - I_L(t_1) \neq 0 \rightarrow$ ZVS not possible.

(a) Duty cycle variations

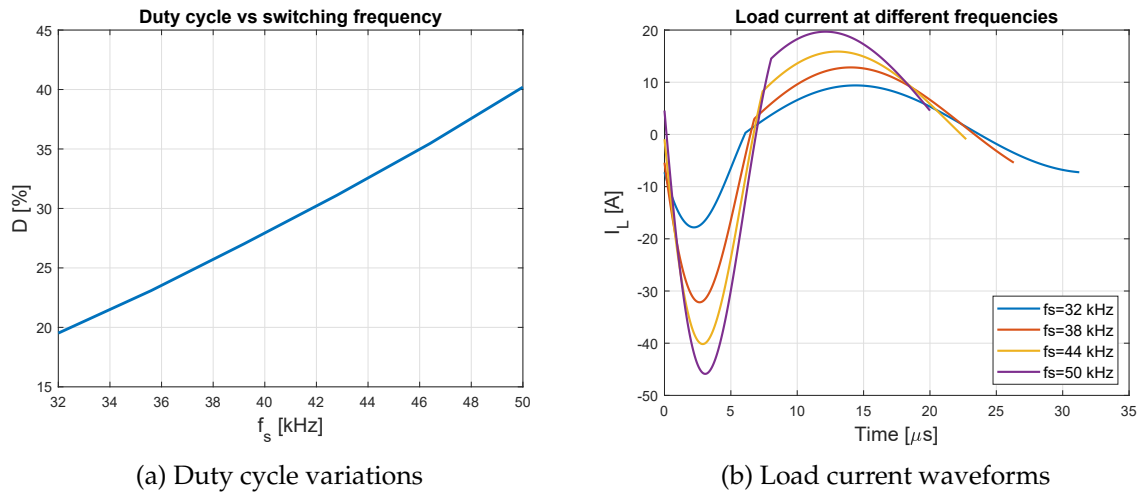(b) Load current waveforms

Figure 2.19: Waweforms and circuit parameter variations with different switching frequencies

2.2.4.2 Second topology

The second topology is very similar to the first one, the circuit diagram is showed in figure 2.20. The main difference is that the diode is now antiparallel to the switch. The circuital parameters will be kept the same as those used for the first topology ($R_{eq} = 8\,\Omega$, $L_{eq} = 40\,\mu H$, $L_i = 250\,\mu H$, $C_r = 110nF$)
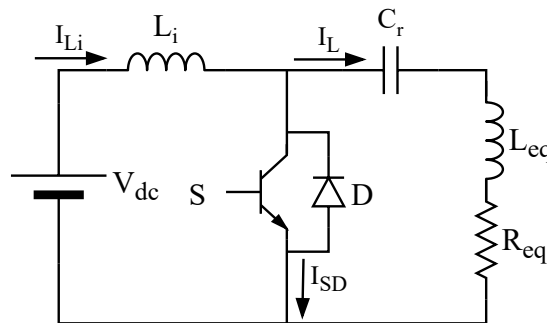
Figure 2.20: Circuit diagram for the second topology of quasi resonant inverter

Also the working operation is very similar, which can be splitted in two separated modes.

Mode A: switch/diode On   Mode A starts as already described for the first topology. At the beginning $I_{SD} = I_{Li} - I_L > 0$ so the switch conduct. The main difference is that once $I_{Li} = I_L$ (time instant t_1), the diodes D takes the conduction while $I_{SD} = I_{Li} - I_L > 0$ so during this phase the transistor can be turned off achieving a ZVS turn off. Once $I_{SD} = 0$ again the diode conduction stops and Mode B starts.

Boundary conditions at the beginning of a steady state period are:

$$v_c(0) = V_{c0} \tag{2.23a}$$
$$i_L(0) = I_0 \tag{2.23b}$$

The analytical expressions for the voltages and the currents in the circuit are $(0 < t < t_{11})$ (the same for mode A in the first topology):

$$i_{Li}(t) = I_0 + \frac{V_{dc}}{L_i} t \tag{2.24a}$$

$$v_c(t) = e^{-\alpha t} [V_{c0} \cos(\omega_{d1} t) + \frac{1}{\omega_{d1}} (\frac{I_0}{C_r} + \alpha V_{c0}) \sin(\omega_{d1} t)] \tag{2.24b}$$

$$i_L(t) = e^{-\alpha t} [I_0 \cos(\omega_{d1} t) - \frac{1}{\omega_{d1}} (\alpha I_0 + \frac{V_{c0}}{L_{eq}}) \sin(\omega_{d1} t)] \tag{2.24c}$$

To understand how the current conduction during mode A is carried firstly in the switch and secondly in the diode the figure 2.21 can be useful.
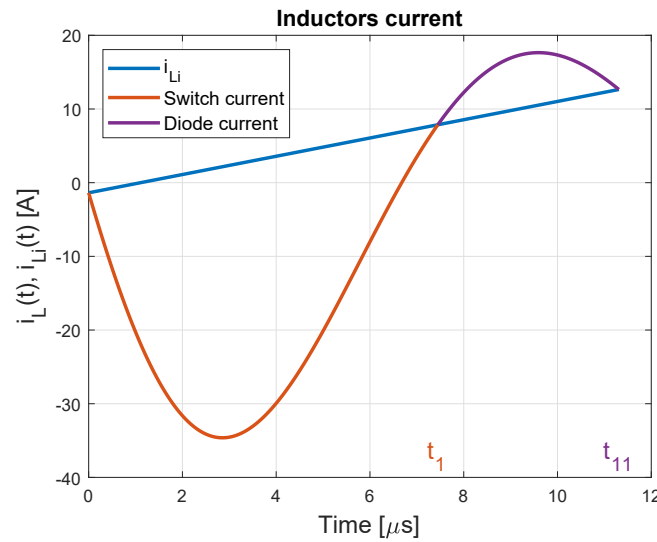
Figure 2.21: inductors current during mode A.

Mode B: switch/diode Off   Both the switch and the diode are opened. This phase is very similar to mode B of the previous topology. The oscillation frequency of the RLC load is now $f_{d2} > f_{d1}$. The analytical expressions and other considerations for the voltages and the currents in the circuit for $t_{11} < t < t_2$ are exactly the same as what already explained for mode B of the first quasi resonant topology (equations 2.22).

Overall considerations   A full period of load inductor and capacitor voltage is showed in figure 2.22. The relationship between the duty cycle and the switching frequency is very similar to the one already showed in figure 2.19a: D increase with f_s. The behaviour of the waveforms with different switching frequency is also very similar to what showed in figure 2.19b.

Depending on the circuit parameters, there are also values on the boundaries for the switching frequency. Soft switching is not achieved if f_s is too high or too low: the switch current oscillations during mode A are not enough high to overcome the input inductor current, so the diode won't turn on. One example of this situation is showed in figure 2.23

(a) Load current

(b) Capacitor voltage
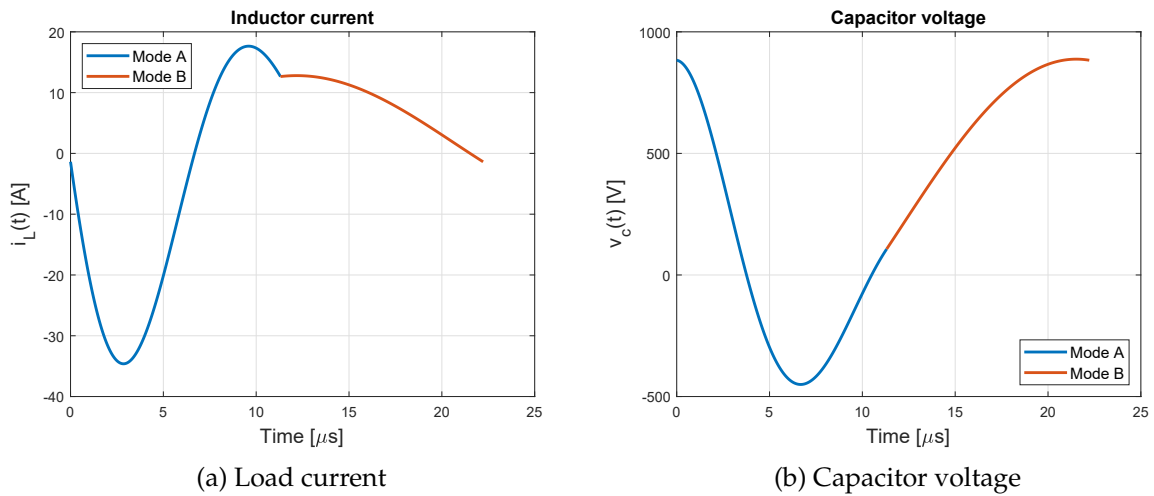
Figure 2.22: One period, calculated waveforms, for the first topology of quasi resonant inverter, with $f_s = 45\,kHz$
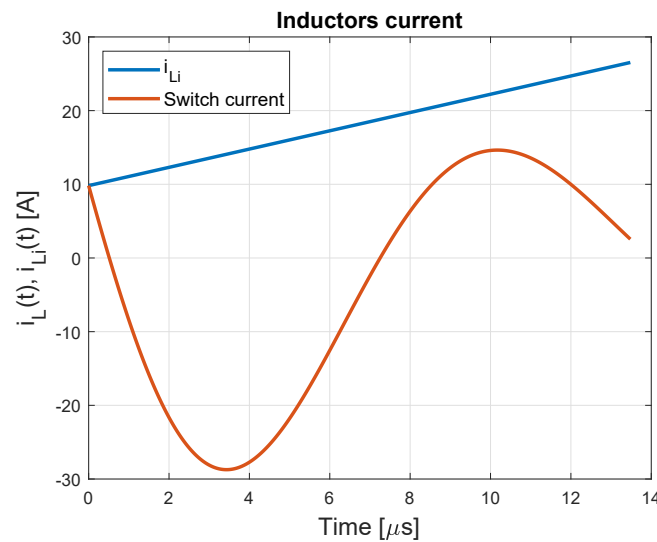
Figure 2.23: Inductors current during mode A with $f_s = 60kHz$ (too high).

2.2.4.3 Third topology

The circuit of the third topology is showed in figure 2.24. As can be seen, the input inductor is not needed. The analysis of this topolgy will be done with this circuital parameters: $R_{eq} = 8\,\Omega$, $L_{eq} = 60\,\mu H$, $C_r = 73nF$ (taken from [13]).

As usual, the operation of this converter can be splitted in two modes, depending on the switch state.

Mode A: switch/diode On The period starts when the diode is conducting: the capacitor voltage is $-V_{dc}$ and $i_L = i_{SD} < 0$. Since the capacitor voltage is constant, no current flows into it, while the current in the inductor increase exponentially (first order circuit with a time constant $\tau = \frac{L_{eq}}{R_{eq}}$). When the current becomes positive, the conduction switch from the diode to the transistor (ZVS) that have been turned on during the conduction of the diode. Mode A ends at

Figure 2.24: Circuit diagram for the third topology of quasi resonant inverter

the instant $t_1 = D' t_2$ where D' is the fraction of the total period in which the diode or the switch is conducting (the duty cycle of the switch D is lower).

Boundary conditions at the beginning of a steady state period are:

$$v_c(0) = -V_{dc} \tag{2.25a}$$

$$i_L(0) = I_0 \tag{2.25b}$$

The analytical expressions for the voltages and the currents in the circuit are $(0 < t < t_1)$:

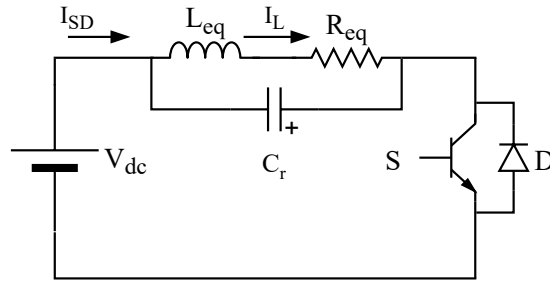$$v_c(t) = -V_{dc} \tag{2.26a}$$

$$i_L(t) = (I_0 - \frac{V_{dc}}{R_{eq}})e^{-\frac{t}{\tau}} + \frac{V_{dc}}{R_{eq}} \tag{2.26b}$$

t_0 is the time instant at which the conduction moves from the diode to the switch, and it can be analytically found by solving $i_L(t_0) = 0$ which gives

$$t_0 = -\tau \, ln(\frac{V_{dc}}{V_{dc} - I_0 R_{eq}}) \tag{2.27}$$

Mode B: switch Off   When the switch is turned off at time t_1, an indipendent RLC network must be studied, exactly what showed in figure 2.3. The analytical expressions for the waveforms during mode B $(t_1 < t < t_2)$ are

$$v_c(t) = e^{-\alpha(t-t_1)} \left[V_{c1} \, cos(\omega_d(t-t_1)) + \frac{1}{\omega_d}(\alpha V_{c1} + \frac{I_1}{C_r}) \, sin(\omega_d(t-t_1))\right] \tag{2.28a}$$

$$i_L(t) = e^{-\alpha(t-t_1)} \left[I_1 \, cos(\omega_d(t-t_1)) - \frac{1}{\omega_d}(\alpha I_1 + \frac{V_{c1}}{L_{eq}}) \, sin(\omega_d(t-t_1))\right] \tag{2.28b}$$

Mode B ends at time t_2 when

$$v_c(t_2) = I_0 \tag{2.29a}$$

$$i_L(t_2) = -V_{dc} \tag{2.29b}$$

Time istant t_2 is found with the same iterative method shown for the half and full bridge.

Overall considerations A full period of load inductor and capacitor voltage is showed in figure 2.25. Contrary to first and second topology showed above, the relationship between duty cycle and switching frequency is different. Since the duration of mode B is almost fixed (it depends on the inductor/load parameter), when f_s increase the duty cycle must be decreased in order to reduce the duration of Mode A, see figure 2.27. In figure 2.26 the duty cycle showed is calculated considering that the duty cycle is switched on at half conduction period of the diode (instant $\frac{t_0}{2}$):

$$D = \frac{t_1 - \frac{t_0}{2}}{t_2} \tag{2.30}$$

(a) Load current

(b) Capacitor voltage

Figure 2.25: One period, calculated waveforms, for the third topology of quasi resonant inverter, with $f_s = 40\,kHz$
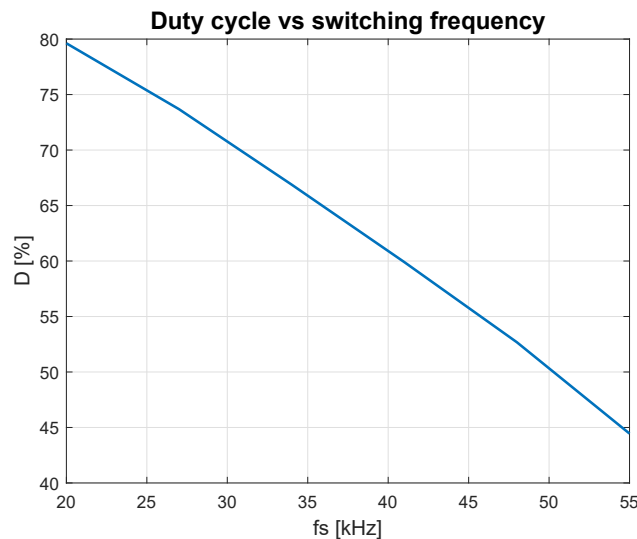
Figure 2.26: Relationship between duty cycle and switching frequency

If f_s is too high, the duty cycle will decrease is such a way that at a certain point the energy stored during Mode A won't be enough to cause the oscillation of $v_c(t)$ during mode B to reach $-v_{dc}$ again. To show this, figure 2.28 is useful.

(a) Capacitor voltage waveforms

(b) Load current waveforms

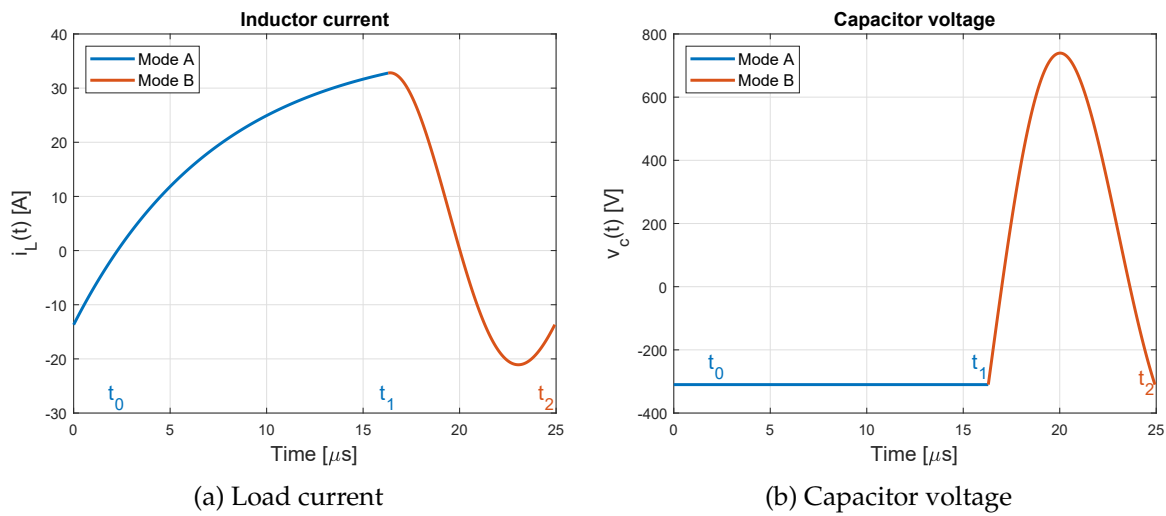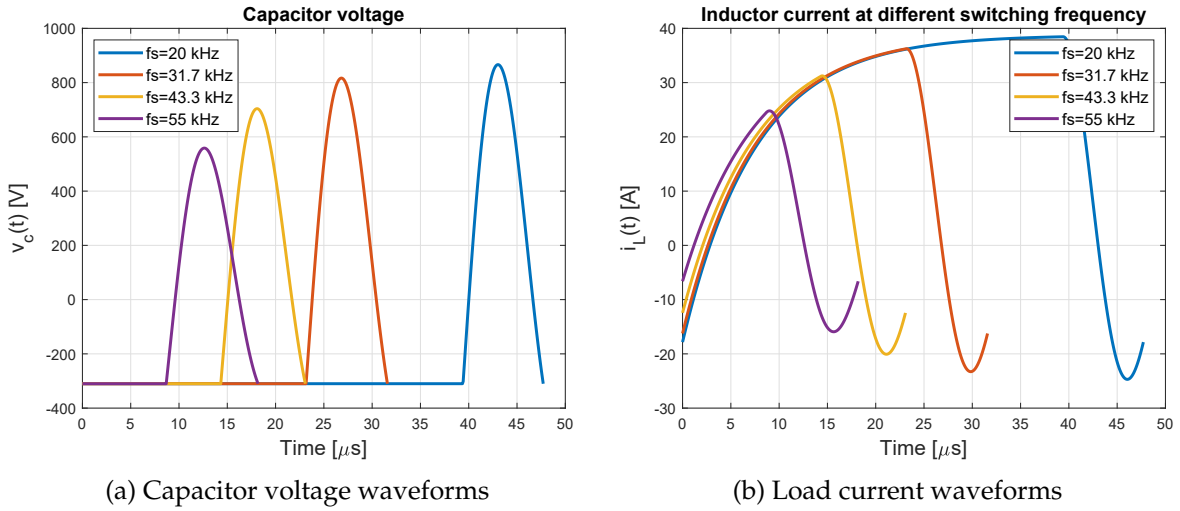Figure 2.27: Waweforms and variations with different switching frequencies

(a) Load current

(b) Capacitor voltage
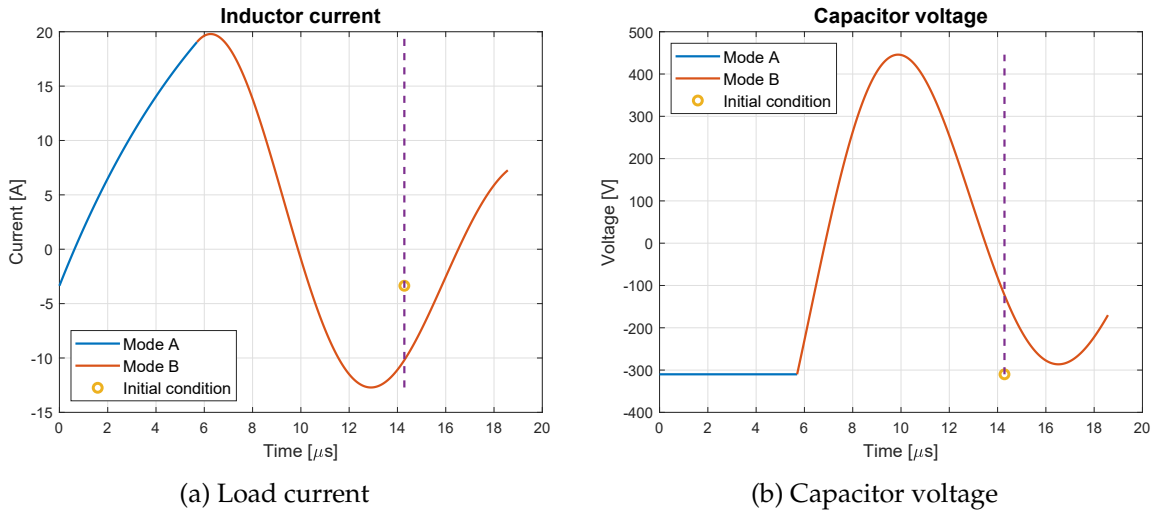
Figure 2.28: One period, calculated waveforms, for the third topology of quasi resonant inverter, with $f_s = 70\,kHz$

The steady state condition is marked with a yellow circle, which is at time $1/f_s$. The operation at $f_s = 70\,kHz$ is not feasible because it can be seen from figure 2.28b that even if the duty cycle should be lower, the capacitor voltage doesn't reach the steady state value $v_c(t_2) = -V_{dc}$ anymore. This is because the inductor energy stored during phase A is not enough to cause a suitable high oscillation amplitude of the capacitor voltage.

There isn't any minimum switching boundary that cause ZVS to be lost, but usually such a lower boundary is put at $20\,kHz$ that is the upper limit of the audible audio range.

2.2.4.4   Conclusions

Among the three topologies described, the third one is, by far, the most used. The first advantage is that the input inductor is not required. This is quite important since this kind of topology is used to produce cheap hobs. A comparison analysis have been made in [13]: the power output

range is higher in the first two topologies compared to the third one, but it turns out that on average the third topology has better overall performances, expecially in terms of component utilization factor.

On the other hand, one aspect that must be underlined is that the voltage stress of the switches is much higher in quasi resonant topologies compared to half/full bridge topologies: voltage across transistor can overcome 1000 V, while in bridge topologies it is clamped to a max value of V_{dc} by snubber capacitances.

2.3   EMI filters

Power electronics is increasingly being present in lots of device/appliances which are, in turns, widely present in everyday circumstances. This cause diverse circuits to operate in close proximity to each other: very often one device affect another one. In addition, electronics boards are becoming smaller and smaller, with consequent increase of interference between them. Not only have the systems to operate under ideal conditions in the laboratory, but also products must be designed to work in the "real world" with other equipment nearby, and to comply with electromagnetic compatibility (EMC) regulations. This means that the equipment should not be affected by external electromagnetic sources and should not itself be a source of electromagnetic noise that can pollute the environment and the grid[2].

2.3.1   Common mode and differential mode currents

Electromagnetic emissions are commonly related to common mode and/or differential mode currents. Consider the situation showed in figure 2.29, where a generator is supplying a load through a transmission line that is carrying the current I_1 in the top conductor and the current I_2 in the bottom conductor. Those two currents can be decomposed in two auxiliary terms named
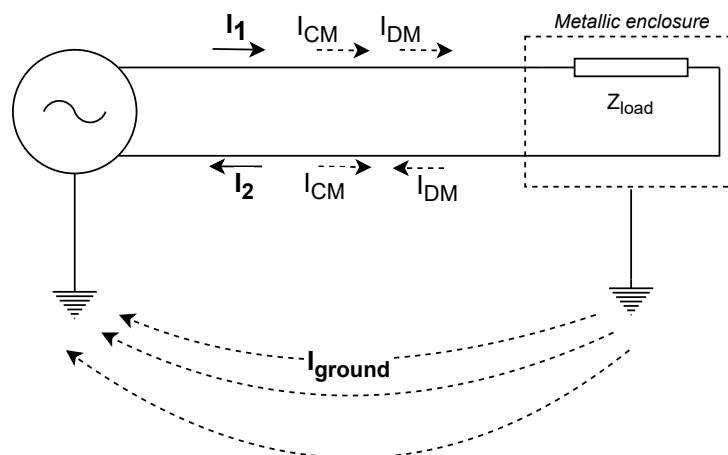

Figure 2.29: Decomposition of the currents on a two wire transmission line into common mode I_{CM} and differential mode I_{DM} components.

"common mode" $\bar{I}_{DM}$ and "differential mode" $\bar{I}_{DM}$ in such a way that the differential mode current are equal in magnitude and direction in each wire, while the differential one is equal in

magnitude but with opposite sign. So it is possible to state that:

$$\overline{I}_1 = \overline{I}_{DM} + \overline{I}_{CM} \tag{2.31a}$$

$$\overline{I}_2 = \overline{I}_{DM} - \overline{I}_{CM} \tag{2.31b}$$

Solving these two equations gives the value for the common mode and differential mode currents:

$$\overline{I}_{DM} = \frac{\overline{I}_1 + \overline{I}_2}{2} \tag{2.32a}$$

$$\overline{I}_{CM} = \frac{\overline{I}_1 - \overline{I}_2}{2} \tag{2.32b}$$

The common mode current returns to the supply via the ground conductor: $\overline{I}_{ground} = 2\,\overline{I}_{CM}$. During the normal operation of the circuit, only differential mode current flows and I_{CM} is zero. Common mode currents are usually the result of an external magnetic interference that is coupling with the ground loop created by the active conductors and the ground itself (common mode loop). The top/bottom conductors can create a loop with the ground even considering parasitic capacitances that are inherently present in the circuit. When a time-varying magnetic field flows inside a closed loop an electromotive force (emf) is induced, with the consequent flow of a current. Also a differential mode loop is present (between the two active conductors of the transmission line) but its area is often negligible, especially compared with common-mode loop one. As it might be understood, common mode current is unwanted. A first argument can be given thinking about radiated electric fields due to I_{CM} and I_{DM}. Each one can be superimposed to give the total radiated electric field. Since $\overline{E} = \rho\,\overline{J}$, it has the same direction as the current from which is generated. Since the differential mode currents are oppositely directed, the resulting electric field will also be oppositely directed: they will subtract to give a small net radiated electric field. On the other hand, since the common mode currents are directed in the same direction, their radiated field will add, giving a much larger contribution to the total radiated field: it can be stated that common-mode currents have a much higher potential for producing radiated emissions compared to differential mode currents.

2.3.2   Common mode currents rejection

There are several ways to reduce the common mode currents flow in a circuit: one of the most effective solution is to use a *common mode choke*. Two wires carrying currents $\overline{I}_1$ and $\overline{I}_2$ are wound around a ferromagnetic core as shown in figure 2.30. Note the points in the circuital symbol, which show the winding direction of the two coils: this means that the mutual inductance between the windings is positive.

If R_1 and R_2 are the resistances of each coil, L_1 and L_2 the self-inductances, M the mutual inductance beween the coils, the voltage across each winding is generally:

$$\overline{U}_1 = R_1\,\overline{I}_1 + j\,\omega L_1\,\overline{I}_1 - j\,\omega M\,\overline{I}_2 \tag{2.33a}$$

$$\overline{U}_2 = R_2\,\overline{I}_2 + j\,\omega L_2\,\overline{I}_2 - j\,\omega M\,\overline{I}_1 \tag{2.33b}$$
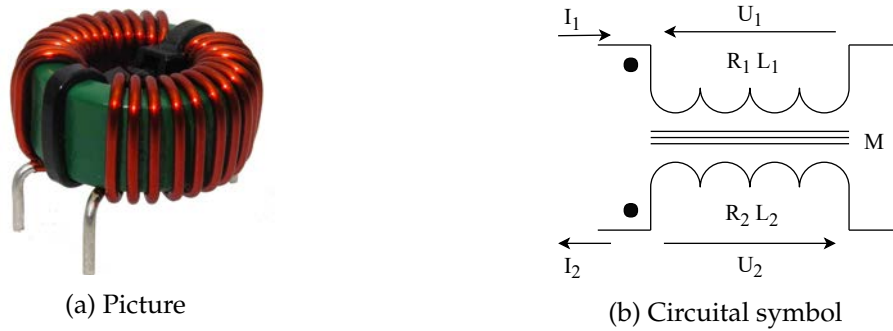
(a) Picture

(b) Circuital symbol

Figure 2.30: Appearance and symbol of a common mode choke

So the impedance of each coil, seen by each branch current is

$$\dot{Z}_1 = \frac{\overline{U}_1}{\overline{I}_1} = R_1 + j\,\omega L_1 - j\,\omega M \frac{\overline{I}_2}{\overline{I}_1} \tag{2.34a}$$

$$\dot{Z}_2 = \frac{\overline{U}_2}{\overline{I}_2} = R_2 + j\,\omega L_2 - j\,\omega M \frac{\overline{I}_1}{\overline{I}_2} \tag{2.34b}$$

If windings are identical and there isn't any flux leakage in the magnetic circuit (the flux of one winding completely links the other winding) $L_1 = L_2 = L = M$. If only differential mode currents is flowing in the circuit, $\overline{I}_2 = \overline{I}_1$ and equations 2.34 become:

$$\dot{Z}_1 = R_1 + j\,\omega(L_1 - M) = R_1 \tag{2.35a}$$
$$\dot{Z}_2 = R_2 + j\,\omega(L_2 - M) = R_2 \tag{2.35b}$$

On the other hand, if only common mode currents is flowing in the circuit, $\overline{I}_2 = -\overline{I}_1$ and equations 2.34 become:

$$\dot{Z}_1 = R_1 + j\,\omega(L_1 + M) = R_1 + j\,\omega\,2L \tag{2.36a}$$
$$\dot{Z}_2 = R_2 + j\,\omega(L_2 + M) = R_2 + j\,\omega\,2L \tag{2.36b}$$

As can be seen, a common mode choke has no effect on differential mode currents (R_1 and R_2 are almost negligible) but it places an inductance of value $2\,L$ in series with the two conductors to common mode currents. In order to provide this behaviour, it is very important to wound correctly the wires aroud the core in such a way that the fluxes due to the two common-mode currents add in the core whereas the fluxes due to the two differential-mode currents subtract. High common mode currents, howewer, can saturate the core leading to an important decrease of L which, in turns, can ruin the effect of the choke. Usually, howewer, common mode currents are together with differential mode currents that cancel out in the core ad do not saturate it. Typical value for L varies from $10\,mH$ to $50\,mH$ in high power converters.

In addition to common mode choke, common mode rejection is improved by connecting two capacitors (called *y capacitors*) from line to ground and from neutral to ground, as can be seen in figure 2.31. The task carried out by those capacitors is to shunt or bypass the high-frequency common mode noise to ground.
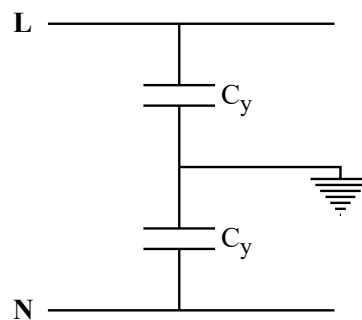
Figure 2.31: Example of Y cap connection in a circuit

2.3.3 Differential mode rejection

In parallel with common mode chokes, also *differential mode chokes* are used. The aim is to suppress harmonics and unwanted signals that add to the differential (desired) one. The easiest approach is to build a common mode choke but *reverse* one of the two windings, in such a way that no impedance is seen from common mode currents while a big one is seen from high frequency differential mode harmonics. The problem with this approach is that differential current will saturate the core during normal operation since the fluxes add each other. The solution is obtained building two inductors separately (figure 2.32a). The main task of this component is to provide an high impedance path to high frequencies voltage harmonics ($Z_L = j\omega L$), so less high frequency currents can flow (Ohm's law). The connection in the circuit (figure 2.32b) is similar to the common mode one. Typical values for the inductances used can vary from $500\,\mu H$ to $1\,mH$.

(a) Picture

(b) Circuital symbol
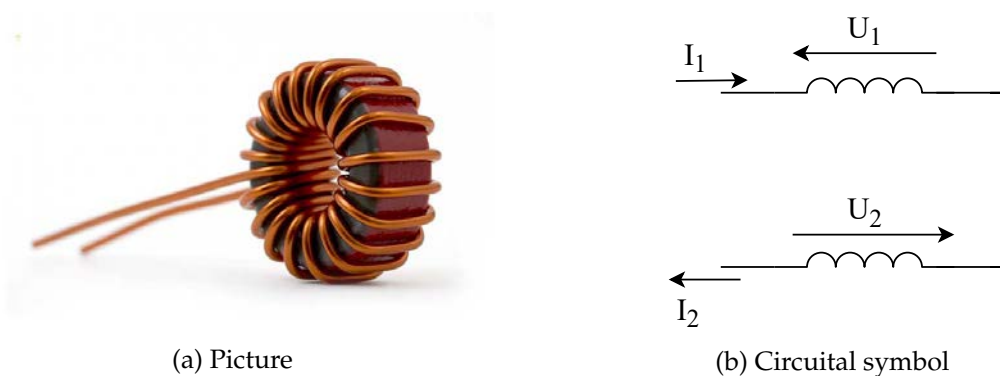
Figure 2.32: Appearance and symbol of a differential mode choke

Together with the inductors, capacitors placed between L and N conductors (so called *x-capacitors*) offer a low impedance path for high frequencies noise. More than one can be present in the input filter. Essentially, a low-pass filter is used to suppress high-frequency-differential mode noise, whatever is coming from the grid or is generated from the cooktop.

2.3.4 Overview of an EMI input filter

In the following figures, some EMI filter architectures are displayed. Note that possible configurations are possible and not always all the components analysed above are present together.

Integrated common mode and differential mode chokes have also been built [3], but the operation for common mode and differential mode rejection is as explained for the "separated" chokes.
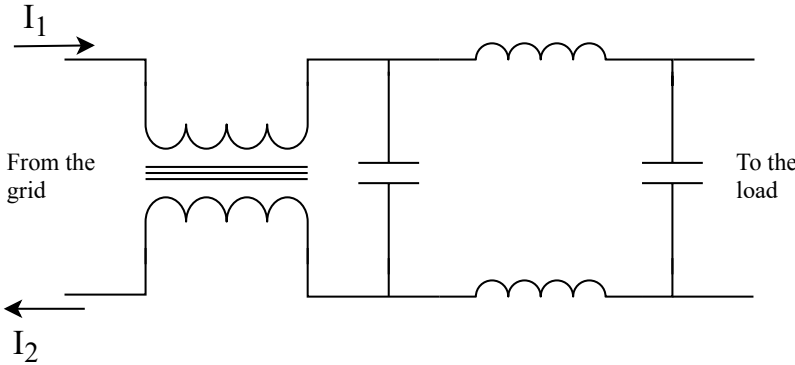
Figure 2.33: First example of EMI input filter

Figure 2.34: Second example of EMI input filter

Chapter 3

Inductor and load modelling

In this chapter, different techniques that are available to model the inductor together with the load will be investigated. As showed in the previous parts of this thesis, everything can be considered as a series resistance-inductor connection. It seems to be a very easy model but inside those simple elements, multiples phenomena are hidden and must be taken into account. After the explanation of some theoretical background where the equations describing field quantities i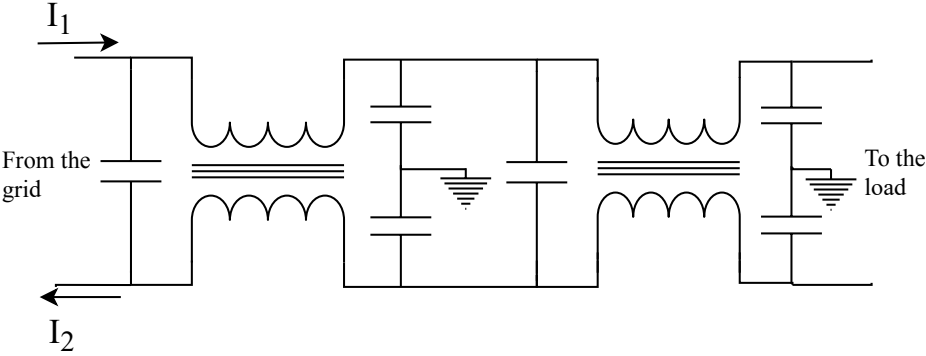nvolved in the system are showed, an analytic method will be presented and the results will be compared to a finite element analysis.Then, to take into account the saturation effects that can occur in the pot, an iterative method to find an equivalent relative permeability for the stainless steel will be presented and analysed. Finally, some conclusions will be drawn to understand which are the advantages and limitations of the analytical method compared to the FEM one.

3.1 Physical description for a planar circular coil between pot and ferrite

3.1.1 Differential equations

The inverter output is connected to a pancake inductor with a series connected resonant capacitor. The coil is, in turn, placed between a pot and a ferrite layer, which provides a low reluctance path to the magnetic field, so it acts as a flux concentrator but also as a shield for the power electronics that is in the bottom. A schematic of the geometry under study is showed in figure 3.1. Ferrite usually comes as several bars radially distributed around the centre of the coil, this because the material is difficult and expensive to cut into circular shapes. By the way, it will be considered as a disc, in order to maintain the axial symmetry of the problem. To further shield the electronics, a metallic conductive plate (usually aluminium) is placed under the ferrite layer. The pot is represented only as a metallic disc, in fact the bottom of the pot is usually made up of different layers (sandwich). The eddy currents flow only in the lower level, since it is built with magnetic stainless steel (AISI 409 or 430), the thickness is not more than 1-2 mm. Above that, an aluminium layer is placed in order to evenly spread the heat in the rest of the pan which is made of common, non-magnetic stainless steel. Taking into account the magnetic problem, only the lower layer is relevant because it is the only part where eddy currents flow: it act as a shield for the upper part of the pan which is relevant only for thermal purposes.

To study this problem, the best choice for the coordinate system is the cylindrical one.The pot will be considered with a constant permeability and the computation of the impedance
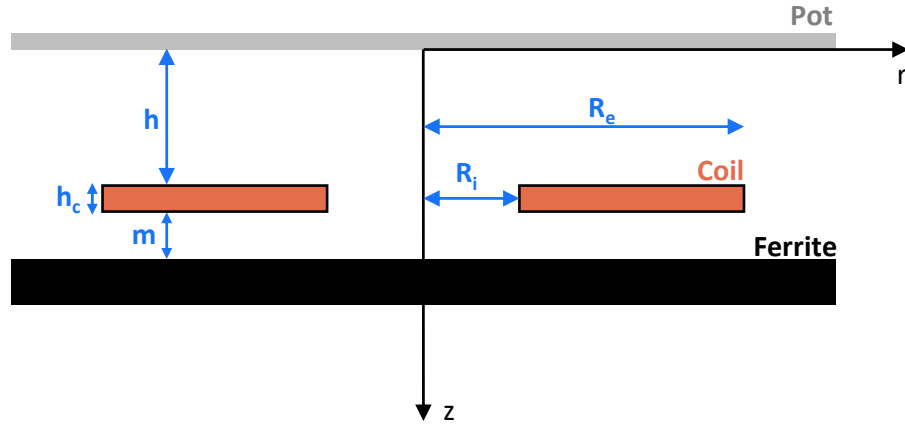
Figure 3.1: Configuration analysed for the computation of the impedance at the inductor extremities

is performed writing the equations using the magnetic potential vector **A** as main variable. In particular, due to the symmetry of the geometry, some considerations about the vector components can be made. Firstly, the magnetic flux density **B** has only radial and vertical component (it stays in the r-z plane):

$$\mathbf{B} = (B_r, B_\varphi, B_z) = (B_r, 0, B_z) \tag{3.1}$$

Since

$$\mathbf{B} = \nabla \times \mathbf{A} \tag{3.2}$$

it holds that A is perpendicular to B, so the vector potential has only azimuthal component:

$$\mathbf{A} = (A_r, A_\varphi, A_z) = (0, A_\varphi, 0) \tag{3.3}$$

In particular, $A_\varphi = A_\varphi(r,z)$: the azimuthal component cannot vary with φ. To find the general differential equation that describe the problem, the following Maxwell equation must be considered, with obvious meaning of the symbols:

$$\nabla \times \mathbf{H} = \mathbf{J} \tag{3.4}$$

Since $\mathbf{H} = \frac{\mathbf{B}}{\mu}$ and $\mathbf{J} = \sigma \, \mathbf{E}$, equation 3.4 becomes:

$$\nabla \times \frac{\mathbf{B}}{\mu} = \sigma \, \mathbf{E} \tag{3.5}$$

Now the magnetic permeability can be taken out of the curl symbol since it is a constant scalar, and considering also equation 3.2:

$$\frac{1}{\mu} \nabla \times (\nabla \times \mathbf{A}) = \sigma \, \mathbf{E} \tag{3.6}$$

Then the properties for the curl of a curl is applied:

$$\nabla(\nabla \cdot \mathbf{A}) - \nabla^2 \mathbf{A} = \mu \, \sigma \, \mathbf{E} \tag{3.7}$$

It is now convenient to take $\mathbf{A}$ in such a way that $\nabla \cdot \mathbf{A} = 0$ (Coulomb gauge). By the way, it must be taken into account that this assumption has not a physical meaning, such as $\nabla \cdot \mathbf{B} = 0$. The following Maxwell equation must be now taken into account:

$$
\begin{aligned}
\nabla \times \mathbf{E} &= -\frac{\partial \mathbf{B}}{\partial t} \\
&= -\frac{\partial^2}{\partial t \partial (\nabla \times \mathbf{A})} \\
&= -\nabla \times \frac{\partial \mathbf{A}}{\partial t}
\end{aligned}
\tag{3.8}
$$

Looking at the extremities of the equation it can be finally said that

$$
\mathbf{E} = -\frac{\partial \mathbf{A}}{\partial t}
\tag{3.9}
$$

Now, substituting the gauge relation, and putting equation 3.9 in 3.7, the Poisson's equation for this system is obtained:

$$
\begin{aligned}
\nabla^2 \mathbf{A} &= \mu\sigma \frac{\partial \mathbf{A}}{\partial t} \\
&= \mu\sigma j\omega \mathbf{A}
\end{aligned}
\tag{3.10}
$$

The Laplacian of $\mathbf{A} = (A_r, A_\varphi, A_z)$ in cylindrical coordinates is:

$$
\nabla^2 \mathbf{A} = \left(\nabla^2 A_r - \frac{A_r}{r^2} - \frac{2}{r^2}\frac{\partial A_\varphi}{\partial \varphi}, \nabla^2 A_\varphi - \frac{A_\varphi}{r^2} + \frac{2}{r^2}\frac{\partial A_r}{\partial r}, \nabla^2 A_z \right)
\tag{3.11}
$$

Since $A_r = A_z = 0$, as already mentioned in equation 3.3, and A_φ is constant along φ:

$$
\nabla^2 \mathbf{A} = \left(0, \nabla^2 A_\varphi - \frac{A_\varphi}{r^2}, 0 \right)
\tag{3.12}
$$

In turns, the laplacian of A_φ in cylindrical coordinates, taking into account also the simplifications due to the symmetry of the configuration, is:

$$
\begin{aligned}
\nabla^2 A_\varphi = \nabla \cdot (\nabla A_\varphi) &= \nabla \cdot \left(\frac{\partial A_\varphi}{\partial \varphi}, \frac{1}{r}\frac{\partial A_\varphi}{\partial \varphi}, \frac{\partial A_\varphi}{\partial z} \right) \\
&= \nabla \cdot \left(\frac{\partial A_\varphi}{\partial r}, 0, \frac{\partial A_\varphi}{\partial z} \right) \\
&= \frac{1}{r}\frac{\partial}{\partial r}\left(r\frac{\partial A_\varphi}{\partial r} \right) + 0 + \frac{\partial}{\partial z}\left(\frac{\partial A_\varphi}{\partial z} \right) \\
&= \frac{1}{r}\frac{\partial A_\varphi}{\partial r} + \frac{\partial^2 A_\varphi}{\partial r^2} + \frac{\partial^2 A_\varphi}{\partial z^2}
\end{aligned}
\tag{3.13}
$$

Equations 3.10 together with 3.12 and 3.13 becomes:

$$
\nabla^2 \mathbf{A} = \left(0, \frac{1}{r}\frac{\partial A_\varphi}{\partial r} + \frac{\partial^2 A_\varphi}{\partial r^2} + \frac{\partial^2 A_\varphi}{\partial z^2} - \frac{A_\varphi}{r^2}, 0 \right) = \mu\sigma j\omega \mathbf{A}
\tag{3.14}
$$

So, the final equation that holds for the magnetic vector potential is:

$$\frac{\partial^2 A_\varphi}{\partial r^2} + \frac{1}{r}\frac{\partial A_\varphi}{\partial r} - \frac{A_\varphi}{r^2} + \frac{\partial^2 A_\varphi}{\partial z^2} = j\omega\mu\sigma\, A_\varphi \tag{3.15}$$

In particular, taking into account that $\sigma = \frac{1}{\rho}$ is zero in the air, equation 3.15 can be further elaborate:

$$\frac{\partial^2 A_\varphi}{\partial r^2} + \frac{1}{r}\frac{\partial A_\varphi}{\partial r} - \frac{A_\varphi}{r^2} + \frac{\partial^2 A_\varphi}{\partial z^2} = \begin{cases} 0 & \text{in the air} \\ \frac{j\omega\mu\, A_\varphi}{\rho} & \text{in the metal} \end{cases} \tag{3.16}$$

The equation can be solved using the variable separation method. A possible solution of the differential equation is then:

$$A_\varphi(r,z) = R(r)Z(z) \tag{3.17}$$

Substituting the general solution in the Laplace equation:

$$Z\frac{d^2R}{dr^2} + Z\frac{1}{r}\frac{dR}{dr} - \frac{Z\,R}{r^2} + R\frac{d^2Z}{dz^2} = 0 \tag{3.18}$$

Dividing by Z:

$$\frac{d^2R}{dr^2} + \frac{1}{r}\frac{dR}{dr} - \frac{R}{r^2} + \frac{R}{Z}\frac{d^2Z}{dz^2} = 0 \tag{3.19}$$

Using k as the separation constant/variable and replacing it in equation 3.19:

$$k^2 = \frac{1}{Z}\frac{d^2Z}{dz^2} \tag{3.20a}$$

$$\frac{d^2R}{dr^2} + \frac{1}{r}\frac{dR}{dr} - \frac{R}{r^2} + Rk^2 = 0 \tag{3.20b}$$

Multiplying both sides by r^2 and rearranging the equation:

$$r^2\frac{d^2R}{dr^2} + r\frac{dR}{dr} - R + Rr^2k^2 = 0$$
$$r^2\frac{d^2R}{dr^2} + r\frac{dR}{dr} + R(k^2r^2 - 1) = 0 \tag{3.21}$$

Equation 3.21 is a Bessel equation and the solutions is

$$R(r) = c_1\,J_1(k\,r) + c_2\,Y_1(k\,r)\ c_1, c_2 \in \mathbb{R}$$
$$= f(k)\,J_1(k\,r) \tag{3.22}$$

where J_1 and Y_1 are Bessel functions respectively of first and second kind, first order. The solution of the equation 3.20b is [14]:

$$Z(z) = C'(k)e^{kz} + D'(k)e^{-kz} \tag{3.23}$$

So the final expression for the vector potential is [14]:

$$A_\varphi = R(r)Z(z)$$
$$= J_1(k\,r)[C(k)e^{kz} + D(k)e^{-kz}] \tag{3.24}$$

Where $C(k) = f(k)C'(k)$ and $D(k) = f(k)D'(k)$.

If the solution extends radially, so that there are no restrictions on the radial function $R(r)$, there are correspondingly no restrictions on k and the solution involves an integral over all k:

$$A_\varphi = \int_0^{+\infty} J_1(k\,r)[C(k)e^{kz} + D(k)e^{-kz}]\,\mathrm{d}k \tag{3.25}$$

From now on, the analytical solutions of the problem is showed in [14]. All the results for the vector potential in the different regions involved is evaluated. To find those relations, boundary conditions are exploited in order to derive the expressions for the coefficients $C(k)$ and $D(k)$.

3.1.2 Boundary conditions

Between two different materials, at the interface, it holds the continuity of the normal component of **B** and tangential component of **H**. The magnetic field components in cylindrical coordinates are (taking into account also the simplifications due to symmetry):

$$\begin{aligned} \mathbf{H} &= \frac{\mathbf{B}}{\mu} = \frac{1}{\mu}(\boldsymbol{\nabla} \times \mathbf{A}) \\ &= \frac{1}{\mu}\left(-\frac{\partial A_\varphi}{\partial z}, 0, \frac{1}{r}\frac{\partial(r\,A_\varphi)}{\partial r}\right) \end{aligned} \tag{3.26}$$

So the quantities of interest for the boundary conditions computation are

$$\begin{aligned} B_z &= \frac{1}{r}\frac{\partial(r\,A_\varphi)}{\partial r} \\ &= \frac{1}{r}\left(A_\varphi + r\frac{\partial A_\varphi}{\partial r}\right) \\ H_r &= -\frac{1}{\mu}\frac{\partial A_\varphi}{\partial z} \end{aligned} \tag{3.27}$$

Generally considering an interface between materials 1 and 2, the boundary condition for the tangential magnetic field is:

$$H_1 r = H_2 r \tag{3.28a}$$

$$\frac{1}{\mu_1}\frac{\partial A_{\varphi 1}}{\partial z} = \frac{1}{\mu_2}\frac{\partial A_{\varphi 2}}{\partial z} \tag{3.28b}$$

Since the boundary conditions must be satisfied over the entire material separation, fields on both sides of the interface must have the same functional dependence on the radius r [15]:

$$\frac{\partial A_{\varphi 1}}{\partial r} = \frac{\partial A_{\varphi 2}}{\partial r} \tag{3.29}$$

Taking into account equation 3.29, the boundary condition on normal magnetic field becomes (at the interface $r_1 = r_2$):

$$B_1 z = B_2 z \tag{3.30a}$$

$$\frac{1}{r_1}\left(A_{\varphi 1} + r\frac{\partial A_{\varphi 1}}{\partial r}\right) = \frac{1}{r_2}\left(A_{\varphi 2} + r\frac{\partial A_{\varphi 2}}{\partial r}\right) \tag{3.30b}$$

$$A_{\varphi 1} = A_{\varphi 2} \tag{3.30c}$$

So, equations 3.28b and 3.30c are the boundary conditions applied between the interfaces from one material to another (pot, air, inductor, ferrite).

3.1.3   Physical phenomena that affect the impedance values

As already mentioned, the system inductor+load, can be modelled as an equivalent resistor R_{eq} and inductor L_{eq} (figure 3.2), which are connected in series with a resonant capacitor C_r. Behind the lumped parameters value, several physical phenomena are hidden. In this section a brief explanation of their aspects will be given, in order to better understand the results that will be presented in the next sections. Further considerations about their behaviour with different supply quantities (current, frequencies) will be presented in chapter 4.

Figure 3.2: Lumped parameters model of the inductor and load system

3.1.3.1   Equivalent resistance

The equivalent resistance R_{eq} can be decomposed in two main terms:

$$R_{eq} = R_c + \Delta R \tag{3.31}$$

Where R_c is the resistance of the coil, and ΔR is the resistance change when the pan is put above the inductor. The current density **J** that is induced in the pot generates heat through Joule losses, according to equation 3.32:

$$P_{pot} = \int_{V_{pot}} \rho_{pot} \mathbf{J}^2 \, dV \tag{3.32}$$

Defined I the rms value of the current in the coil, ΔR is then defined as:

$$\Delta R = \frac{P_{pot}}{I^2} \tag{3.33}$$

Then, considering I constant, R is directly proportional to the power dissipated in the pot. The value of R is affected by several aspects. For example, the more is the pot close to the coil, the more ΔR will be high. But also, the number of turns, the geometry of the inductor and the radius of the pan can substantially affect the values of the resistance. Everything that can increase the

value of the eddy currents in the pan will contribute to the raising of the resistance: the more is the inductor big, the more R_{eq} is high. As can be easily understood, ΔR is always positive. Since the coil is made of Litz wire, it's resistance calculation is not straightforward and a method of computation will be presented in the section 3.2.2.

3.1.3.2 Equivalent inductance

Also the equivalent inductance is composed by two main terms:

$$L_{eq} = L_c + \Delta L \tag{3.34}$$

L_c is the self inductance of the coil and ΔL is the change of the inductance due to the presence of the pan above the cooktop, which depends mainly on two phenomena:

- magnetization effect: placing the pot above the inductor is like placing a ferromagnetic core in a transformer which increase the inductance by a factor of μ_{pot}.
- demagnetization effect: eddy currents in the pot are generated by means of the Faraday-Lenz law, which substantially states that the magnetic flux generated by them counteracts the flux variations produced by the inductor. The basic transformer theory can be applied to figure out that the demagnetization effect leads to a drop of the total inductance.

Generally, magnetization occur with high permeability-low conductive materials (ferrites, for example), while demagnetization happen when the material has high conductivity (copper and aluminium, for example). Concerning the induction cooking, the demagnetizing effect is the dominant one, and how it happens can be explained in two ways, depending on how the inductor is supplied:

- Voltage source with fixed rms value: as the basic transformer theory explains, once the load is connected to the secondary of the transformer, an increase of the current absorbed at the primary counteract the flux generated by the secondary circuit, while the flux remains constant:

$$L_{eq} = \frac{\Phi_0}{I_1} = \frac{\Phi_0}{|\overline{I_1'} + \overline{I_0}|} \tag{3.35}$$

- Current source with fixed rms value: the magnetic flux produced by the primary circuit is fixed, while the secondary one depends on the load. The total one, sum of the two, has a lower rms value due to the phase shift between the two magnetic fluxes, that is more than 90°:

$$L_{eq} = \frac{\Phi_{tot}}{I_1} = \frac{|\overline{\Phi_{coil}} + \overline{\Phi_{pot}}|}{I_1} \tag{3.36}$$

The huge amount of eddy currents cause also the decrease of the magnetic permeability of the pot due to saturation phenomena.

Due to the predominant demagnetization effect, therefore, $\Delta L < 0$, so $L_{eq} < L_c$. The more the eddy currents, the more the demagnetizing effect. As an exaple, one parameter that mostly affect the inductance drop is the frequency of the supply current. The more it is, the high is the magnetic flux variation with consequent increase of eddy currents.

3.2 Analytical modeling

3.2.1 Code description

The complete solving of equation 3.16 using the boundary conditions described in the previous section, have been done by professor Lupi and his research group at the university of Padua, and the work results are displayed in [16]. They have then been implemented with a Matlab script that calculates the impedance seen at the inductor extremities and the current density distribution in the pan. Howewer, some assumptions have been made in the procedure for the calculations:

- The thickness of the coil h_c is negligible
- The relative magnetic permeability of the pot μ_{pot} is constant: the saturation effect is not taken into account
- The relative magnetic permeability of the ferrite layer is infinite: no magnetic field can go through it
- The pot and ferrite radial dimensions are considered to be infinite

Some improvements have been made during the work for this thesis. First of all, to take the thickness of the coil into account, the Matlab script have been modified, changing the value of the parameters h and m, incorporating the hc value:

- $h_{new} = h + \frac{h_c}{2}$
- $m_{new} = m + \frac{h_c}{2}$

So, while the user will always consider the parameters h and m as showed in figure 3.1, the script will consider the pot and the ferrite $\frac{h_c}{2}$ further from a coil with negligible thickness. The results after this approximation have been verified with a FEM simulation and the results of the comparison are showed in section 3.3.

The parameters that must be set as input to the whole computation procedure are listed in table 3.1

The outputs of the script are:

- The impedance seen at the inductor extremities, without the resistance of the coil, that will be calculated separately (see section 3.2.2):

$$Z_{eq_{nc}} = (R_{eq} - R_c) + j\omega L_{eq} = \Delta R + j\omega L_{eq} \tag{3.37}$$

- The current density distribution at different depths of the pot.

As an example, the results for the parameters values in table 3.2 will be evaluated. The geometry have been taken from a real inductor coming from an induction hop present in the laboratory.

The value of the calculated impedance is showed in equation 3.38 while the magnitude of the current density calculated along the pot at different depth is reported in figure 3.3. It is worth saying that the computation is very fast: it takes less than one second.

$$Z_{eq_{nc}} = 5.21 + j\,10.46\,\Omega \tag{3.38}$$

Table 3.1: Input parameters for the Matlab script

Parameter name	Description
Supply	
I_c	Coil peak current
f	Frequency of the current
Inductor	
R_i	Inner radius
R_e	Outer radius
N	Number of turns
h_c	Thickness
Pot and ferrite layer	
h	Airgap between pot and inductor
m	Airgap between pot and ferrite
s_1	Pot thickness
r_1	Pot resistivity
μ_1	Pot relative magnetic permeability

Table 3.2: Parameters values for the first example

Parameter name	Value	Parameter name	Value
Supply		Pot and ferrite layer	
I_c	20 A	h	4 mm
f	50 kHz	m	0.8 mm
Inductor		s_1	1 mm
R_i	18 mm	r_1	$60 \cdot 10^{-8} \, \Omega \cdot m$
R_e	81 mm	μ_1	100
N	21		
h_c	3 mm		

So:

$$\Delta R = 5.21 \, \Omega \tag{3.39a}$$
$$L_{eq} = 33.29 \, \mu H \tag{3.39b}$$

From figure 3.3, it can be seen that the current density is almost concentrated in less than half thickness of the pan (1 mm). In fact, the penetration depth is:

$$\delta = \sqrt{\frac{2\rho}{\omega\mu_0\mu_1}} = 0.174 \, mm \tag{3.40}$$

One more thing to underline is that the current peak value influence only the current density values, while the impedance is not affected, being the system completely linear.
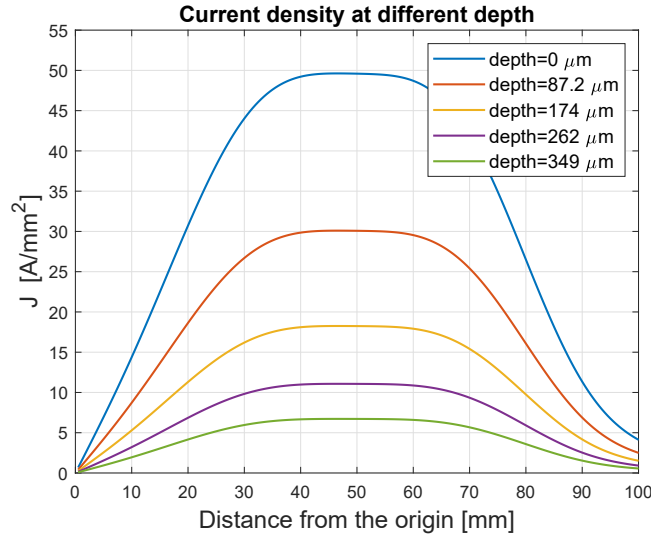
Figure 3.3: Current density evaluated using the script at different depth in the pan

3.2.2   Resistance calculation

The inductor is made of Litz wire. It consist of very thin individually isolated strands wound around each other. The main purpose of this kind of construction is to reduce proximity and skin effect: an increase of the current frequency does not influence the resistance as in a solid conductor where the increase is relevant. An easy and straightforward method for the resistance calculation is presented in [17] and will be reported here. Litz wires used for inductors often present a rectangular cross section with dimensions h_c and L_c. Given the diameter of the strands d_s, the total length of the connection wires l_{conn}, and the stacking factor $skf = \frac{Area\,of\,conductive\,material}{h_c\,L_c}$, the Rdc resistance of the coil is:

$$R_{dc} = \frac{\rho\,l_{tot}}{h_c\,L_c\,skf}$$

$$l_{tot} = l_{turns} + l_{conn}$$

(3.41)

The ac-part of the coil resistance can be obtained as a function of the dc-part by:

$$R_{ac} = R_{dc}\,\frac{1}{k_s}\left(1 + \frac{\beta_r^4}{192 + \beta_r^4}\right)$$

(3.42)

Where:

$$k_s = \begin{cases} 1 & \text{if } \delta > \frac{d_s}{2} \\[2mm] \frac{\frac{d_s}{2}^2 - \left(\frac{d_s}{2} - \delta\right)^2}{\left(\frac{d_s}{2}\right)^2} & \text{if } \delta < \frac{d_s}{2} \end{cases}$$

(3.43)

$$\beta_r^2 = \frac{8\pi f \cdot 10^{-7}}{R_{dc}}$$

(3.44)

The calculation of the parameter δ (skin depth) is already showed in equation 3.40. For the geometry reported in table 3.2, the R_{dc} resistance is $51.1\,m\Omega$ while the ac resistance against

frequency is showed in figure 3.4. It can be seen how small is the variation in the 20-100 kHz range, underlining once more how effective is the Litz wire solution to reduce skin and proximity effects.
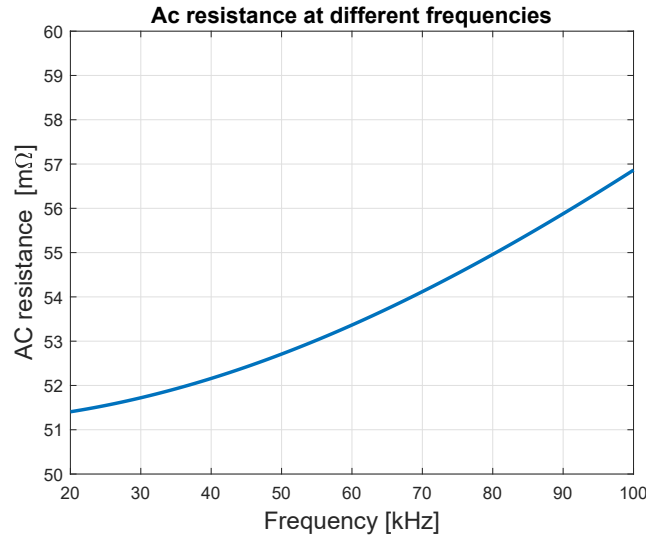

Figure 3.4: Ac resistance of the coil at different frequencies

3.3   FEM modeling

To compare the results of the analytical procedure and verify their accuracy a FEM simulation model has been made using Flux 12.1. A view of the geometry can be seen in figure 3.5a where the axial symmetry have been exploited. On the other hand, the ferrite and pot layer could not be infinitely large as the analytical method consider, but it has been verified that if their radial extension is about 10 % bigger that the external radius of the inductor, the solution is then not influenced by further increasing the dimensions. The aim of this section is to present the FEM model setup in order to have a way to compare the results of the analytic procedure with a more reliable method. Further in this thesis, the model will be improved with non linearities of the materials, and more deep analysis of magnetic phenomena will be presented. The characteristics of each region are listed in table 3.3, while the circuit configuration can be seen in figure 3.5b. The model is solved as an AC steady state magnetic 2D problem.

Table 3.3: Regions type and parameters

Region	Type	Parameters
Ferrite	Magnetic non conducting region	$\mu_{ferr} = 10000$
Inductor	Coil conductor region	$N = 21, R = 53\,m\Omega,$
Pot	Solid conductor region	$\rho_{pot} = 60 \cdot 10^{-8}, \mu_{pot} = 100$
Air	Air or vacuum region	

A comparison between the current densities induced in the surface of the pot is showed in figure 3.6: the graph shows the goodness of the analytical results compared with the FEM one.

(a) Geometry for the FEM model
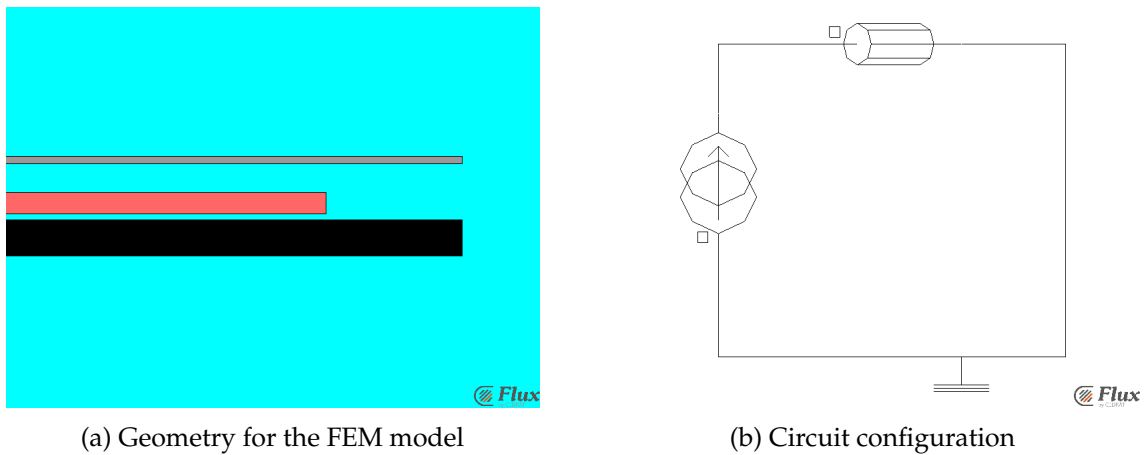

(b) Circuit configuration
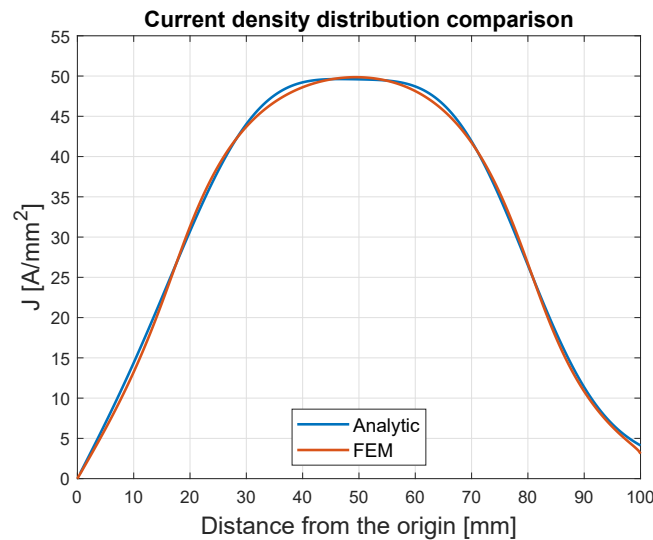
Figure 3.5: Flux geometry and circuit setup

Figure 3.6: Surface current density distribution for different computation methods

Also the impedance seen at the inductor extremities have been computed, with this results (to compare with results in 3.39):

$$\Delta R = Re\left(\frac{\overline{V}_{coil}}{\overline{I}_{coil}}\right) = 5.21\,\Omega \tag{3.45a}$$

$$L_{eq} = Im\left(\frac{\overline{V}_{coil}}{\overline{I}_{coil}}\right)\frac{1}{\omega} = 32.26\,\mu H \tag{3.45b}$$

3.4   Saturation of the pot: an iterative method

In section 3.2 it has been showed how the impedance seen by the inverter and the current density in the pot is analytically computed. As already mentioned, that procedure consider a constant relative permeability of the pot, so the saturation phenomena that could be appear is not taken into account. In other words, the B-H curve for the stainless steel is considered linear. By the way, starting from medium power levels the magnetic flux is very high in the pot which leads

the steel to be already in the saturation zone of the B-H curve. Given the impossibility to find a correct current density distribution, if μ_{pot} is not constant, is there any equivalent μ_{pot} that gives the same impedance computation using the analytical procedure, compared to a FEM one?
In order to find the answer to this question, the Matlab script presented in section 3.2 have been further improved:

- The Magnetic field **H** in the pot is calculated
- The magnetization characteristic of the stainless steel is found
- An equivalent relative magnetic permeability of the pot $\mu_{pot_{eq}}$ have is derived

After those calculations, a Matlab procedure have been created in order to repeat the routine until the convergence of the method is found and a final value of $\mu_{pot_{eq}}$ is considered.

3.4.1   Analytical calculation of H field

Starting from the current density known in several points of the pot, the magnetic field **H** can be analytically computed. In fact from equation 3.9, considering that $\mathbf{E} = \rho_{pot}\mathbf{J}$ and $\frac{d}{dt} = j\omega$:

$$\rho_{pot}\, J_\varphi(r,z) = -j\omega\, A_\varphi(r,z) \tag{3.46}$$

So the expression for the vector potential is:

$$A_\varphi(r,z) = j\frac{\rho_{pot}}{\omega}\, J_\varphi(r,z) \tag{3.47}$$

To find the B field, the rotor of $A_\varphi(r,z)$ must be done in cylindrical coordinates:

$$\begin{aligned}
\mathbf{B}(r,z) &= \boldsymbol{\nabla} \times A_\varphi(r,z) \\
&= (-\frac{\partial A_\varphi}{\partial z}, 0, \frac{A_\varphi}{r} + \frac{\partial A_\varphi}{\partial r})
\end{aligned} \tag{3.48}$$

This formula have been applied to find the r and z coordinate of the B field in the pot. To be accurate in the calculation, the current density in the pan must be computed in a high number of points. The evaluated current density and the B field comparison at the surface, for the geometry of table 3.2, is showed in figure 3.7. As can be seen, the pictures show very good agreement between analytical anf FEM computation. Once **B** is found, **H** can be easily derived as $\mathbf{H} = \frac{\mathbf{B}}{\mu_0\,\mu_{pot}}$ since the relative permeability is constant and known.

3.4.2   B-H curve for magnetic stainless steel

In the process to find the equivalent relative permeability, the B-H curve for the stainless steel that is placed in the bottom of the pan is necessary. The materials used for the bottom of the pan are usually AISI 409 or 430. They are magnetic stainless steels. It is quite difficult to find the correct values for the BH curve, because:

- The curve values depends on the type of treatments and process that the material has experienced
- The magnetization curve measurement is expensive so companies tend to not publish the results for free, keeping everything for themselves as an industrial secret

(a) Analytical evaluated current density
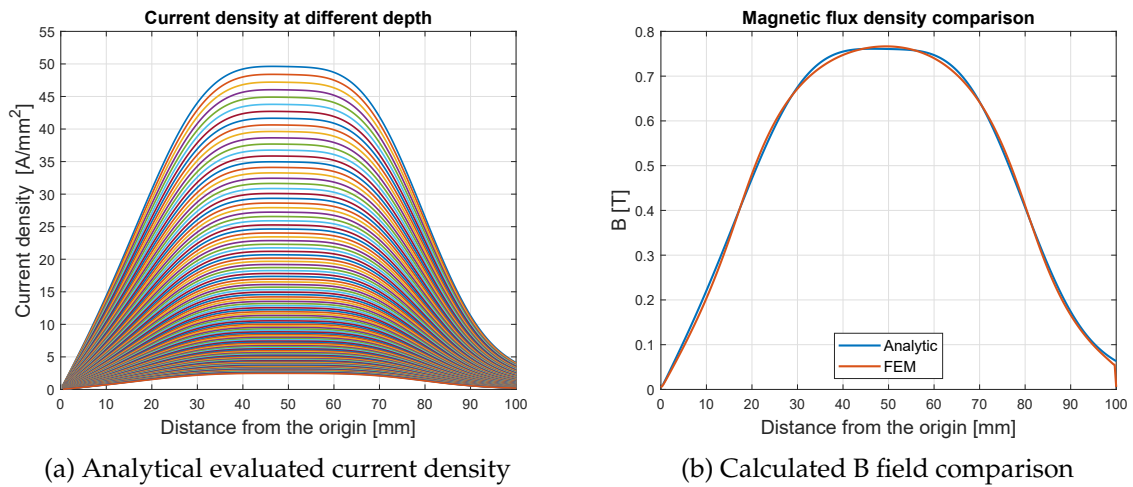
(b) Calculated B field comparison

Figure 3.7: Current density distribution used for the B field calculation and comparison with FEM of the field calculated at the surface

The first magnetization curve will be used: the hysteresis effect will be neglected. It is a typical assumption that is considered also when working with FEM software. Usually the following parametric function is used for representing the curve:

$$B(H) = \mu_0 H + \frac{2B_s}{\pi} \tan^{-1}\left(\frac{\pi(\mu_{r_i} - 1)\mu_0 H}{2B_s}\right) \tag{3.49}$$

Where B_s is the saturation flux density and μ_{r_i} the in initial relative magnetic permeability. So, with this relation, only two parameters are necessary to have a complete curve. Some data can be found in the literature, as in [18] for example, where is reported $B_s = 1.47\,T$ and a range $\mu_{r_i} = 1100 - 1600$ for AISI 430. Based on others little informations from people in the laboratory who has more experience, the suggestion was to choose μ_{r_i} close to 2000, since the AISI 409 is more magnetic than the 430, so the final value chosen for μ_{r_i} is 1600. The curves resulting can be seen in figure 3.8 where the classic BH relation and the μ_r against H are showed.
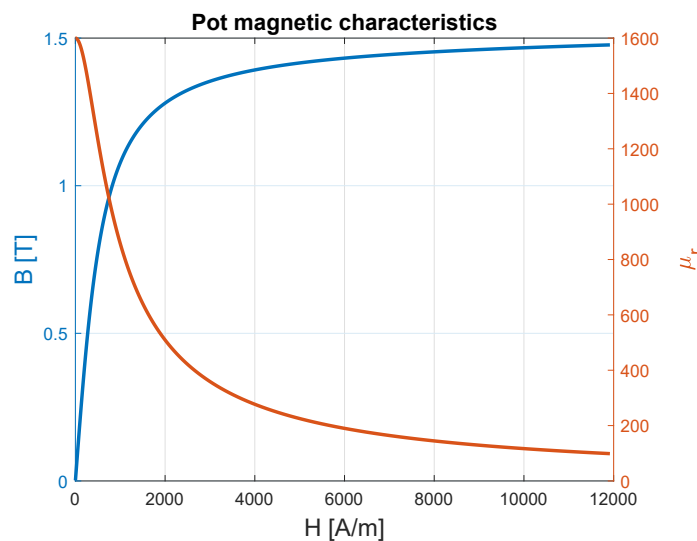

Figure 3.8: Magnetization curve for the pot material

3.4.3   Calculation of the equivalent relative permeability

Up to now, with a constant, user defined, permeability, the analytic procedure calculate the current density and the B (or H) distribution on the pan. Since the relationship with those values is well established by the curves showed above, the aim of this step of code improvement is to find a permeability that correspond to a specific, calculated, H field value. In other words, μ_r must not be randomly decided by the user, but it should be found from the calculated H distribution. An iterative process have been implemented with this aim:

1. The geometry, materials parameter, supply current and frequency are set once at the beginning and kept constant throughout all the iterative process.

2. A starting value for μ_{pot} is chosen by the user.

3. The impedance seen at the load extremities and the current density are computed as described in sections 3.2.1 and 3.2.2.

4. The H field is calculated in all the points of the pot as showed in section 3.4.1.

5. Using the curve showed in figure 3.8, at each point is associated a relative permeability value, interpolating the function 3.49.

6. $\mu_{pot_{eq}}$ is found calculating the mean of all the permeability values associated to the points (r, z) of the pot that satisfy the following relation (according to the coordinate system in figure 3.1):

$$\begin{cases} R_i < r < R_e \\ -1.85\,\delta < z < 0 \end{cases} \tag{3.50}$$

7. The iterative process starts again from step 3 of the list, and each time the input relative permeability is the value calculated at phase 6.

The process stops when the variation of $\mu_{pot_{eq}}$ between two consecutive steps is less than 0.5. To better understand how the process works, in figure 3.9 the effective pot zone for the equivalent relative permeability calculation is showed, while in figure 3.10 a syntesis of the iterative method presented in this section is represented.
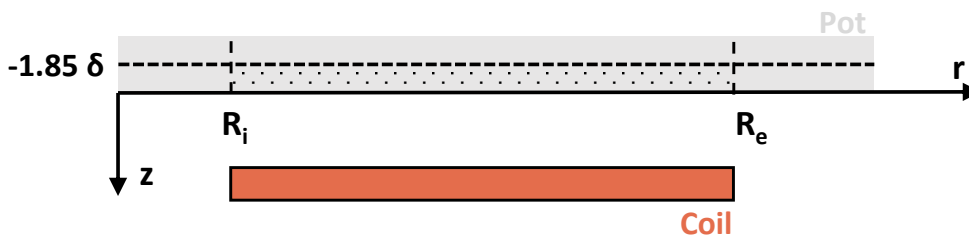

Figure 3.9: Pot and inductor with highlighted area for the computation of $\mu_{pot_{eq}}$

One thing that must be explained is why such a choice for the limits showed in equation 3.50. As it should be understood, those limits restrict the volume of the pot where the relative permeability is evaluated, so the total mean value, which is $\mu_{pot_{eq}}$, will be affected. In particular that $1.85\,\delta$ have been chosen comparing the results of the iterative process with FEM simulations and how that value is found will be discussed in the next section.

The aim is now to understand how those limits affect the impedance computation. The first thing to remark is that the current density (and so the H field) is limited in a very small part of the pot: the inductor size in the radial direction, three penetration depths in the z direction.
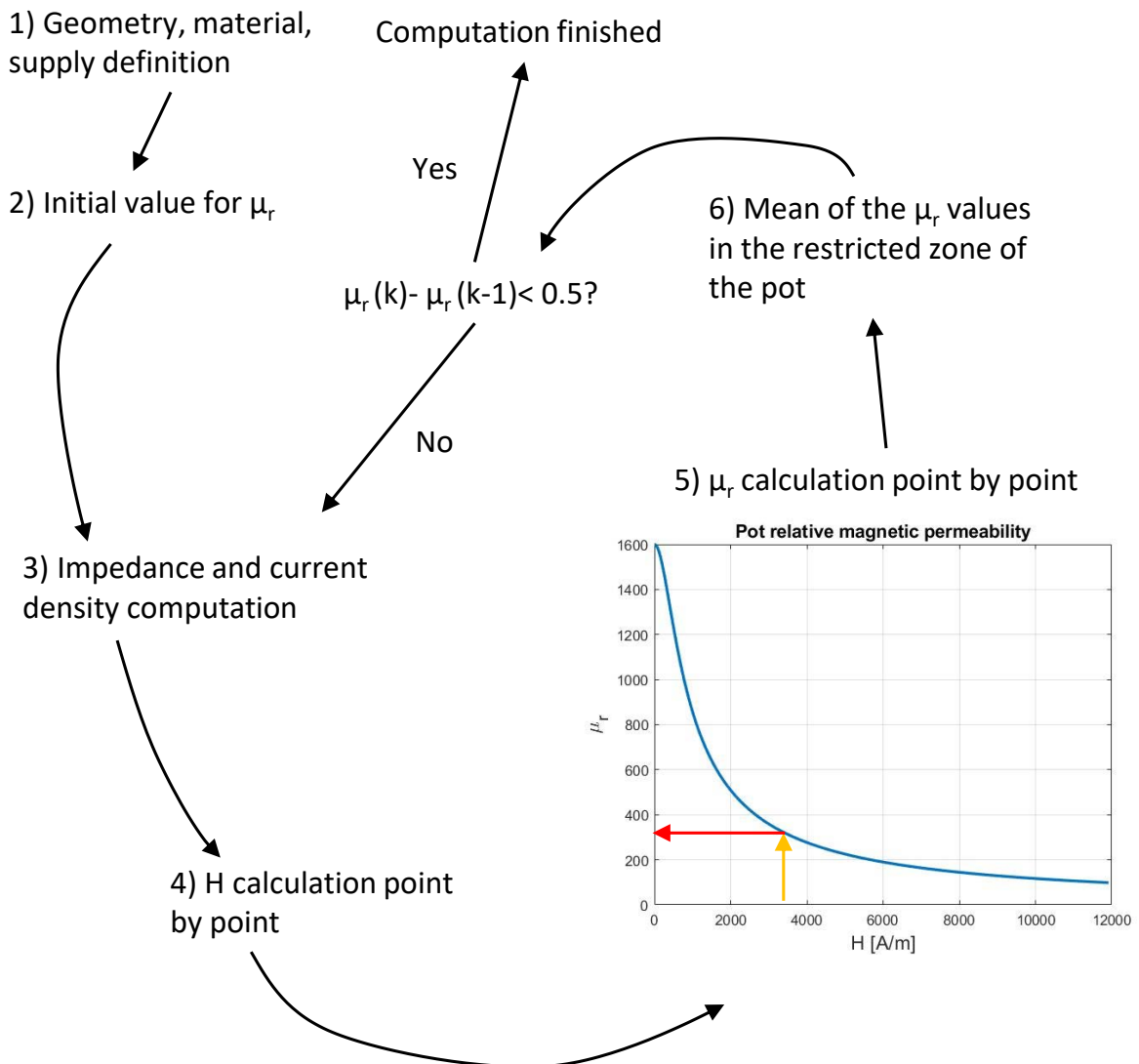
Figure 3.10: Recapitulation of the iteration process to find the equivalent relative permeability of the pot

Where the current density is high, the H field is high, and so the permeability is low, the other way around holds for the zone of the pot with very low eddy current. This can be seen in figure 3.11.

Given the supply current value in the pot, the more the limits are closer to the area of the pot where eddy current are concentrated, the less is the mean value of the relative permeability.

The iterative method has a very fast convergence, it takes no more than 4 iterations to reach the stop condition, for a large amount of supply current and starting permeability value. For the usual geometry under example (table 3.2) the method reach the convergence for $\mu_{pot_{eq}} = 572$. The value for the equivalent relative permeability depends on the geometry, but mainly on the supply current. In fact the saturation effect heavily depends on the magnetic field value which

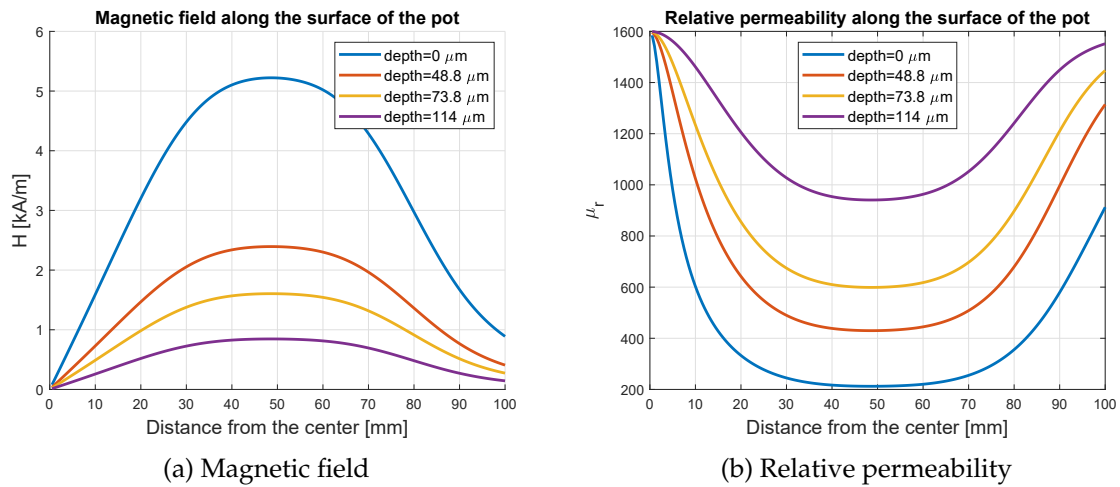(a) Magnetic field   (b) Relative permeability

Figure 3.11: Analytical magnetic field and relative permeability evaluated at different depth of the pot

is directly proportional to the current flowing in the inductor: the more, the less is $\mu_{pot_{eq}}$, as can be seen in figure 3.12.
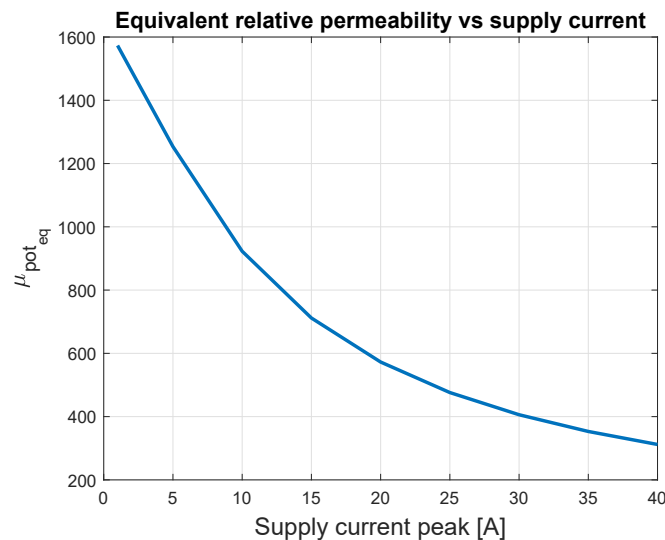

Figure 3.12: Equivalent relative permeability with different values of the peak supply current

3.5 Comparison between analytic and FEM technique, including saturation

After the explanation of how the analytic iterative method works, it is now necessary to compare the results with the FEM simulation and see if a value of constant permeability given to the pot in the analytic procedure, can lead to a Z_{eq} computation that is close to the reality. The B-H curve in figure 3.8 have been applied to the pot material in the FEM model.

The 1.85 δ (upper limit value for the calculation area of the $\mu_{pot_{eq}}$) have been found empirically. Such value is the value that, for the most range of geometries, current and frequencies leads to

an analytical calculation of R_{eq} which is close (error less than 3%) to the real value found using the FEM simulation. The error in the calculation for the equivalent resistance and inductance have been calculated in the following way:

$$R_{err} = \frac{R_{eq_{analytic}} - R_{eq_{FEM}}}{R_{eq_{FEM}}} \tag{3.51a}$$

$$X_{err} = \frac{L_{eq_{analytic}} - L_{eq_{FEM}}}{L_{eq_{FEM}}} \tag{3.51b}$$

The results, for different values of frequencies and currents, are showed in figure 3.13, considering the geometry in table 3.2. As can be seen, while the error in the resistance value is very limited (it stays in the $\pm 3\%$ range) the error in the equivalent inductance is much higher and tend to the 30 %.

(a) Error in the equivalent resistance   (b) Error in the equivalent inductance
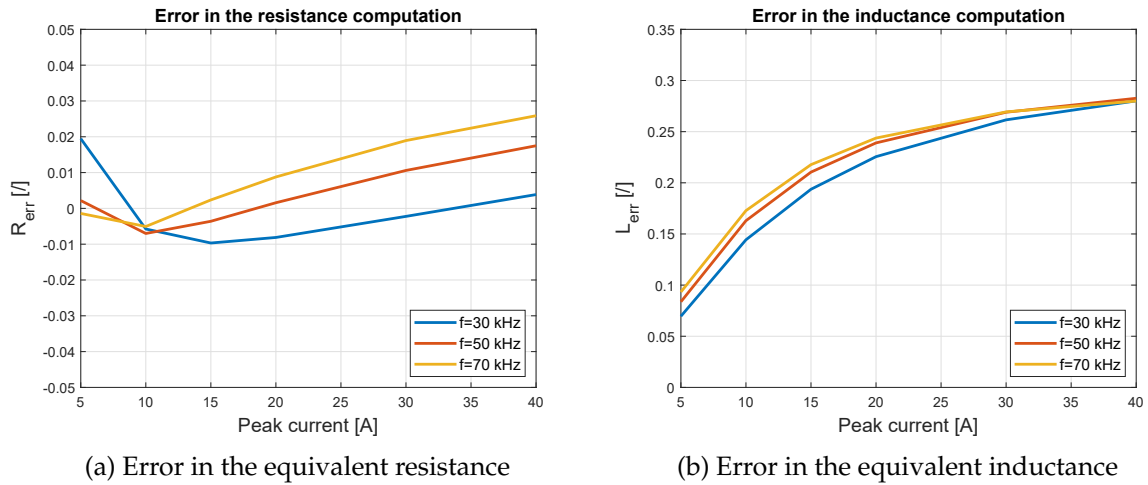
Figure 3.13: Error in the equivalent impedance

The physical reason for this discrepancy in the errors can be analysed and explained. To understand why the equivalent resistance can be equal, even if the current density distribution is not the same, the formulas 3.32 and 3.33 must be taken into account. In fact, same R_{eq} means same power in the pot and, in turns, means that the integral of the square of the current density in the volume of the pot is the same: this can also happen with different distribution of $J_\varphi(r,z)$. One example that can prove this assumption is showed in figure 3.14a: even if the current density distribution is not the same, the area under the two curves is equal, and this is what happen throughout all the pot. In fact, since the real permeability of the pot computed with the FEM method is lower in the bottom part of the pot (figure 3.14b), the penetration depth is higher so its distribution decrease less rapidly compared to the analytical solution: in the lower part of the pot $J_{an} > J_{FEM}$ because $\mu_{an} > \mu_{FEM}$, while in the top part of the pan $J_{an} < J_{FEM}$ because $\mu_{an} < \mu_{FEM}$.

On the other hand, the motivation for being $X_{eq_{mat}} >> X_{eq_{FEM}}$, as showed in picture 3.13b, can be understood with the help of picture 3.15. In the part of the pot where the most current density is present $\mu_{an} > \mu_{FEM}$, so the magnetization effect is enhanced: the reluctance seen by the m.m.f produced by the coil is lower and so an higher magnetic flux density flow, accordingly to the Hopkinson law for the magnetic circuits.

(a) Current density comparison
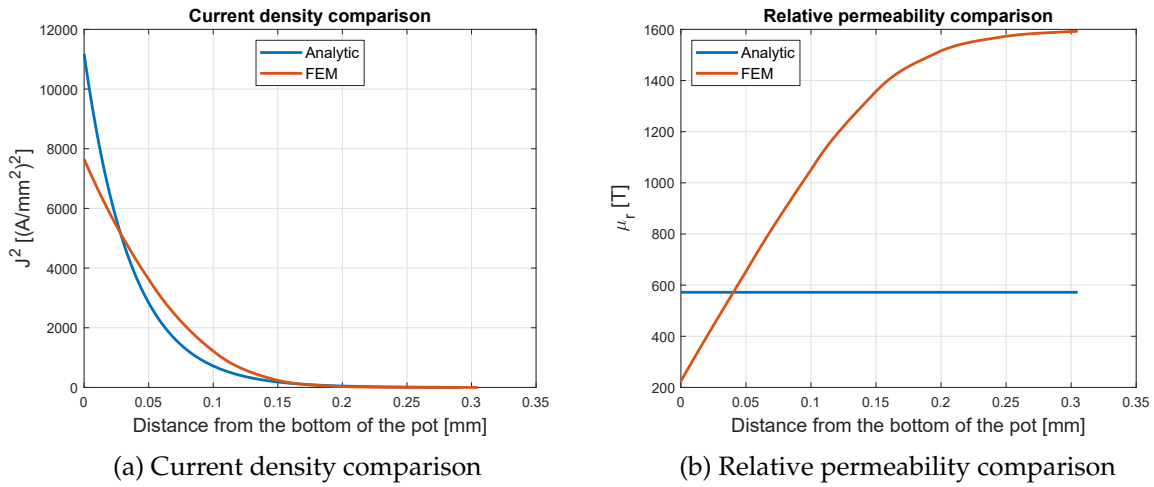
(b) Relative permeability comparison

Figure 3.14: Comparisons of current density and relative permeability between analytical and FEM computation methods along a vertical path at a radius of $r = \frac{R_e + R_i}{2}$
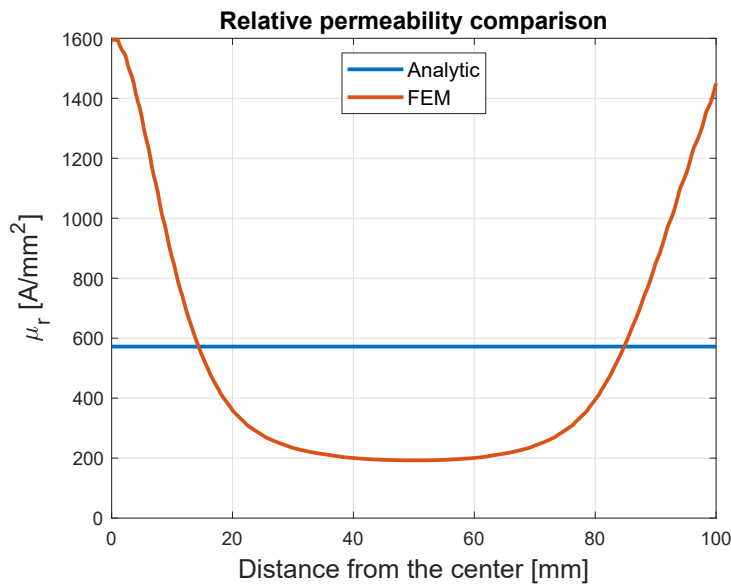

Figure 3.15: Relative permeability distribution comparison at the surface of the pot

3.6 Conclusions

The aim of the procedure explained in this chapter was to find a possible way to include saturation effects in the analytic computation of the impedance seen by the inverter. All the methods developed have been explained with some results. It has been verified that it is impossible to find a unique value of equivalent relative permeability that leads to a correct computation of both R_{eq} and L_{eq}. In fact, even if R_{eq} is correctly calculated, L_{eq} is overestimated. The pysical reasons behind those aspects have been deeply explained. On the other hand, the procedure requires very low computation time to find $\mu_{pot_{eq}}$, compared to the FEM one: it takes less than 20 seconds to obtain the equivalent permeability with a current of 20 A and a starting value of 400.

A more detailed statistical analysis in different geometries would lead to a deeper knowledge

on the relation between the error and the geometry, leading to a possible use of this presented technique.

Chapter 4

Improved load power control scheme

In this chapter, the load active power control topic will be treated. In the first part, the possible techniques that can be adopted to adjust the active power tranferred will be investigated and analysed. The converter under test will be the half bridge since, as explained in section 2.2, it is the best compromise between cost and quality for cooking applications. The circuit of such topology is reported again in figure 4.1.
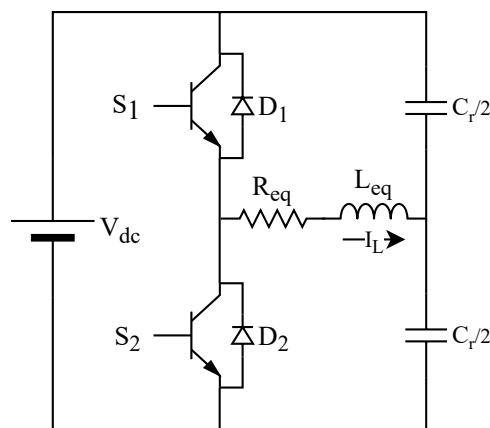

Figure 4.1: Circuit diagram for the half bridge inverter

In the second part of the chapter, some of the basic techniques described will be applied to a real case of induction load in order to build a novel control strategy, that achieves low load active powers without using the PDM strategy.

4.1   Load power control techniques

In this section, each strategy will be presented and discussed with results from analytical and circuital simulations. The analytic waveforms derived and the simulink model that allows to model and simulate the converter in the SWM and ADC mode are mostly the same of what discussed in section 2.2.3, so the waweforms presented will be similar to those already seen, then it won't be explained how the timing of the switch is managed. On the other hand, for the DCM control it have been necessary to create another Matlab procedure, so a little bit more detailed explanation will be given.

Since the aim of this chapter is to show how the different control techniques works, the equivalent impedance of the load will be kept constant regardless the frequency and current magnitude of the supply. In section 4.2, where the power value in the pot will be the main topic, the real load variations will be taken into account.

4.1.1 Square wave modulation (SWM)

This type of power control change the active power in the load by varying the switching frequency: when f_s is equal to the resonant frequency, the power is maximum, and the more f_s is high, the less is the active power transferred to the load, the other way around holds for the reactive power. The resonance capacitor value is set in order to obtain a resonance frequency $f_0 = 20\,kHz$:

$$C_r = \frac{1}{(2\pi f_0)^2\, L_{eq}} = 1.81\,\mu F \tag{4.1}$$

Another parameter that affect the power values in the load is the so called "Quality factor" which expression is:

$$Q = \frac{\omega_0\, L_{eq}}{R_{eq}} \tag{4.2}$$

The quality factor influence the rapidity with which the power decrease when the switching frequency decrease. The peak power value doesn't change. To show this assumption, the power for the loads values showed in table 4.1 will be evaluated. The resonant capacitor is changed for each load to keep the resonance frequency to 20 kHz. The procedure for the power calculation is done using the Matlab scripts already presented in section 2.2.3.4.

Table 4.1: Load values for power computation

Load n°	R_{eq} [Ω]	L_{eq} [μH]	C_r [μF]	Q [-]
1	7	35	1.81	0.63
2	7	70	0.904	1.26
3	7	140	0.452	2.51

The power in the load for different frequencies is showed in figure 4.2. It can be seen that for higher Q values the power decrease faster, in fact when L_{eq} is higher, as soon as the switching frequency deviate from f_0, the inductive reactance $\omega\, L_{eq}$ prevail on the capacitive reactance $\frac{1}{\omega\, C_r}$ and the active power suddenly drop. On the other hand, induction loads usually have very low Q values: a Q of 2.51 like in load n°3 is very difficult to obtain.

As an example, the load current for different frequencies with load number 1 is showed in figure 4.3.

With the presence of the snubber capacitance the load power is lower, but the difference compared to the ideal case with no deadtime is negligible. In addition, it must be said that the more the frequency the more the switching losses in the converter, which lead to a decreased efficiency of the system. Some literature about the SWM can be found in [19].
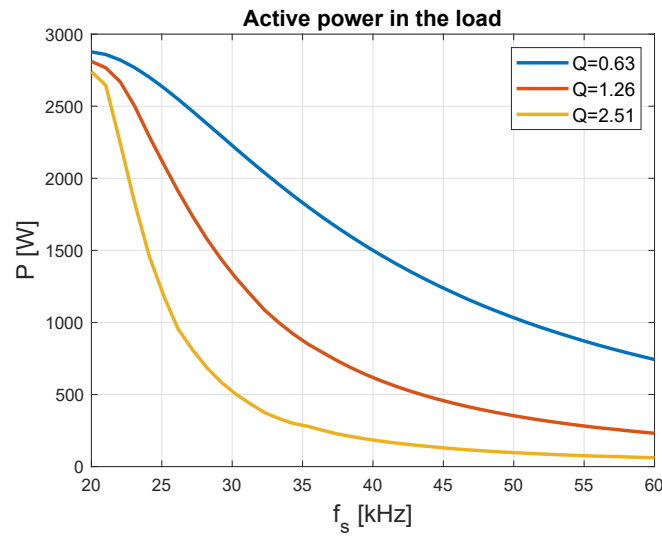
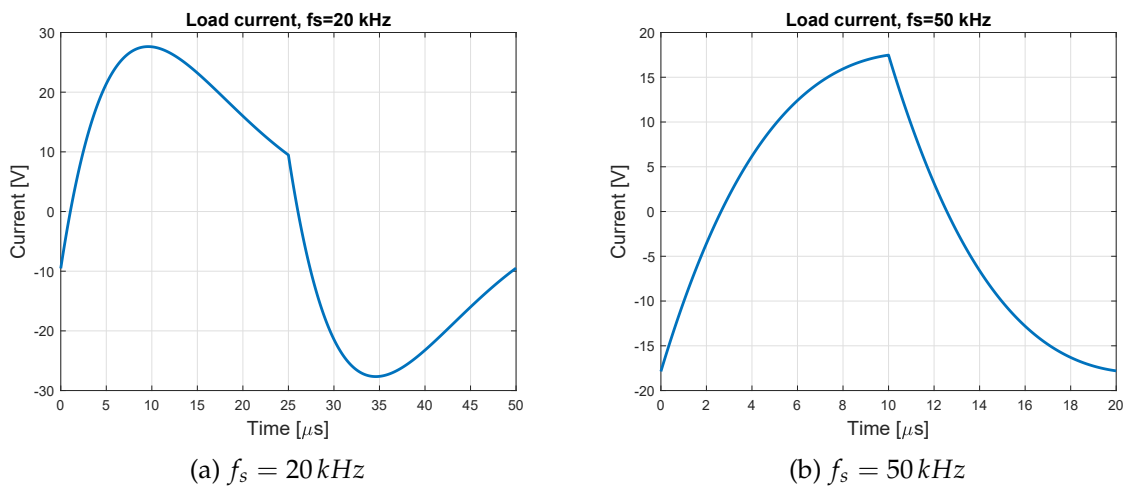Figure 4.2: Power in the load for different Q factors

(a) $f_s = 20\,kHz$

(b) $f_s = 50\,kHz$

Figure 4.3: One period of the load current for different frequencies

4.1.2   Asymmetrical duty cycle modulation (ADC)

The second power control method that will be explained in this section uses the frequency and the duty cycle to control the power transferred into the load. As the SWM technique, the increase in the frequency correspond to a decrease of the active power in the pan but, in addition, the duty cycle of the switches is used as another "knob" for the regulation. In fact, while normally the switches works with 50% duty cycle (in the reality it is lower, due to the mandatory presence of the deadtime), if it is decreased (the top switch stays on less time than the bottom switch) or increased (the top switch stays on more time than the bottom switch) the power in the load drops. The more the duty cycle deviates from the 50%, the more the power decrease.

To understand how this control works, the system will be initially analysed without the lossless snubber and deadtime. The load is (as in the SWM) $R_{eq} = 7\,\Omega$, $L_{eq} = 35\,\mu H$, $C_r = 1.81\,\mu F$. In figure 4.4 the power is displayed against the switching frequency and the duty cycle, to confirm what just explained: the power drops when the duty cycle decrease and when the switching frequency increase.
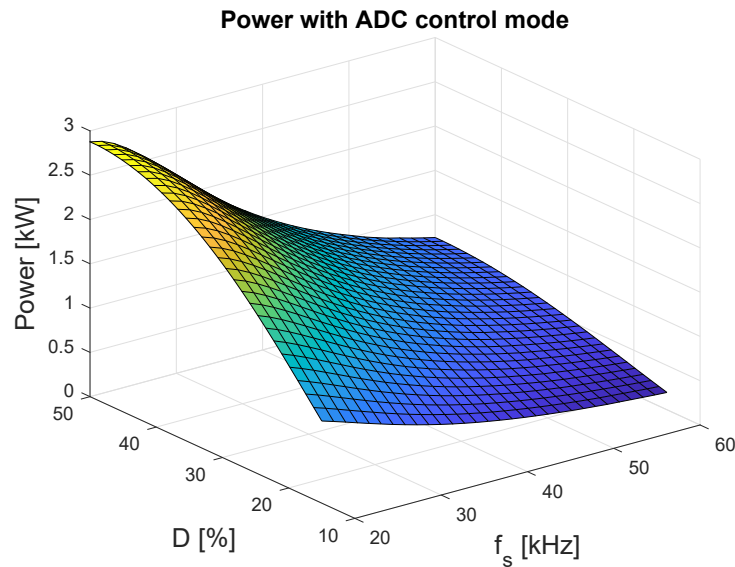
Power with ADC control mode

Figure 4.4: Power in the load with ADC control mode, deadtime and lossless snubber are neglected

As an example, to show how the duty cycle affect the load current, in figure 4.5 the waveforms for a duty cycle of 0.25 and 0.75 are showed. Those two particular values of D because they are equally far from $D = 50\,\%$: the rms value of the two currents is the same. In fact, it can be easily seen that the raising period in figure 4.5b is just the shifted opposite of the falling period in figure 4.5a. It is confirmed that, in terms of active power in the load, the duty cycle D has the same effects of a duty cycle $1 - D$. For this reason, from now on, only duty cycles less than 0.5 will be taken into consideration, without loss of generality.
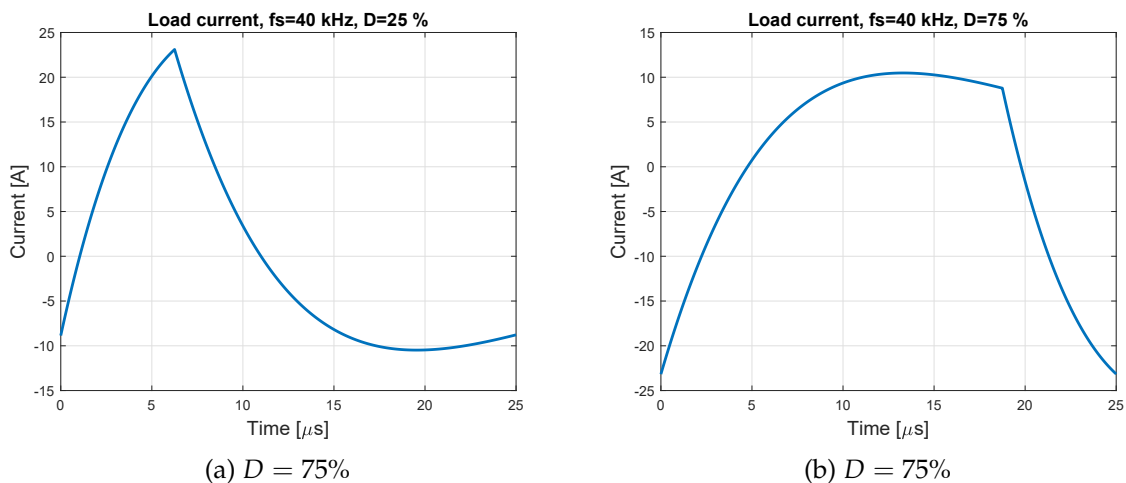

(a) $D = 75\%$ (b) $D = 75\%$

Figure 4.5: Load current at $f_s = 40kHz$, with "opposite" duty cycles

One drawback of this kind of control technique is the asymmetrical devices utilization factor. While in the SWM the converter works in a symmetric way (the voltage and the current in the switch are just 180° shifted, but equal in magnitude) in the ADC, on the other hand, the switch that has the lower duty cycle (the top one if $D < 0.5$, the bottom one if $D > 0.5$) must open an higher current than the switch with the higher duty cycle. In figure 4.5 it's $\simeq 23\,A$ for the switch

more stressed and $\simeq 8\,A$ for the less stressed one.

Another drawback is the reduced ZVS operation range. In fact, if the lossless snubber together with the deadtime are considered, it is not difficult that situations like what showed in figure 2.10 can happen:

- the frequency is close to f_0: the bottom switch conduction time is close or higher than $\frac{f_d}{2}$ so when it is time to switch off there isn't enough negative output current to discharge both snubber capacitors (figure 4.6a)

- the duty cycle is very small ($< 20\,\%$): during the on time the current doesn't rise enough to a value that allows to discharge both snubber capacitors when the top switch turns off (figure 4.6b)

(a) $f_s = 20\,kHz\,D = 25\,\%$
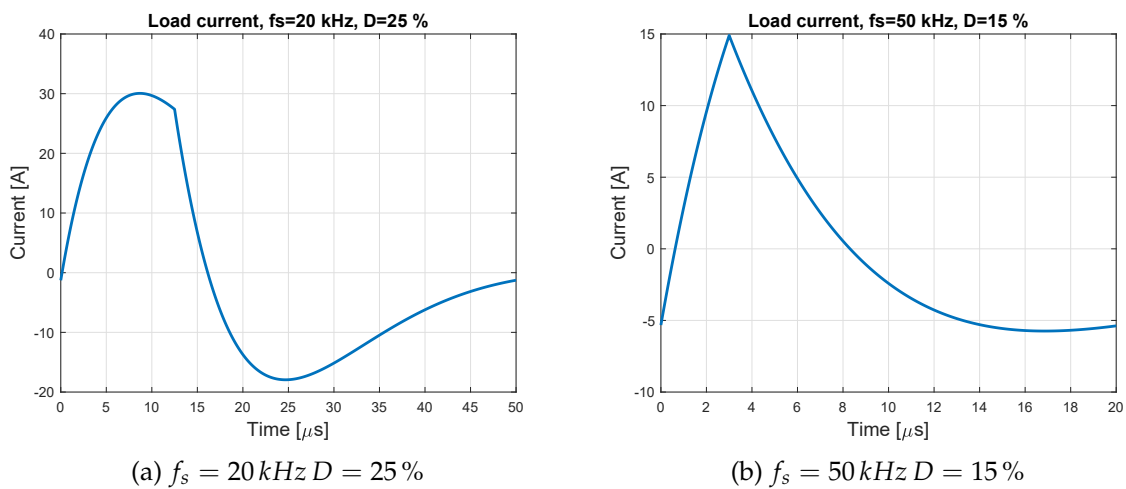

(b) $f_s = 50\,kHz\,D = 15\,\%$

Figure 4.6: Load current examples to show how the ZVS cannot be achieved

The overall view of the cases where the ZVS can be achieved for different duty cycles and switching frequencies can be seen in figure 4.7, when a deadtime of $1\mu s$ and the snubber capacitors are $10\,nF$. When the power is zero, it means that the ZVS condition is not achieved.

(a) Power against switching frequency, for different duty cycles

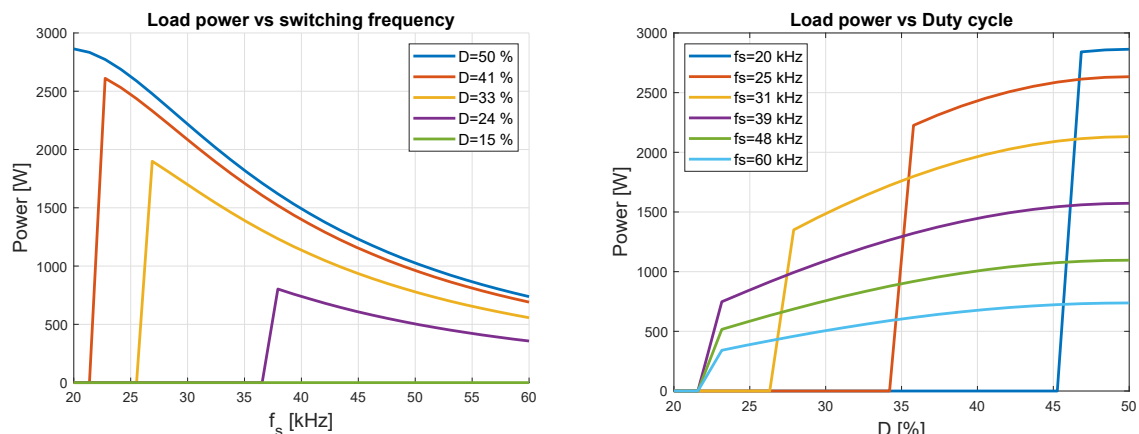(b) Power against duty cycles, for different switching frequency

Figure 4.7: Power in the load with ADC control mode, including the effect of Lossless snubber and deadtime ($t_{dt} = 1\mu s$, $C_s = 10nF$)

From the figures it can be concluded that the more is the frequency high, the less duty cycle values allow the ZVS condition to be satisfied. In addition, there is a lower duty cycle limit where no switching frequency can allow a safe work of the converter. In this example, with a duty cycle of 22 % no ZVS is achieved.

Some literature about the ADC can be found in [19] and [20].

4.1.3 Pulse density modulation (PDM)

This modulation technique is used for the medium/low power range. Keeping the switching frequency constant, the inverter is enabled and disabled at intervals of some seconds. When the inverter is on, it supplies the coil using the SWM technique and then, after some seconds, all the four switches are disabled and the inductor is not supplied at all. A scheme of such technique can be seen in figure 4.8.
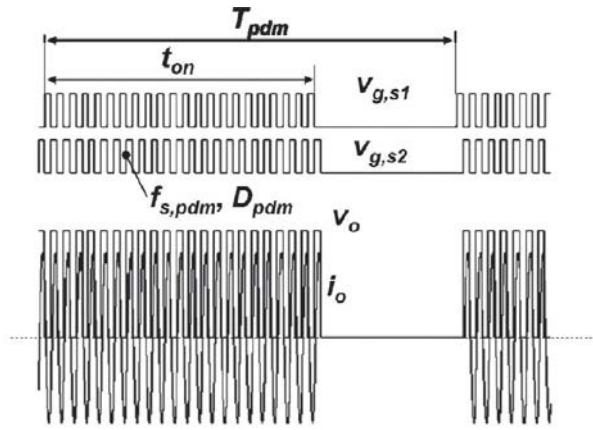

Figure 4.8: PDM main waveforms and parameters [19]

The medium/high frequency range is supplied with the SWM technique. As can be seen in figure 4.2, very low power level cannot be reached even at very high frequencies, so to achieve lower level a transition from SWM to PDM is done. As explained in [19], the change in the modulation technique can be done based on reaching a certain switching frequency or power level. The control parameters are the duty cycle of PDM (D_{PDM}) and the pulse period T_{PDM}:

$$D_{PDM} = \frac{t_{on}}{T_{PDM}} \tag{4.3a}$$

$$P_{load} = P_0 \, D_{PDM} \tag{4.3b}$$

where P_0 is the power supplied to the load at such switching frequency in the SWM. The load power is linear with D_{PWM}. Typical values range for T_{PDM} is from 2 to 4 seconds. One of the main drawbacks of this strategy is that the power is discontinuous, and the user can note boiling pulses. In addition, such control strategy can create flicker problems due to the discontinuous load power supply. One advantage of this strategy is the switching frequency reduction and the linear power control.

This type of control have not been deeply analyzed due to its simplicity but mainly because the novel control method that will be proposed in section 4.2 will have the aim to provide low power levels to the load without using the PDM strategy. Some literature about the PDM can be found in [19], [21] and [22].

4.1.4 Discontinuous current mode (DCM)

The last control technique showed is based on obtaining a zero inductor current so that the inverter operates in discontinuous mode, in fact in each cycle there is a period of time when both switches are off. The load considered for the analysis will be (as usual in all section 4.1) $R_{eq} = 7\,\Omega$, $L_{eq} = 35\,\mu H$. The working operation of the inverter with this control mode will be analysed step by step considering the different states of switches and diodes, that are summarized in table 4.2

Table 4.2: Operations mode summary of the half-bridge inverter working in DCM

MODE	I_L	S_1	S_2	D_1	D_2
A	> 0	x			
	< 0			x	
B	$= 0$				
C	< 0		x		
	> 0				x
D	$= 0$				

While in the SWM and ADC control the resonant frequency of the load was set at 20 kHz, in the DCM the resonant capacitor C_r is set in order to have $f_d = 80\,kHz$. As will be seen in the next section, to decrease the power in the load the switching frequency must be decreased (contrary to SWM and ADC control) without falling in the audible range (from 20 Hz to 20 kHz). So the resonant capacitor value is $C_r = 107\,nF$. Further explanation will be done below.

4.1.4.1 Mode A and B

At the time $t = 0$ the switch S_1 starts conducting, the initial conditions are:

$$v_c(0) = V_{c0} \tag{4.4a}$$
$$i_L(0) = 0 \tag{4.4b}$$

The current initially rises and the self oscillation of the load starts. The current firstly increases and then decrease reaching zero again at the time t_0, when the antiparallel diode takes the conduction. During Mode B the switch is turned off (ZVS) and ends when the current returns to zero at the instant t_1. The analytical expressions for the capacitor voltage and inductor current for $0 < t < t_1$ are:

$$v_{c_1}(t) = V_{dc} + (V_{c0} - V_{dc})\, e^{-\alpha t}\left(cos(\omega_d t) + \frac{\alpha}{\omega_d} sin(\omega_d t)\right) \tag{4.5a}$$

$$i_1(t) = \frac{V_{dc} - V_{c0}}{\omega_d L_{eq}} e^{-\alpha t} sin(\omega_d t) \tag{4.5b}$$

At the time t_1 the conduction of D_1 ends and no switches are ON (Mode B) until the time t_2. The values at the time t_1 are:

$$v_{c_1}(t_1) = V_{c1} = V_{dc} + (V_{c0} - V_{dc}) e^{-\alpha t_1} \tag{4.6a}$$
$$i_1(t_1) = 0 \tag{4.6b}$$

The analytical expressions for the capacitor voltage and inductor current for $t_1 < t < t_2$ are:

$$v_{c_2}(t) = V_{c_1} \tag{4.7a}$$
$$i_2(t) = 0 \tag{4.7b}$$

The time instants t_0, t_1 are particular values that depends on the load parameters, while t_2 depends on the switching frequency:

$$t_0 = \frac{\pi}{\omega_d} = \frac{1}{2 f_d} \tag{4.8a}$$
$$t_1 = \frac{2 pi}{\omega_d} = \frac{1}{f_d} \tag{4.8b}$$
$$t_2 = \frac{1}{2 f_s} \tag{4.8c}$$

So, the duty cycle of the switch is ideally $D = \frac{t_{on}}{T_s} = \frac{t_0}{f_s}$ but in reality it is turned off a bit later the zero crossing of the current.
The current and voltage waweforms in the load during mode A and B can be seen in figure 4.9.

(a) Load current

(b) Capacitor voltage

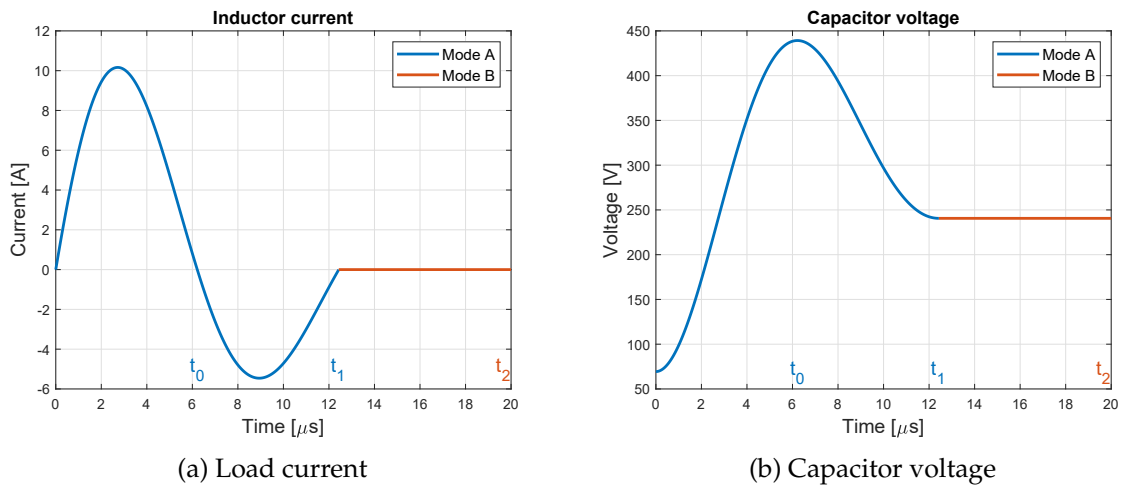Figure 4.9: Waveforms in the load during mode A and B, for a switching frequency of $f_s = 25\,kHz$

4.1.4.2 Mode C and D

Regarding mode C and D, it is not necessary to analytically solve the problem again, but since those two modes consist of the second half of the switching period, it holds that, for

$t_2 < t < t_2 + t_1$ (Mode C):

$$v_{c_3}(t) = -v_{c_1}(t - t_2) + V_{dc} \tag{4.9a}$$
$$i_3(t) = -i_1(t - t_2) \tag{4.9b}$$

While for $t_2 + t_1 < t < 2t_2$ (Mode D):

$$v_{c_4}(t) = -v_{c_1}(t - t_2) + V_{dc} \tag{4.10a}$$
$$i_4(t) = 0 \tag{4.10b}$$

4.1.4.3   Overall considerations

A full period of the load waweforms is displayed in figure 4.10:
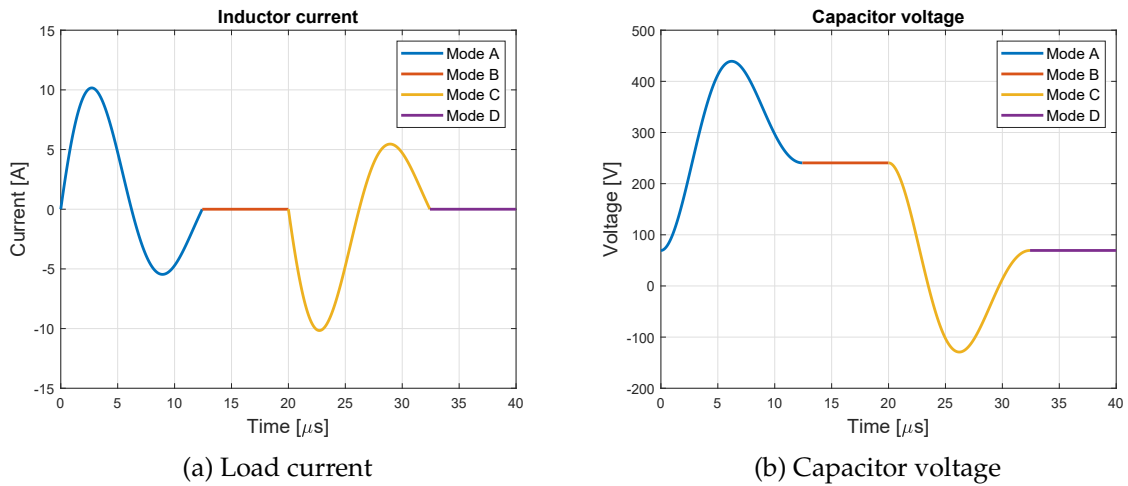

(a) Load current

(b) Capacitor voltage

Figure 4.10: One period waveforms in the load for a switching frequency of $f_s = 25\,kHz$

The steady state capacitor starting voltage can be analytically calculated and the procedure can be understood looking at figure 4.11. It is easy to understand that this condition must be valid in the steady state regime:

$$V_{dc} - V_{c1} = V_{c0} - 0 \tag{4.11}$$

Considering now equation 4.6a, equation 4.11 becomes:

$$V_{dc} - V_{dc} - (V_{c0} - V_{dc})\,e^{-\alpha t} = V_{c0} \tag{4.12}$$

So the analytical expression for V_{c0} can be found:

$$V_{c0} = V_{dc}\frac{e^{-\alpha t}}{1 + e^{-\alpha t}} \tag{4.13}$$

Another thing to consider is that no deadtime and snubbers must be present, in fact the switch turn on is always a ZCS, because the current at the beginning of the period is always zero and starts to raise only when the transistor is fully conducting. On the other hand, the switch turn off is a ZVS, because after the conduction time, the current naturally flows through
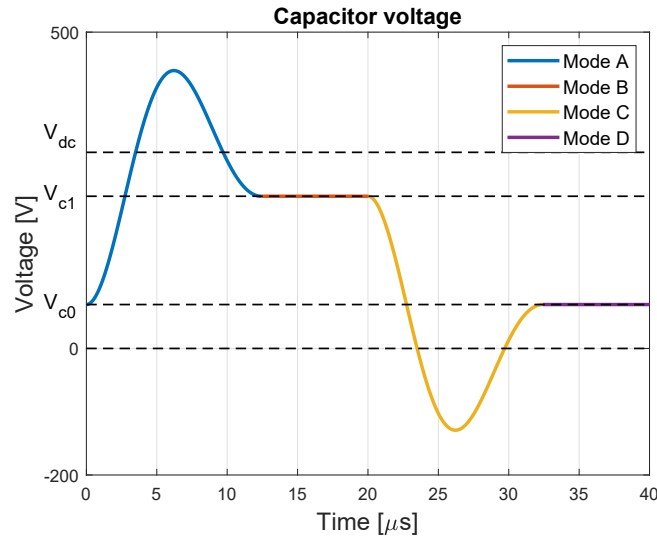
Figure 4.11: One period capacitor voltage waveform for a switching frequency of $f_s = 25\,kHz$

its antiparallel diode. So, with this power control strategy there is no need to protect the switch against the hard commutations.

Concerning the power inducted in the load, it's variation can be done adjusting the time periods when the inverter is switched off (Mode B and D), this means that the switching frequency can be varied from a maximum value that is $f_{s_{max}} = \frac{f_d}{2}$ to the aforementioned 20 kHz. The power control is then linear with the switching frequency (as can be seen in figure 4.12):

$$P = \alpha \, P_{max} \tag{4.14a}$$

$$\alpha = \frac{t_1}{t_2} = \frac{2\,f_s}{f_d} \tag{4.14b}$$

Where P_{max} the maximum power, i.e. when $f_s = \frac{f_d}{2}$.

Some literature about the DCM can be found in [23].

4.2   Novel control strategy proposed

4.2.1   Introduction

The control strategies explained and analysed in section 4.1, shows how many ways the power in the load can be supplied. In the most common induction hobs that are sold in the stores, as showed in figure 1.2, the power can be regulated by means of changing a number in the user interface that range from 10 (maximum power, around 3.3 kW) to 1 (minimum power, 50-100 W).

The most common strategy is to supply the medium/high power level with a SWM technique, and the lower power level with PDM control. The drawbacks of such technique is that the low power range is supplied discontinuosly and the user can experience some boiling pulses at low power. The aim of this section is to provide a power modulation strategy that allows to reach a power of about 50-100 W without using the PDM control.
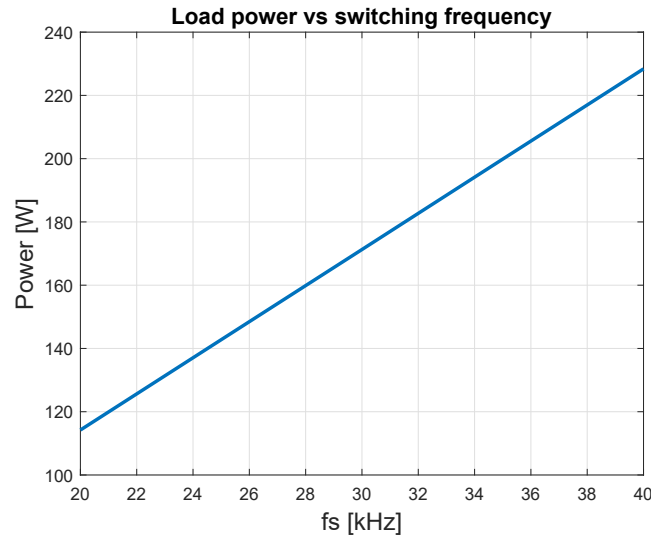
Figure 4.12: Load active power with different switching frequencies

To do this, both analytical and FEM simulations will be necessary, and an update of some parameters are needed and discussed in section 4.2.2. It will be taken into consideration that the load lumped model characterization is not constant with frequency and current, and the change in the values will be showed in section 4.2.3. Then in 4.2.4, 4.2.5 and 4.2.6 the results of the application of the different strategies will be shown.

4.2.2   Update of the materials parameters

The FEM simulation used in section 3.3 has still some simplifications, that will be relaxed in this section:

- The ferrite BH curve is considered linear with an infinite permeability.
- The resistivity of the pot is considered at 20°C.

From ferroxcube.com the magnetic characteristics of the ferrite can be found. Usually the type used for induction hobs is 3C90. The magnetic characteristics are considered at a temperature of 100°C:

$$\mu_i = 3750 \tag{4.15a}$$
$$B_{sat} = 0.38\,T \tag{4.15b}$$

The magnetization curve can be seen in figure 4.13.

The resistivity of the pot must be considered at a temperature higher than 20°C. From matweb.com the foolowing informations about the resistivity of the magnetic stainless steel AISI 409 are given:

$$\rho_{pot} = \begin{cases} 60 \cdot 10^{-8} & @\ T = 20°C \\ 76 \cdot 10^{-8} & @\ T = 20°C \end{cases} \tag{4.16}$$

considering a linear increase of the resistivity with the temperature:

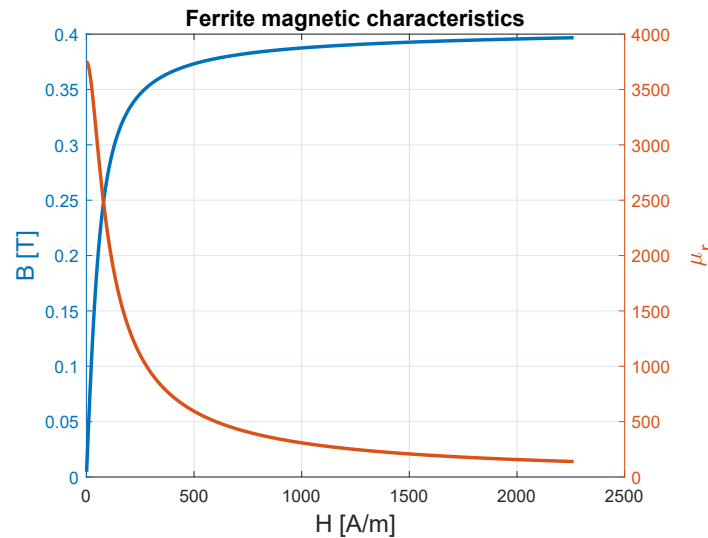$$\rho_{T_{pot}} = \rho_{20_{pot}}(1 + \alpha(T - 20)) \tag{4.17}$$

Figure 4.13: Magnetization curve for ferrite 3C90 at 100 °C

It holds that $\alpha = 1.48 \cdot 10^{-3}$. So the resistivity of the pot at 100 °C will be $\rho_{pot} = 67.1 \cdot 10^{-8}\Omega \cdot m$.

4.2.3 Load characterization

In this section, the variation of the equivalent parameters R_{eq} and L_{eq} with the current and the frequency will be showed and analysed. The geometry of the inductor and pot is displayed in table 4.3. This choice of dimensions allow the maximum power to be around 3.3 kW, see section 4.2.4 for the details.

Table 4.3: Parameters values for the first example

Parameter name	Value	Parameter name	Value
Inductor		Pot and ferrite layer	
R_i	21 mm	h	4.5 mm
R_e	90 mm	m	0.8 mm
N	23	s_{pot}	1 mm
h_c	3 mm	ρ_{pot}	$67.1 \cdot 10^{-8} \; \Omega \cdot m$
		μ_{pot}	see fig. 3.8
		μ_{ferr}	see fig. 4.13
		s_{ferr}	5 mm

Using the FEM model, the Z_{eq} for the load is calculated, for different values of supply current and frequency. At the end of the process a matrix similar to the one explained in figure 4.14 is obtained as a representation of the function $Z_{eq}(f_s, I_{rms})$.

	I_1	I_2	I_3	I_4	I_5	I_6
f_1	Z_{11}	Z_{12}	Z_{13}	Z_{14}	Z_{15}	Z_{16}
f_2	Z_{21}	Z_{22}	Z_{23}	Z_{24}	Z_{25}	Z_{26}
f_3	Z_{31}	Z_{32}	Z_{33}	Z_{34}	Z_{35}	Z_{36}
f_4	Z_{41}	Z_{42}	Z_{43}	Z_{44}	Z_{45}	Z_{46}

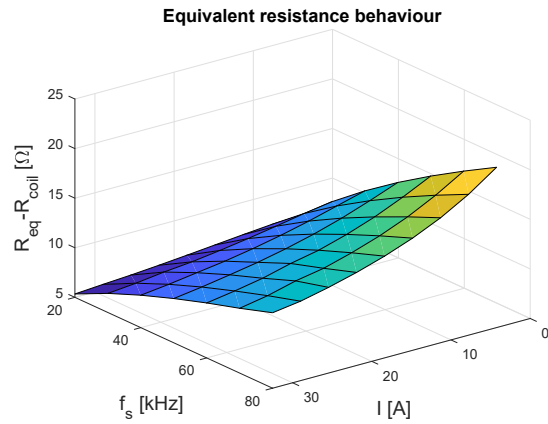Figure 4.14: Matrix with the calculated value of Z_{eq} from the FEM simulation

4.2.3.1 Equivalent resistance R_{eq}

The values of the equivalent resistance with different frequencies and rms current value of the supply for the geometry of table 4.3 can be seen in figure 4.15.
 Some things should be underlined about such behaviour:
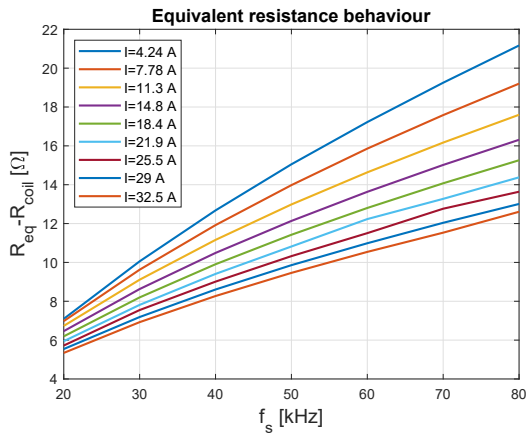
(a) 2D graph   (b) 3D surface

Figure 4.15: R_{eq} values for the geometry of table 4.3

- The resistance increase with the frequency: this is because the more the flux changes in time, the more the active power in the load.
- The resistance decrease with the current: this is due to the saturation effect, in fact when the current increase the permeability of the metal in the zone with current densities decrease, so less magnetic flux is generated due to an increase of the reluctance seen by the inductor.

4.2.3.2 Equivalent inductance L_eq

The values of the equivalent inductance with different frequencies and rms current value of the supply for the geometry of table 4.3 can be seen in figure 4.16.

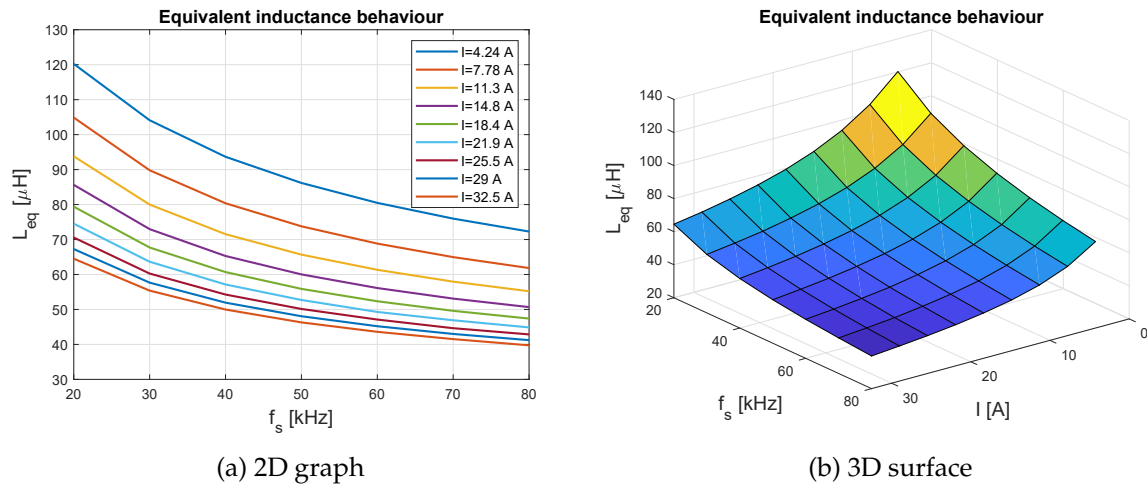(a) 2D graph   (b) 3D surface

Figure 4.16: L_{eq} values for the geometry of table 4.3

Some things should be underlined about such behaviour:

- The inductance decreases with the frequency: this because the more the frequency, the more the eddy current generated, and the more demagnetizing effect.
- The inductance decrease with the current: the saturation phenomena leads to a decrease of the magnetization effect due to the decrease of the relative permeability of the pot.

4.2.4 Square wave modulation (SWM)

For the medium/high power levels, the SWM technique is used. In addition to the description of the strategy made in section 4.1.1, the variations of the load are taken into account, so an iterative method is used to find the right working point of the system:

1. A starting value for Z_{eq} is chosen, the map of the load obtained from the FEM simulation is loaded into the Matlab workspace and the switching frequency is set to $f_{0_{start}} = 20kHz$.

2. If the switching frequency is still 20 kHz the resonant capacitor is set according to the formula:

$$C_r = \frac{1}{(2\,\pi\,f_{0_{start}})^2 L_{eq}} \tag{4.18}$$

3. The load waveforms are obtained analytically through Matlab or from a Simulink model. using the procedure explained in section 2.2.3.

4. Starting from the calculated rms current in the load and the switching frequency an equivalent impedance value for the load is interpolated from the $Z_{eq}(f_s, I_{rms})$ function.

5. Step number 2 is repeated if the conditions for its validity holds.

6. The procedure starts now again from step 3, but:

- If the difference of the module of Z_{eq} between the actual iteration and the previous is less than $0.1\,\Omega$, the power is calculated and the switching frequency is increased to the next step.
- If the stop conditon doesn't hold, the frequency is not changed.

7. The whole process ends when the frequency reach the upper value ($60\,kHz$ for example)

To make this procedure more easy to understand, the picture 4.17 can be helpful.
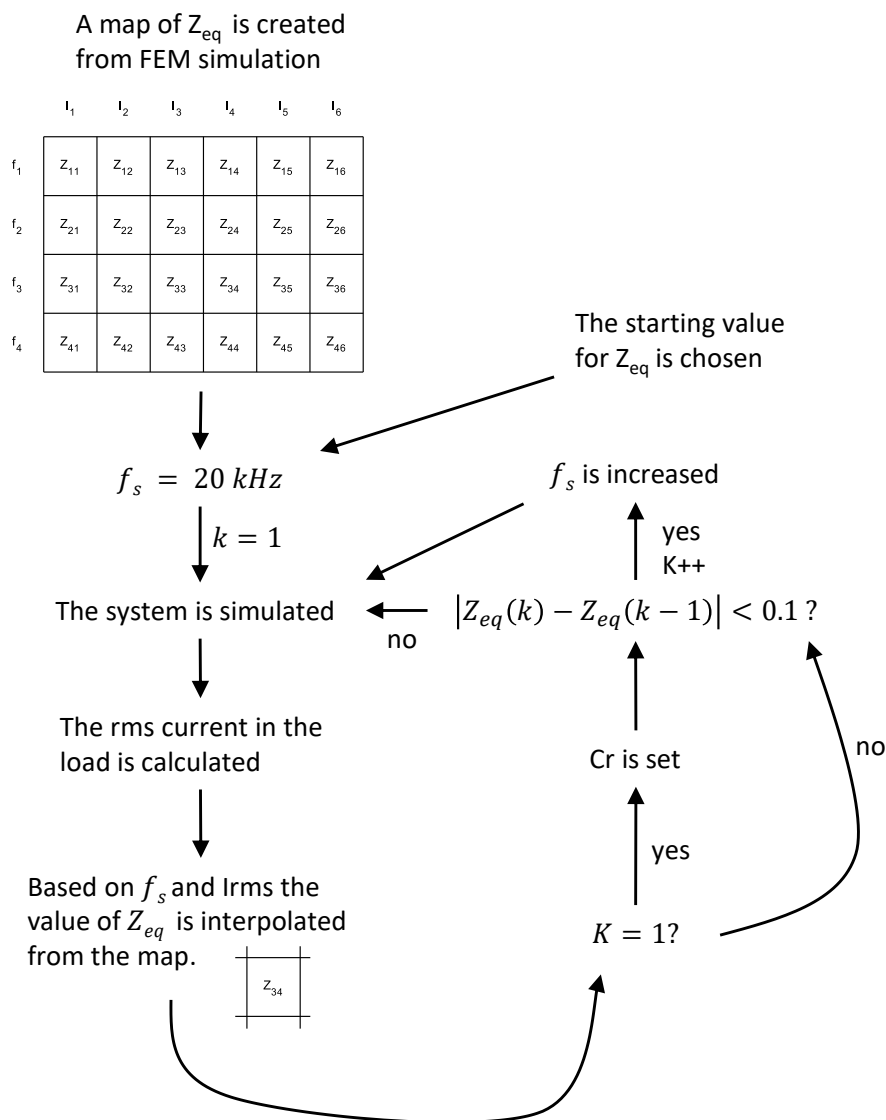

Figure 4.17: Iterative process used to find the active power in the load with the SWM technique

The load power results of the procedure explained are showed in figure 4.18. As can be seen, the peak power with this geometry is above 3 kW, as desired. The resonant capacitor value set in order to have the resonance frequency at 20 kHz is $C_r = 920.4\,nF$.
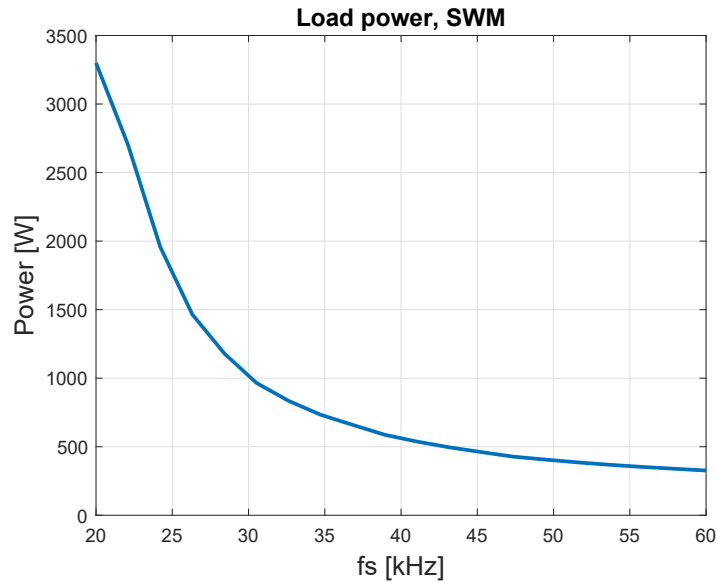
Figure 4.18: Results of the Iterative process used to find the active power in the load with the SWM technique

It is interesting to see how the equivalent parameters change during the simulation. In table 4.4 the values are showed. Since both the increase of the frequency and the decrease of the current lead to an increase of the resistance, it has a remarkable increment from $5.8\,\Omega$ to $17.2\,\Omega$. Regarding the inductance, there isn't any evident change of the values, because of the opposite effects that the increase of the frequency and decrease of the current have on the L_{eq} value.

Table 4.4: Equivalent impedance value in the SWM implemented

f_s [kHz]	I_{rms} [A]	R_{eq} [Ω]	L_{eq} [μH]
20	23.8	5.81	72.1
24	16.9	7.10	75.4
28	12.0	8.53	80.3
32	9.35	9.82	83.0
36	7.88	11.0	83.2
40	6.80	12.1	83.8
44	6.03	13.2	83.6
48	5.42	14.2	83.2
52	5.01	15.2	82.1
56	4.66	16.2	81.1
60	4.36	17.2	80.0

4.2.5   Discontinuous current mode (DCM)

Since in the discontinuous current mode the waweforms are not sinusoidal, the method used for the SWM strategy cannot be applied, because the values for the load R_{eq}, L_{eq}, C_r have been found for the sinusoidal regime. A transient FEM model has been made in order to obtain the

current waweforms. The description of how the strategy works have been explained in section 4.1.4. To make the transient simulation, the circuit have been modified as can be seen in figure 4.19a: a voltage source have been used with imposed voltage as shown in figure 4.19b:

$$V_{source}(t) = V_{dc} \, sign(sin(2\pi f_s t)) \tag{4.19}$$

The simulation have been set up with the aim to find the right self-oscillation pattern of the load. During the first half of the period, when the current is different from zero ($0 < t < t_1$ in figure 4.9a) the top switch is open, so the total load of the inverter $R_{eq} - L_{eq} - C_r$ has an applied voltage of V_{dc}. During the second half of the period, when the load is supplied, the voltage is $-V_{dc}$.
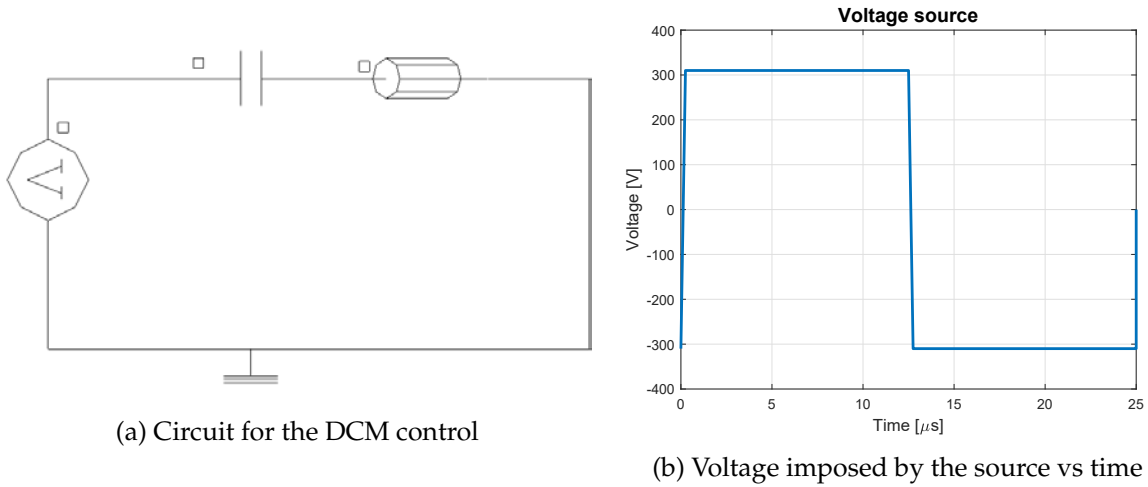

(a) Circuit for the DCM control

(b) Voltage imposed by the source vs time

Figure 4.19: FEM modifications for transient simulation

It is worth to remember that since $f_{s_{max}} = \frac{f_d}{2}$ and $f_{s_{min}} = 20 \, kHz$, the C_r value have been chosen in such a way to obtain a minimum power (correspondent to $f_{s_{min}}$) that is around 50 W. The FEM model gives the results for $f_{s_{max}}$ which correspond also to the maximum power in DCM. In table 4.5 a recap of the different results obtained with different chosen oscillation frequency can be seen.

Table 4.5: Results from FEM simulations

f_d [kHz]	$f_{s_{max}}$ [kHz]	C_r [nF]	P_{max} [W]	P_{min} [W]
100	50	22	75	30
80	40	38	99	49
60	30	59	116	78

From the table above, it can be concluded that the best scenario is the one with $f_d = 80 \, kHz$, in fact the minimum power is close to 50 W as requested. The maximum power is calculated from the waweform obtained with the transient simulation (equation 4.20) while the power for lower switching frequencies $f_s < f_{s_{max}}$ can be obtained with the equation 4.14.

$$P_{max} = mean(v_{coil}(t) \, i_{coil}(t)) \tag{4.20}$$

Some waweforms for this scenario can be seen in figures 4.20 and 4.21a. The Power values for the switching frequency from 20 kHz to $\frac{f_d}{2} = 40kHz$ is howed in figure 4.21b
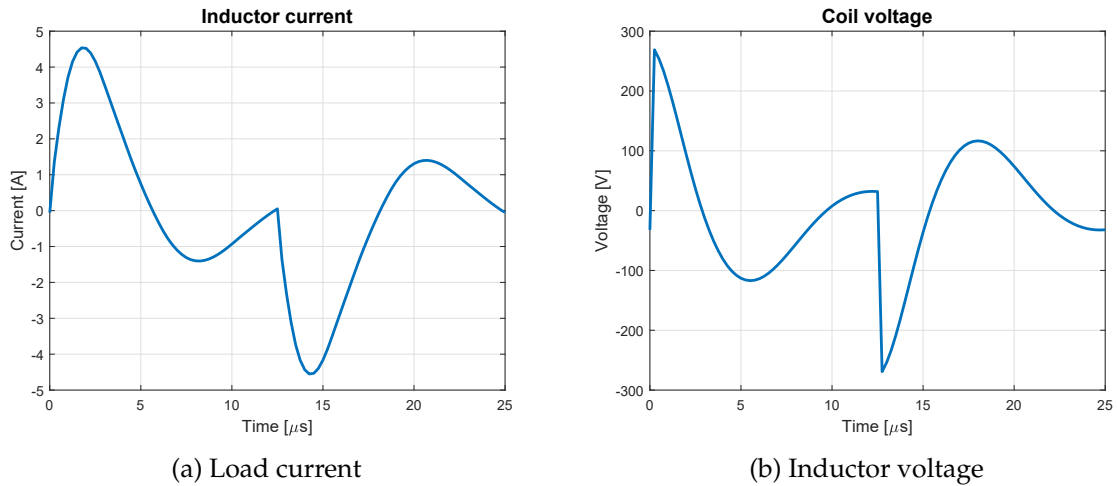

(a) Load current

(b) Inductor voltage

Figure 4.20: One period waveforms in the load for a switching frequency of $f_s = \frac{f_d}{2} = 40\,kHz$

(a) One period load current waveform for a switching frequency of $f_s = 20\,kHz$
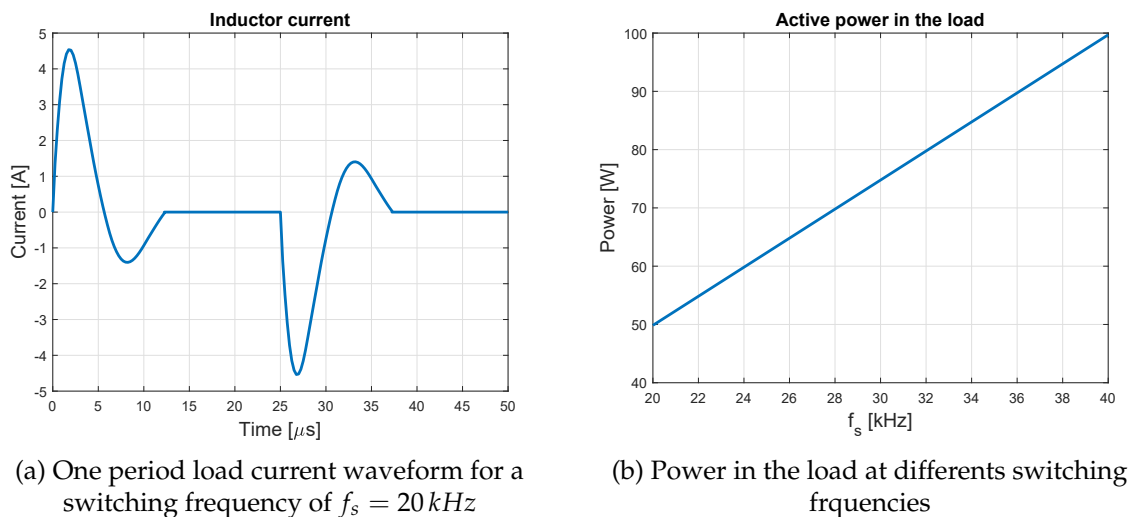
(b) Power in the load at differents switching frquencies

Figure 4.21: One period waveform in the load and overview of the power values in the load for different switching frequencies

4.2.6 Asymmetrical duty cycle control (ADC)

The power levels in the pot achievable with the SWM and DCM techniques designed so far are visible in figures 4.18 and 4.21b. The power range for the SWM is 3300-330 W, while for ADC is 100-50 W. To have a more uniform power distribution in the range 3300-50 W, the ADC technique is used in order to find a load power point in the empty range 330-100 W. The description of how the ADC technique works is provided in section 4.1.2. The final result obtained, after some test, is a power of 210 W with a switching frequency of 60 kHz and a duty cycle of 25%. The resonant capacitor value C_r is 920.4 nF as in the SWM, while the deadtime is $t_{dt} = 2\mu s$. The simulation of such working point have been done with a transient FEM simulation, because since the duty cycle is not 50%, the regime cannot be assimilated to a sinusoidal one any more.

The circuit used in the FEM simulation is the same as the one in figure 4.19a but with different waveform for the voltage source, which is showed in figure 4.22a. The power in the load is calculated as in the DCM using equation 4.20.
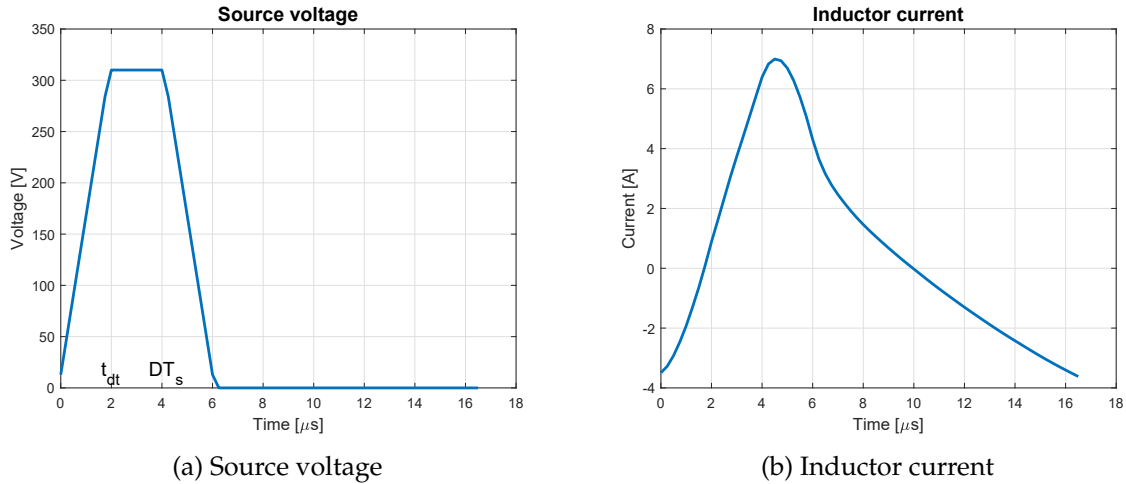

(a) Source voltage

(b) Inductor current

Figure 4.22: One period waveforms for the simulated ADC with $f_s = 60\,kHz$ and $D = 25\,\%$

4.2.7 Conclusions

The aim of section 4.2 was to provide a design of a control configurations that can vary the power from 3300 to 50 W. The combination of different techniques have been used and a recap of the main results and parameters involved in the control is listed in table 4.6.

Table 4.6: Resume of the strategy combinations

Power range [W]	f_s [kHz]	C_r [nF]	C_s [nF]	t_{dt} [μs]
3300-350	20-60	920.4	10	1.1
200	60	920.4	10	2
100-50	40-20	38	/	/

A possible load power level configuration, achievable with the user interface where can be selected a number from 10 (max power) to 1 (min power), is shown in figure 4.23. The absolute values are not fixed and they can be adjusted.

The main big advantages of this kind of control technique are

- the PDM strategy is completely avoided, so the power is not sent to the load discontinuously anymore.
- in the low power range the switching frequency is relatively low. In fact, while a PDM strategy require a switching frequency of 50-60 kHz, in the proposed discontinuous current mode the frequency is 20-40 kHz. This means that the switching losses are reduced.

On the other hand, some drawbacks are:

- the load must be connected to two resonant capacitors that are connected separately: the 920 pF one from level 3 to 10, the other one (38 nF) for levels 1 and 2. Both capacitors can
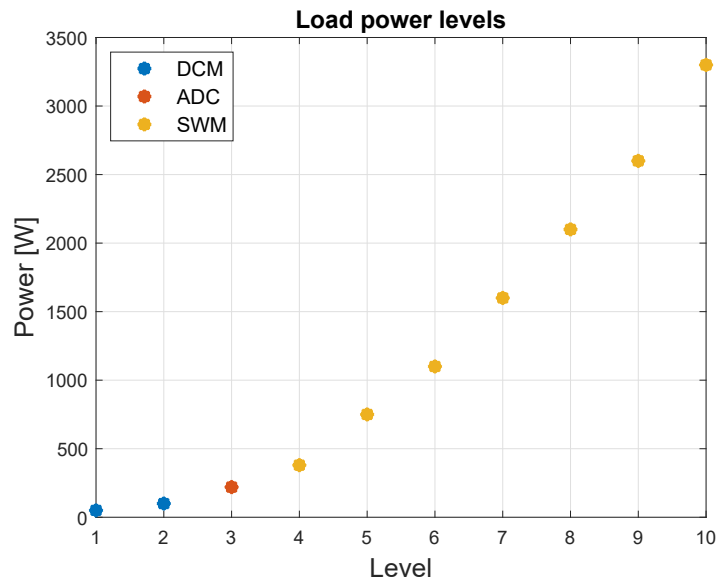
Figure 4.23: Expected load power levels with the control strategy proposed in this chapter

be inserted by a switch of a relè. In picture 4.24a a possible solution is showed, bu only as a concept. Some discharging resistance may be needed to avoid residual high voltages.

- Also the snubber capacitance needs to be disconnected, since in the discontinuous current mode it is not used. A possible solution with a series relè switch is showed in figure 4.24b.
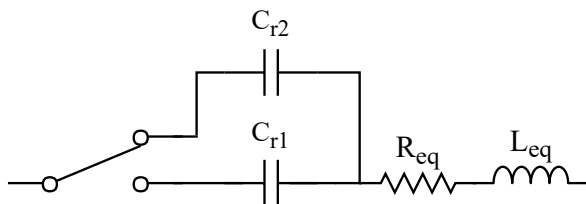
(a) Change of the resonant capacitor
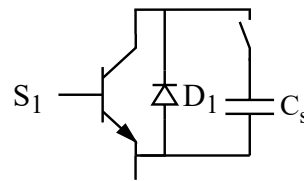
(b) Possible way to connect the snubber capacitor

Figure 4.24: Possible solutions to manage the capacitor connections in the inverter and in the load

It can be concluded that an induction hob equipped with such control technique is a bit more expensive than traditional methods, because of the increase of the microcontroller code complexity and due to an additional resonant capacitor required, but this increase of cost lead to a high improvement on the load power supply quality.

Chapter 5

Smart pot for induction cooking

The university of Padua, through the electroheat laboratory and professor Dughiero has a patent registered on 27/07/2016 [24]. This innovative concept of pot includes several features that can change the cooking experience:

- Thermal insulation of the wall of the pot: the conduction losses are extremely reduced (no risk of burning touching the outer surface of the pan);
- The possibility to supply wirelessly some devices such as a mixer or a vacuum pump by means of a coil placed at the bottom of the pot;

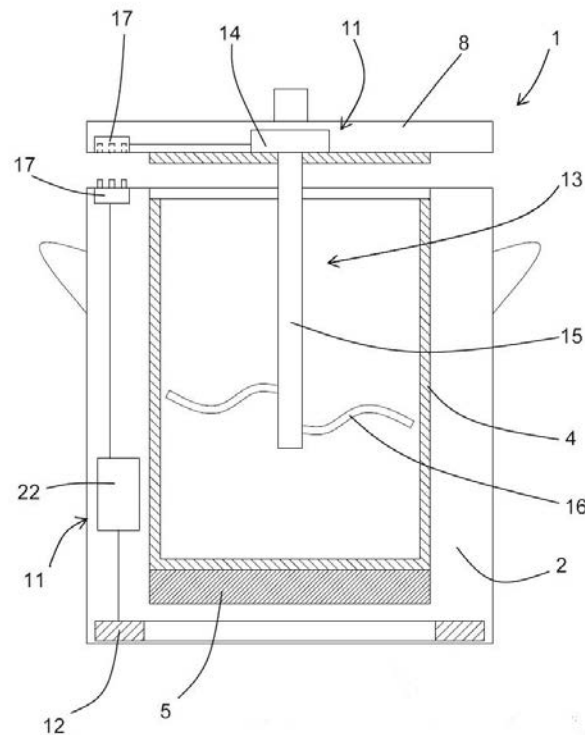An overview of a possible realization of such pot can be seen in figure 5.1.

Figure 5.1: Overview of a possible pot configuration

The following elements are highlighted in the picture:

- 1: Pot under consideration
- 2: Outer containment body
- 4: Metallic container
- 5: Ferromagnetic active portion
- 8: Lid
- 11: Auxiliary device
- 12: Receiving coil
- 13: Mixer
- 14: Electric motor
- 15: Shaft
- 16: Mixing blades
- 17: Electric contacts
- 22: Programmable control unit

In the following sections, a possible practical realization of this system will be analyzed, a circuital model will be built and validated by means of circuital and FEM comparison. Then a possible practical implementation of an electronic converter supplying a device will be explained.

5.1   Circuital model of the system

In the electroheat laboratory a concept of such innovative pot has already been built and it can be seen in figure 5.2.

<div align="center">(a) Lateral view   (b) Bottom view without the wood layer</div>
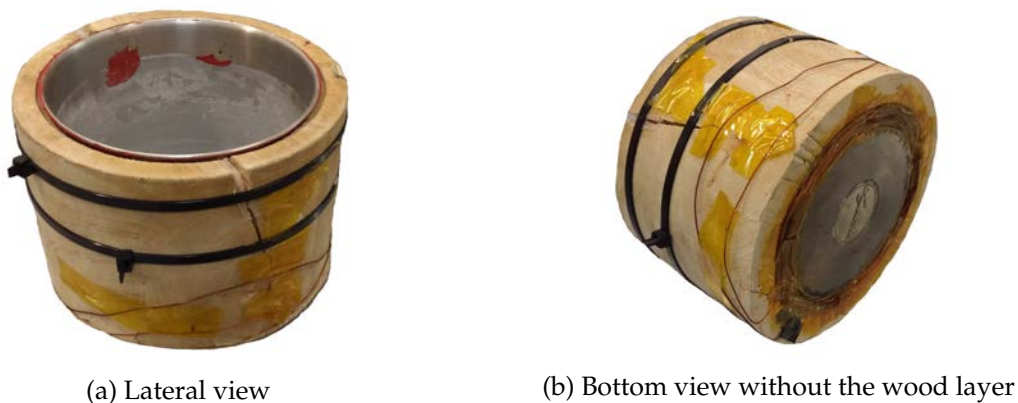
<div align="center">Figure 5.2: Views of the pot prototype present in the laboratory</div>

As it can be understood, this prototype keeps some features already explained in the introduction of the chapter, with some differences compared to the general model in figure 5.1. In particular, the coil is wounded at the same height of the ferromagnetic bottom of the pot, and this is the characteristic that is important to take into account. Later on some explanations on how the reciprocal position between the pot and the coil affects the energy transfer will be given.

To model the system composed by the inductor in the hob and the pan together with the coil a procedure similar to the one used for a wireless transfer system (or a transformer) will be used.

For a general wireless transfer system (air-cored transformer) one of the possible circuit model is provided in [17] and can be seen in figure 5.3.
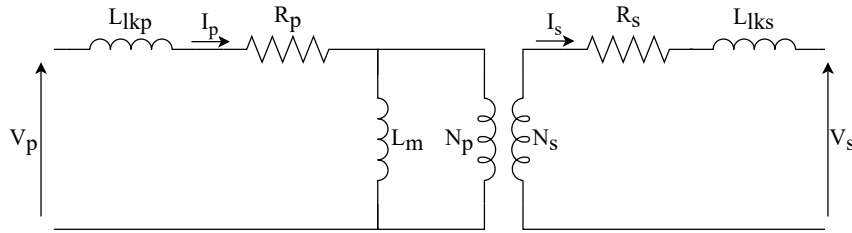

Figure 5.3: T-model of the electrical equivalent circuit

The meanings of the different elements used in the equivalent circuit are listed in table 5.1. Subscript p stay for primary, while subscript s stay for secondary.

Table 5.1: meanings of the different lumped elements used in the equivalent circuits.

Element	U. M.	Meaning
N	[-]	Number of turns.
R	$[\Omega]$	AC resistance of the coil.
L	[H]	Self-inductance of the coil.
L_{lk}	[H]	Leakage inductance of the coil.
M	[H]	Mutual inductance between the coils.
L_m	[H]	Magnetizing inductance.

The leakage and magnetizing inductance are calculated with the followings formulas [17]:

$$a = \frac{N_p}{N_s} \tag{5.1a}$$

$$L_m = a\,M \tag{5.1b}$$

$$L_{lk_p} = L_p - L_m \tag{5.1c}$$

$$L_{lk_s} = L_s - \frac{M}{a} = L_s - \frac{L_m}{a^2} \tag{5.1d}$$

The main difference between a general wireless transfer system and the inductor-pot system is the additional presence of the magnetic bottom of the pot. In fact, the air-cored transformer has no losses in magnetic materials, but only joule losses in the windings. On the other hand, the losses in the system under consideration due to eddy currents are the most considerable part of the total power transferred by the inductor in the hob, so the equivalent circuit must take this into account. In addition, the current in the pot heavily influences the value of the circuit parameters, depending on the power level chosen from the user interface in the hob.

The equivalent circuit that will be proposed, as well as the one already presented, is valid only in sinusoidal regime. With an half bridge inverter feeding the inductor, the only quantity that can be approximated to a sinusoid is the current, so the circuit will be excited with a sinusoidal current source.

The final version of the circuit representing the system can be seen in figure 5.4, which includes also the equivalent resistance of the pot in series with the current generator I_p:

$$\Delta R = R_{eq} - R_p = \frac{P_{pot}}{I_p^2} \tag{5.2}$$

Also the resonant capacitor C_r that is connected in series with the inductor have been included in the circuit, as well as a secondary capacitance C_s that might be needed in order to improve the power transfer.
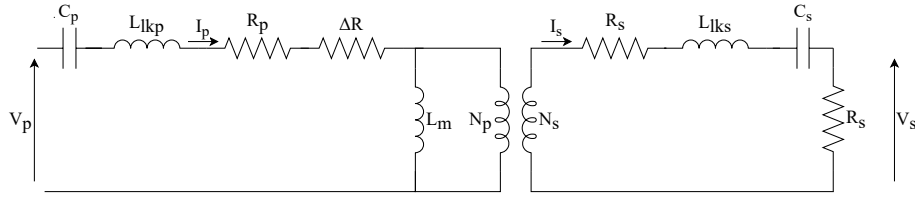

Figure 5.4: T-model of the electrical equivalent circuit for the inductor and the smart-pot

In Matlab a circuital solution of the above circuit has been implemented by means of a function that requires the geometrical parameters as inputs and gives the voltages and currents in the circuit as outputs:

$$\dot{Z}_p = R_{eq} + j\omega L_{lkp} - j\frac{1}{\omega C_p} \tag{5.3}$$

$$\dot{Z}_m = j\omega M \tag{5.4}$$

$$\dot{Z}_s = R_s + j\omega L_{lks} - j\frac{1}{\omega C_s} \tag{5.5}$$

$$\overline{V_p} = \overline{I_p}\left(\dot{Z}_p + \frac{\dot{Z}_m(\dot{Z}_s + R_l)a^2}{\dot{Z}_m + (\dot{Z}_s + R_l)a^2}\right) \tag{5.6}$$

$$\overline{I_m} = \overline{I_p}\frac{(\dot{Z}_s + R_l)a^2}{\dot{Z}_m + (\dot{Z}_s + R_l)a^2} \tag{5.7}$$

$$\overline{I_s} = (\overline{I_p} - \overline{I_m})a \tag{5.8}$$

$$\overline{V_s} = R_l\overline{I_s} \tag{5.9}$$

$$P_{out} = R_l I_s^2 \tag{5.10}$$

It must be underlined that the inductances L_{lkp}, L_{lks}, M and the resistance ΔR are strongly influenced by the saturation level of the pot which, in turns, depends on the frequency and amplitude of the current flowing into the inductor. The parameters $R_{eq}(f, I_p)$ and $L_{eq}(f, I_p)$ are mapped as already showed in section 4.2.3, with no load connected at the receiving coil. The mutual inductance $M(f, I_p)$ and the secondary self inductance $L_s(f, I_s)$ are also found for different values of frequency and current according to the following relations:

$$V_s = j\omega\, M(f, I)\, I_p \text{ when } I_s = 0 \tag{5.11a}$$

$$\Phi_s = L_s\, I_s \qquad\qquad \text{when } I_p = 0 \tag{5.11b}$$

To map the parameters discussed above, a FEM model that include the coil wound around the bottom of the pot have been built. An overview of the geometry and the circuit can be seen in figure 5.5 (the new receiving coil is yellow) while the geometrical parameters value are listed in table 5.3. The motivation for those values will be given at the end of the chapter, after the sizing of the conductors. The dimensions of the inductor are one of the most common that can be found in the majority of induction cooktops.

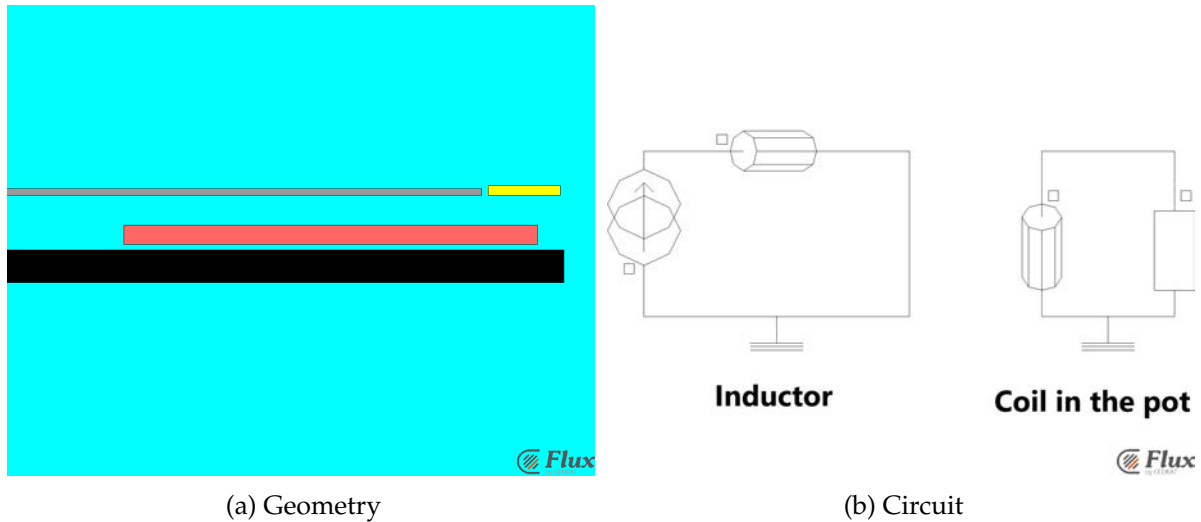(a) Geometry   (b) Circuit

Figure 5.5: Overview of the flux model for the smart pot

The additional geometrical parameters defined in this model are listed in table 5.2.

Table 5.2: Geometric parameters for the receiving coil

Parameter name	Description
R_{i_c}	Inner radius of the coil
w_c	Width of the coil
s_c	Thickness of the coil
N_s	Number of turns

L_s and M are found by means of equations 5.11 for different values of rms current value, switching frequency and number of turns of the secondary coil. The results can be seen in figure 5.6.

As it might be easy to guess, the less N_s is, the less is the value for the two inductances. L_s shows very little changing with current and frequency, and this is due to the fact that the current for which the inductance have been evaluated is not sufficient to reach the saturation zone of the material in the pot, so the relative permeability is almost constant for all the currents (from 0.1 to 4 A, rms values).

5.2   Validation of the model

In this section, the results from the circuital analysis will be compared to the ones obtained with the FEM simulation, analysing the differences. The results for different frequencies, primary

Table 5.3: Parameters values for the smart pot FEM simulation

Parameter name	Value	Parameter name	Value
Inductor		Pot and ferrite layer	
R_i	18 mm	h	4.5 mm
R_e	81 mm	m	0.8 mm
N	21	s_{pot}	1 mm
h_c	3 mm	ρ_{pot}	$67.1 \cdot 10^{-8} \ \Omega \cdot m$
Secondary coil		μ_{pot}	see fig. 3.8
R_{i_c}	$R_{pot} + 1$ mm	μ_{ferr}	see fig. 4.13
w_c	11 mm	s_{ferr}	5 mm
s_c	1.5 mm	R_{pot}	72.5 mm
N_s	$to\ be\ defined$ mm		

(a) Self inductance of the receiving coil

(b) Mutual inductance between inductor and receiving coil
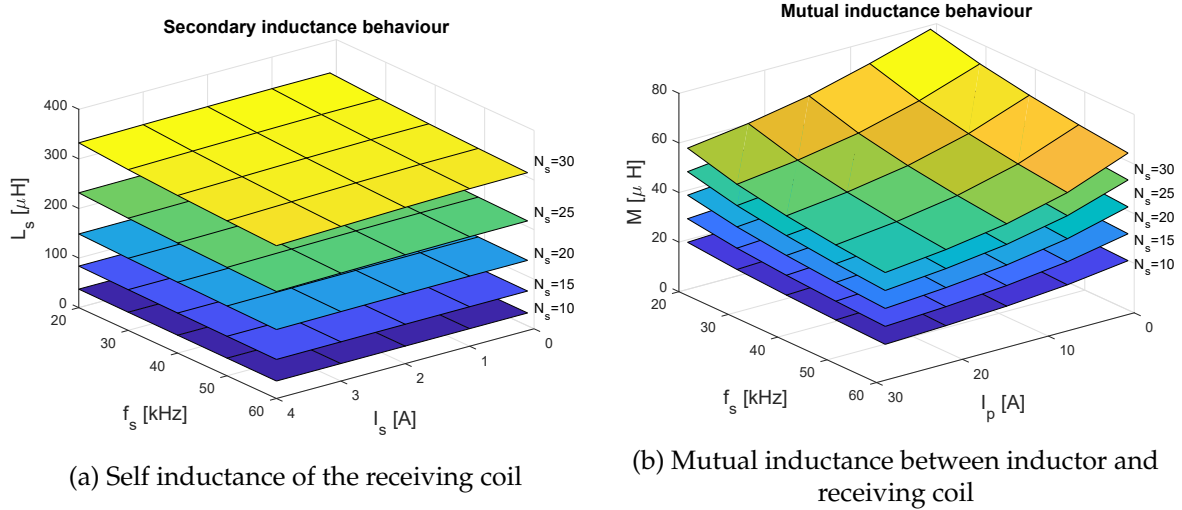
Figure 5.6: Map of the secondary self inductance and mutual inductance at different switching frequencies, current and number of secondary turns.

current and number of turns is showed in figures 5.7, 5.8, 5.9. No secondary capacitance C_s is considered.

As already done and explained several times in this thesis, the Matlab procedure that simulates the system, makes an interpolation on the mapped parameter R_{eq}, L_{eq}, M based on the frequency and the primary current. A starting value for L_s is chosen, and then an iterative process starts in order to find the correct value based on the effective current that flows in the secondary coil.

Some considerations and conclusions can be made looking at the results:

- No load conditions: the circuital solution gives exactly the same results as the FEM one (figures 5.8a, 5.7a, 5.9a).

- Load condition: the analytical results slightly deviates from the FEM ones when the primary current increases, so when the power transferred to R_l starts becoming not negligible compared to the power in the bottom of the pot. On the other hand, very good agreement are showed fro lower primary currents (figures 5.7a, 5.8b, 5.9b).
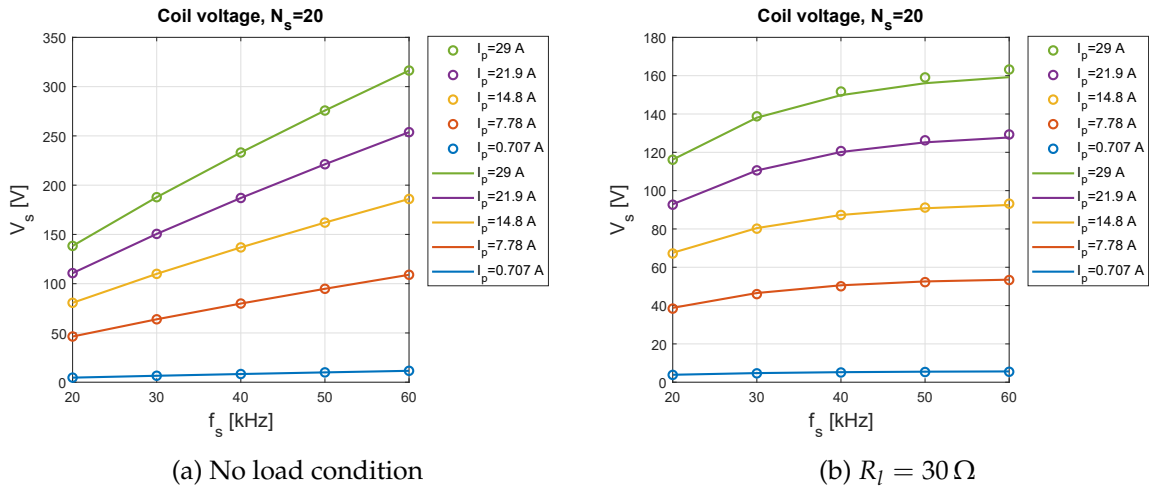
(a) No load condition

(b) $R_l = 30\,\Omega$

Figure 5.7: FEM (circles) and analytical (solid lines) comparison of the secondary voltage value with load and no-load conditions, with a fixed number of secondary turns $N_s = 20$

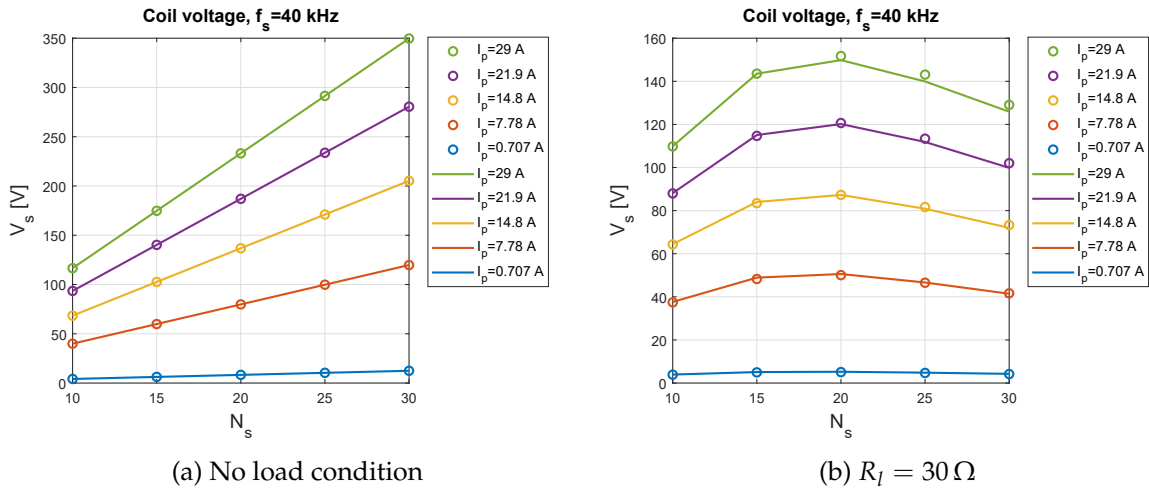(a) No load condition

(b) $R_l = 30\,\Omega$

Figure 5.8: FEM (circles) and analytical (solid lines) comparison of the secondary voltage value with load and no-load conditions, with a fixed switching frequency $f_s = 40\,kHz$

- The more I_p, the more is V_s, both with load and no load conditions.
- The no load voltage strongly increase with the number of turns N_s, while this is not true under load conditions, where it present a maximum value. In fact, when N_s increases, also L_s and R_s increases, (the voltage drop is high), so the optimum between low voltage drops and high no-load voltage stays "in between", for a precise value of N_s.
- As it can be seen in figure 5.9b, when $N_s = 30$, the load voltage doesn't depend on the frequency. This can be understood looking at the formula:

$$\overline{V_s} = \frac{j\omega M \overline{I_m}}{a} - \overline{I_s}(R_s + j\omega L_s) \tag{5.12}$$

The change of frequency affects the value of L_s, R_s and ω. In particular when $N_s = 30$, as can be seen in figure 5.6b, M decreases with the frequency while ω increases, so this opposite effects lead to a $\overline{V_s}$ which is not changing considerably with the frequency when $\overline{I_p}$ is fixed.
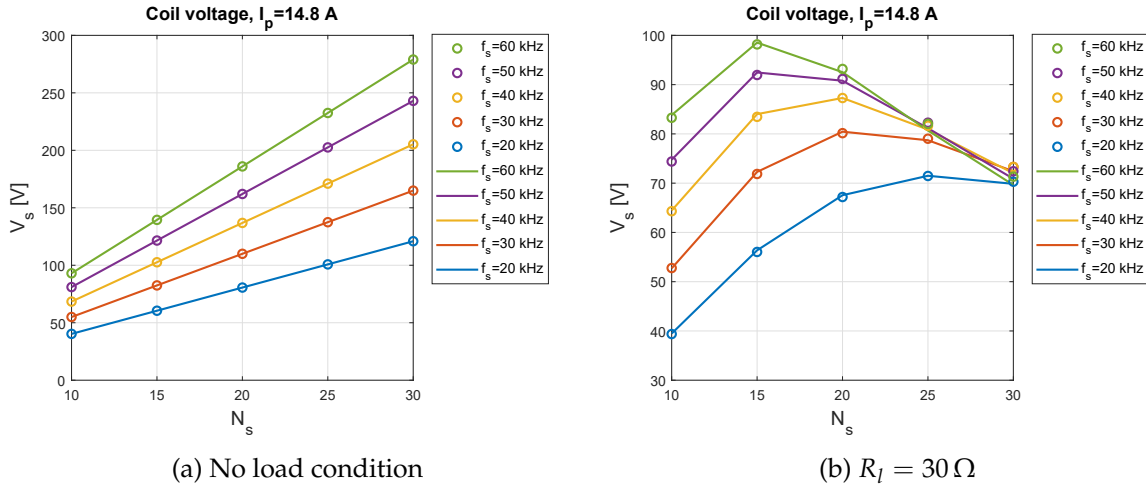
(a) No load condition

(b) $R_l = 30\,\Omega$

Figure 5.9: FEM (circles) and analytical (solid lines) comparison of the secondary voltage value with load and no-load conditions, with a fixed primary current $I_p = 14\,A$

It can be said, finally, that the model has been validated and the smart pot together with the inductor is accurately modelled, as can be seen in figures 5.7, 5.8, 5.9: results from FEM and circuital simulations shows very good agreement.

5.3 Design constraints

To proceed in order to size the secondary coil, some design specifications must be defined. The aim of the secondary coil that have been decided is to supply a vacuum pump and a battery that are directly installed in the pot. The latter is needed in order to provide the energy to the pump when the cooktop is supplying the power with the PDM strategy. After a research done on the web, several pumps have been found, one in particular have been found in [25] and the electrical specifications are:

- Supply voltage: $12\,V_{DC}$
- Absorbed current $\approx 0.6A$

So a maximum power of 10 W can be taken into account. Regarding the battery, a $12\,V_{DC}$, 3000 mAh Li-ion model is a quite common size, as can be found in [26], with sufficient charge. The maximum charging current is 2 A which means $\approx 25W$. Taking into account other auxiliary devices or converters, the power for which the secondary coil will be designed is 30 W - $12\,V_{DC}$. In figure 5.10 an example of vacuum pump and battery can be seen. A resistance of value $R_l = 12/2 = 6\,\Omega$ will be used to model the load.

5.4 Considerations about the secondary capacitance

As can be seen in figure 5.4, a secondary capacitor can be put in series with the secondary coil in order to enhance the transfer capabilities of the system. In fact, the voltage drop across the secondary impedance $R_s + j\omega L_s - j\frac{1}{\omega C_s}$ can be modified and reduced if C_s is tuned correctly.

Firstly, the value of the primary resonant capacitor C_r have been set in order to obtain a peak value of the induced power in the pot (without secondary coil) that is around 2000-2500 W, that

(a) Vacuum pump   (b) Battery

Figure 5.10: Examples of devices that can be supplied by the secondary coil

is a typical maximum power level reached by common induction cooktops for each inductor, with SWM strategy.

The value of C_r have been set without taking into consideration the presence of a load in the secondary coil. This because the power absorbed ($\approx 30\,W$) is negligible compared to the power dissipated in the pan: the equivalent impedance seen by the inverter doesn't change significantly. To calculate the power the same procedure already explained in figure 4.17 has been used.

The capacitor value that allows this is $C_r = 2.7\,\mu F$, and the resulting power in the pot (SWM) can be seen in figure 5.11a together with the rms current I_p in the inductor.

(a) Power induced in the pot   (b) Rms current in the inductor

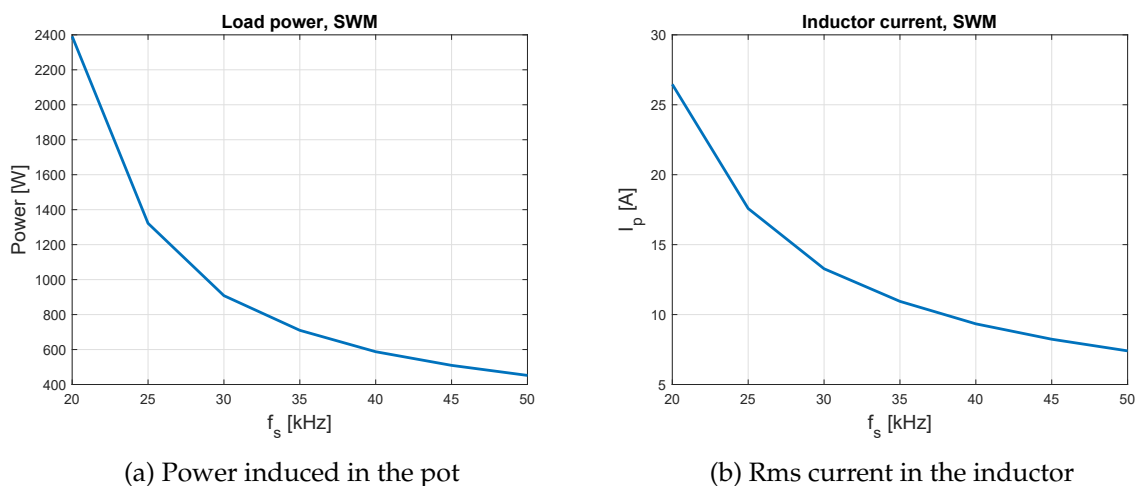Figure 5.11: Power and current in the pot with no-load connected to the secondary coil

So, the values that will be used for I_p depending on f_s, from now on, are resumed in table 5.4. Those values are also the rms value for the current generator that is put (depending on the switching frequency) in the primary side of the circuit.

The secondary voltage V_s with no-load condition and supplied as in table 5.4 is showed in figure 5.12.

As it can be seen, the voltage reach values that are well above 100 V which is very high, considering that the required one is $12\,V_{DC}$. On the other hand, if the voltage is higher than the

Table 5.4: I_p for different f_s values

f_s [kHz]	I_p [A]
20	26.46
25	17.58
30	13.27
35	10.94
40	9.34
45	8.24
50	7.40
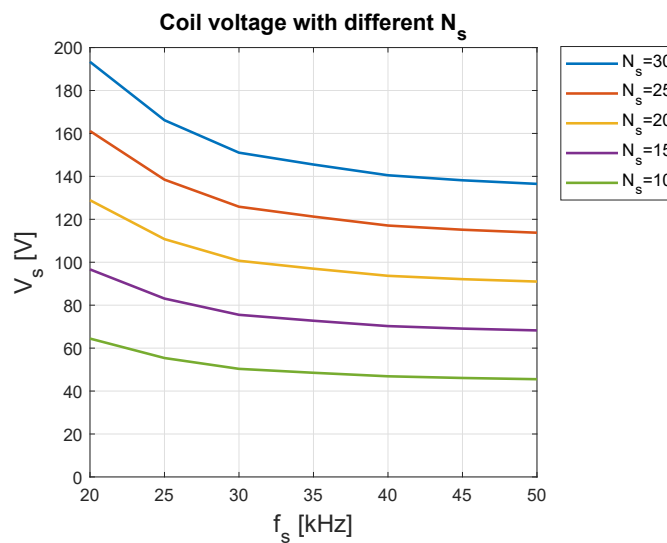
Figure 5.12: Secondary voltage with SWM, $R_l = +\infty$ and different number of turns N_s

required one, the current needed will be lower, and this means that the wire in the pot can be thinner.

In figure 5.13, two examples of output voltage for different values of C_s are showed. The peaks occur when the capacitor resonate with L_s. Obviously, it would be beneficial to change the value of C_s continuously accordingly to f_s, in order to maintain the resonance and have higher transfer capabilities through a big range of power levels, but it would be too expensive in terms of costs and space.

On the other hand, if the secondary current is very low, (due to high secondary voltage or due to low load) the voltage drop across L_s is negligible, so it is useless to put C_s: the load values don't change with different values of C_s. For this first design case, since the target is to supply 30 W, $N_s = 10$ turns will be considered and no secondary capacitance will be placed.
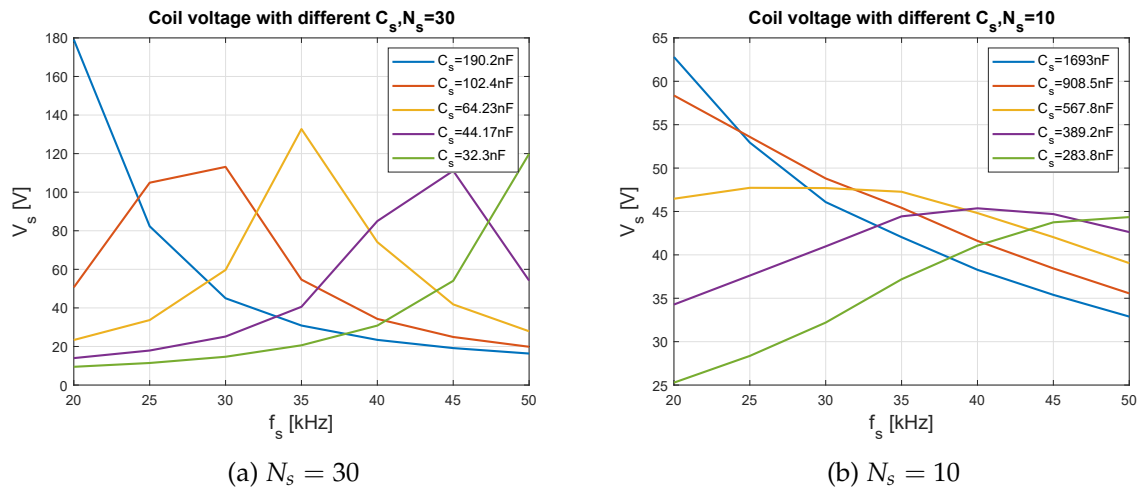
(a) $N_s = 30$ (b) $N_s = 10$

Figure 5.13: Secondary voltage for different secondary capacitors values, $R_l = 10\,\Omega$

5.5 Power conversion

5.5.1 System description

In order to correctly supply the load with a continuous voltage some converters must be used to convert the high frequency voltage to a continuous one. To design this system, Simulink have been used. Firstly the pot model have been built and verified through a comparison with the results from Matlab, where the analytical formulas from 5.3 to 5.10 have been implemented. The Simulink model can be seen in figure 5.14.
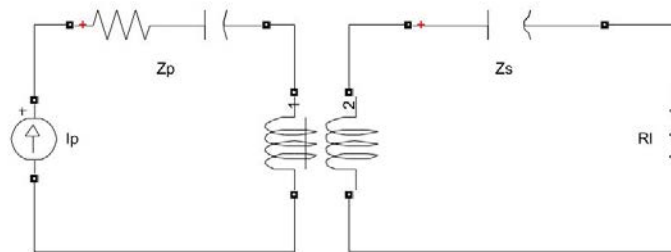

Figure 5.14: Simulink model for the inductor-smart pot system

The overview of the architecture of the power conversion system that will be used is shown in figure 5.15. It includes:

- A rectifier that supply a DC bus.
- A controlled buck converter that act as a stabiliser. A PID controller acts in order to mantain a constant voltage of 13 V across the load.

The correspondent simulink model used in order to simulate the system and find the correct configuration is shown in figure 5.16.

The capacitor C_{bus} have been chosen in order to have a stable voltage and accordingly to what is most used in practice. Often is used a $470\mu F$ electrolytic capacitor.
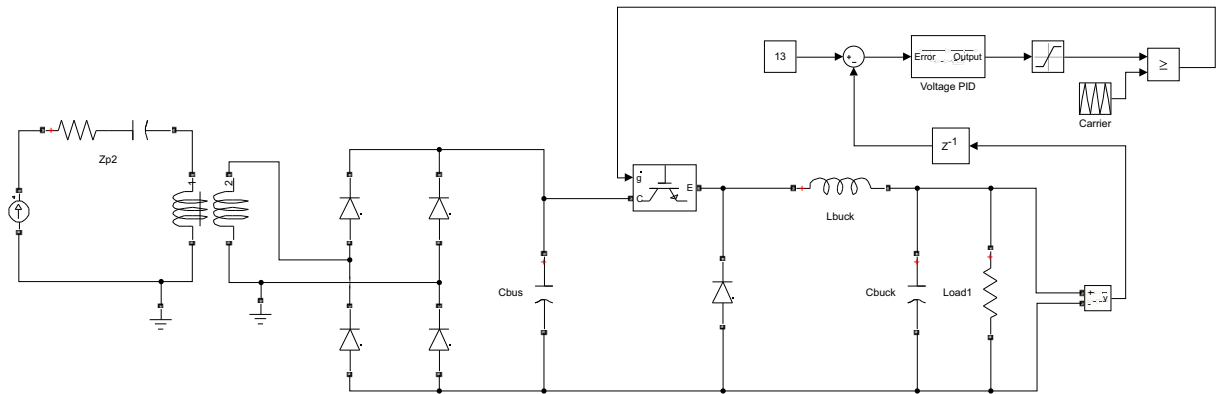
Figure 5.16: Overview of the smart-pot power conversion system modelled in Simulink

5.5.2   Design of the buck converter

The design of the buck converter includes the definition of the components (L_{buck} and C_{buck}) value and the tuning of the control parameters of the PID controller. Some preliminary assumptions must be done. The stabilizers that can be bought from the most common supplier, have a switching frequency that can be above 100 kHz. In this buck converter the switching frequency will be set to 20 kHz, in order to make simulation faster. The more interesting aspects of the results are the mean values of the DC bus and load voltage, which are not affected by the switching frequency value of the buck converter.

The inductor value have been chosen in order to achieve a continuous conduction mode with a certain maximum amount of ripple in the current [27]:

$$L_{buck} = \frac{(V_{in} - V_{out})V_{out}}{V_{in} f_s \Delta I_L} \tag{5.13}$$

where V_{in} is the DC bus voltage, V_{out} is the output voltage, f_s the switching frequency, ΔI_L the peak to peak current ripple. With $V_{in} = 50\,V$, $V_{out} = 13\,V$, $f_s = 20\,kHz$, $\Delta I_L = 0.1\,A$ the inductor values is $L_{buck} = 4.81\,\mu H$.
L_{buck} together with the capacitor C_{buck} form a second-order RC filter, with a cutoff frequency of:

$$f_{cutoff} = \frac{1}{2\pi\sqrt{L_{buck}C_{radd}}} \tag{5.14}$$

To supply the load with a very low ripple (in order to filter out the harmonics at f_s), the cutoff frequency must fullfill the relation:

$$f_{cutoff} \ll f_s \tag{5.15}$$

The value chosen is $f_{cutoff} = 200Hz$, which gives $C_{buck} = 132\,\mu F$.
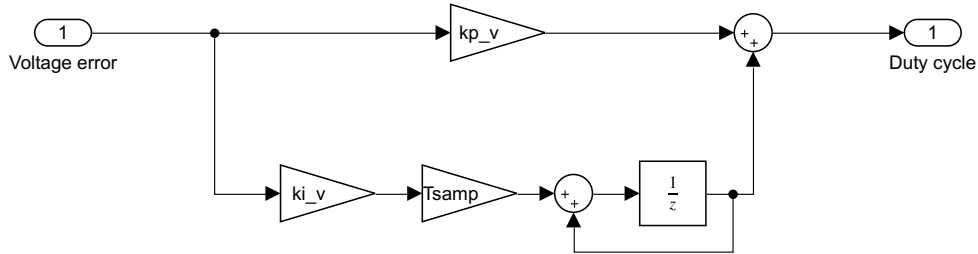
Figure 5.17: Details about the PID converter

To tune the controller, proper values of k_p and k_i must be defined. This is done by deriving the linearized transfer function of the converter through state space modelling. The state space averaged model is defined through the calculation of the relations between the inputs u of the system (input voltage, duty cycle), the states x (inductor current, capacitor voltage) and the outputs y (output voltage):

$$\begin{cases} \frac{\mathrm{d}x}{\mathrm{d}t} = A\,x + B\,u \\ y = C\,x + D\,u \end{cases} \tag{5.16}$$

Then, the linearised transfer function for the modelled system becomes:

$$P(s) = C(sI - A)^{-1}B + D \tag{5.17}$$

where I is the identity matrix. For the buck converter, the expressions for A, B, C, D are:

$$A = \begin{bmatrix} 0 & -\frac{1}{L_{bus}} \\ \frac{1}{C_{bus}} & -\frac{1}{R_l C_{buck}} \end{bmatrix} \tag{5.18a}$$

$$B = \begin{bmatrix} \frac{V_{in}}{L_{buck}} & 0 \end{bmatrix} \tag{5.18b}$$

$$C = \begin{bmatrix} 0 & 1 \end{bmatrix} \tag{5.18c}$$

$$D = \begin{bmatrix} 0 \end{bmatrix} \tag{5.18d}$$

The Bode plot of $P(s)$ is showed in figure 5.18a.

To design the controller, the open loop response $C(s)P(s)$ must be analysed, where $C(s)$ is the transfer function of the feedback controller, which is:

$$C(s) = \frac{Output}{error} = K + \frac{K\,\omega_i}{s} = K\,\frac{s + \omega_i}{s} \tag{5.19}$$

So the proportional controller has a gain of $k_p = K$, the integral one has a gain of $k_i = K\,\omega_i$. The bode plot of a PI controller with $K = 0.001$ and $\omega_i = 2\,\pi\,400$ is showed in figure 5.18b.

The controller must be tuned in order to achieve the stability of the system. Two quantities are used in order to make a controlled system stable, referred to the open loop response $C(s)P(s)$:

(a) Buck Converter

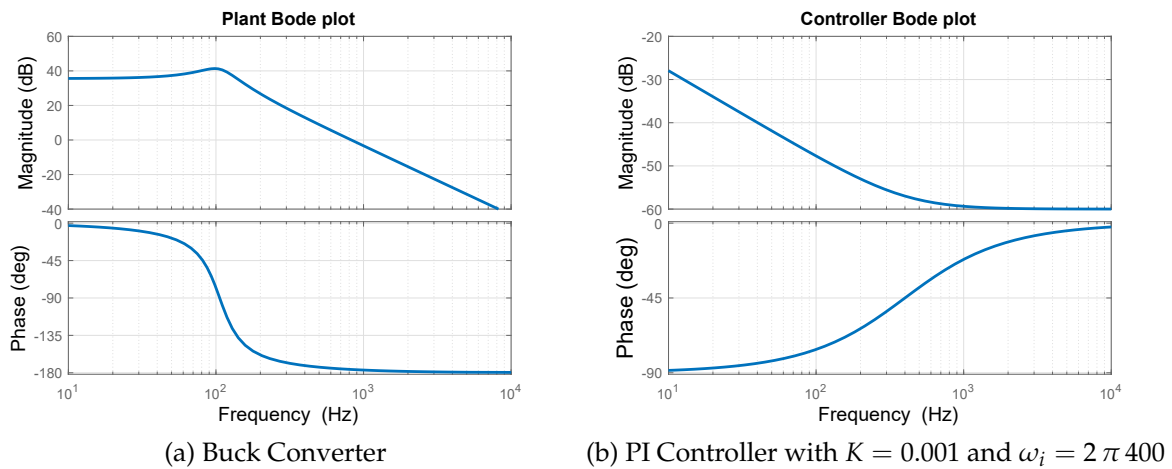(b) PI Controller with $K = 0.001$ and $\omega_i = 2\,\pi\,400$

Figure 5.18: Bode plots for the plant (buck converter) and the PI controller

- phase margin: it is the angle between the transfer function $C(s)P(s)$ and -180° at 0 db crossing.
- gain margin: distance between 0 dB and transfer function $C(s)P(s)$ at point where -180° of phase is crossed.

Usually, control systems are designed in such a way that phase margin $> 30°$ and gain margin $> 6\,db$. With $K = 0.001$ and $\omega_i = 2\,\pi\,400$, for this system the phase margin is $\approx 85°$ and gain margin $\approx 7\,db$, as can be seen in figure 5.19. Consequently,the chosen values are: $k_p = K = 0.001$, $k_i = K\,\omega_i = 2.51$.
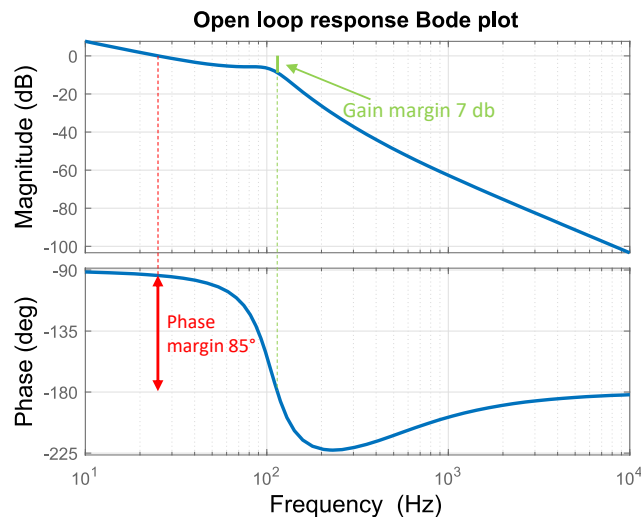
Figure 5.19: Bode plot for the open loop response of the system

As already mentioned, the output voltage have been set at 13 V. The designed control have been implemented in the model showed in figure 5.16 and the results can be seen in the following pictures. In figure 5.20a is showed how the duty cycle varies with the time: when the switching frequency is 20 kHz, for example, the value reached at steady state regime is D=0.16, because of

the high DC bus voltage. On the other hand, at high $f_s = 50\,kHz$, the DC bus voltage is 47 V and the duty cycle needed to obtain $V_l = 13V$ is 0.26.

METTERE I NUMERI CHE è MEGLIO

(a) Duty cycle

(b) Load voltage

(c) DC bus voltage for different power levels

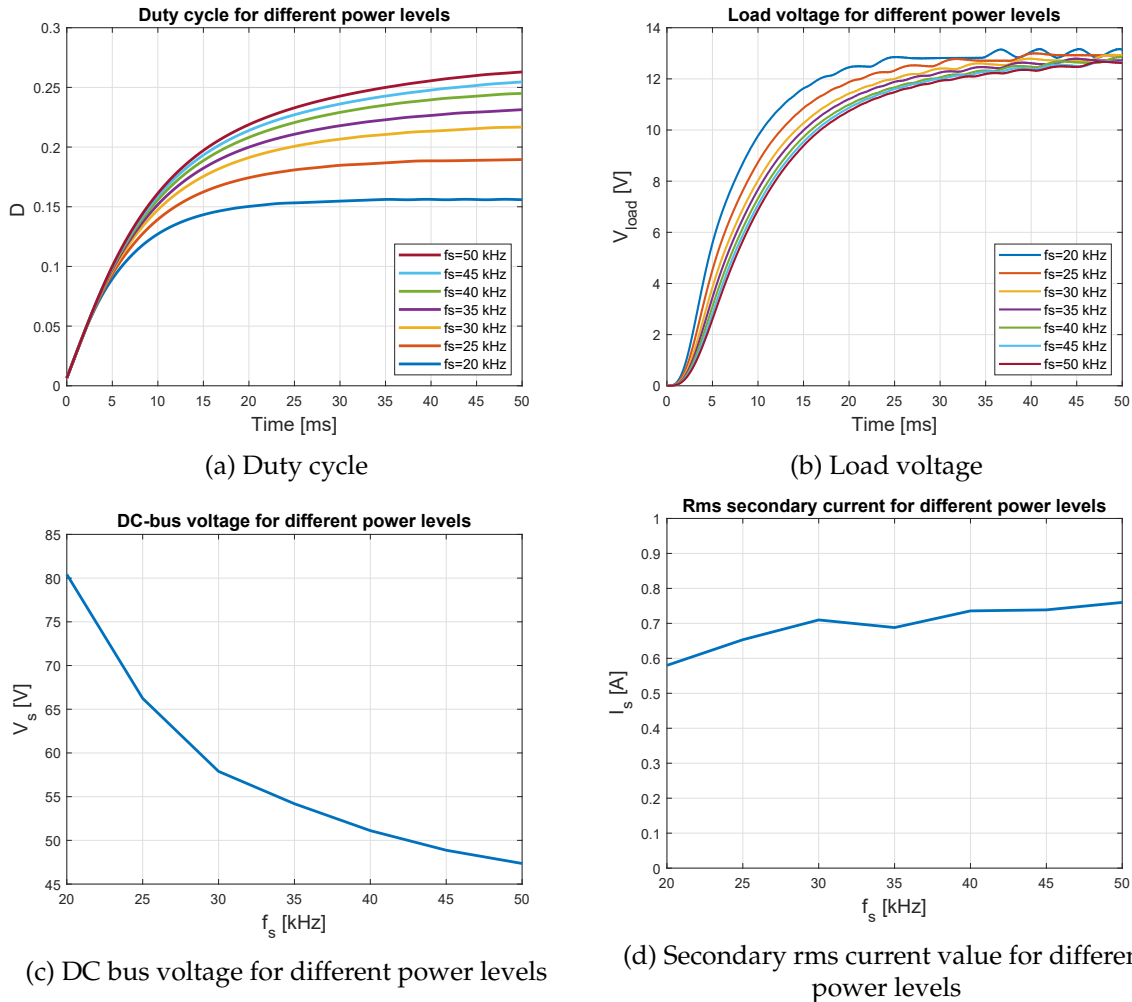(d) Secondary rms current value for different power levels

Figure 5.20: Results from the symulink model of the smart pot system, with a focus on the controlled buck converter, $R_l = 6\,\Omega$

The figures show good response of the system to the controller, with no overshoot, and this is the result obtained by means of sufficient gain and phase margins.

The size of the Litz wire used in the secondary coil is determined taking into account the rms value of the secondary current. As can be seen in figure 5.20d, the maximum is 0.8 A. Litz wire in the primary inductor are usually loaded to a current density that is around $7 - 10 \frac{A}{mm^2}$. In the secondary coil, the load must be reduced due to the fact that the wires are very close to the bottom part of the pot which can reach very high temperature. From [28] several litz wire types are listed. For this situation a possible wire that can be chosen has the following characteristics:

- Circular cross section, external diameter 0.94 mm

- Equivalent gauge 22: the effective conductor cross section area is 0.326 mm^2

- 27 strands, each with 0.127 mm diameter.

- DC Resistance 16.3 $\frac{\Omega}{MFT} = 53.4 \frac{m\Omega}{m}$

With such wire, the maximum current density is then $\frac{0.8}{0.326} = 2.5 < 7 \frac{A}{mm^2}$.

If the only load to supply is the vacuum pump, the load seen by the buck converter is $R_l = \frac{V_l}{I_{pump}} = \frac{13}{0.65} = 20\Omega$. The simulation results with this different load can be seen in figure 5.21.
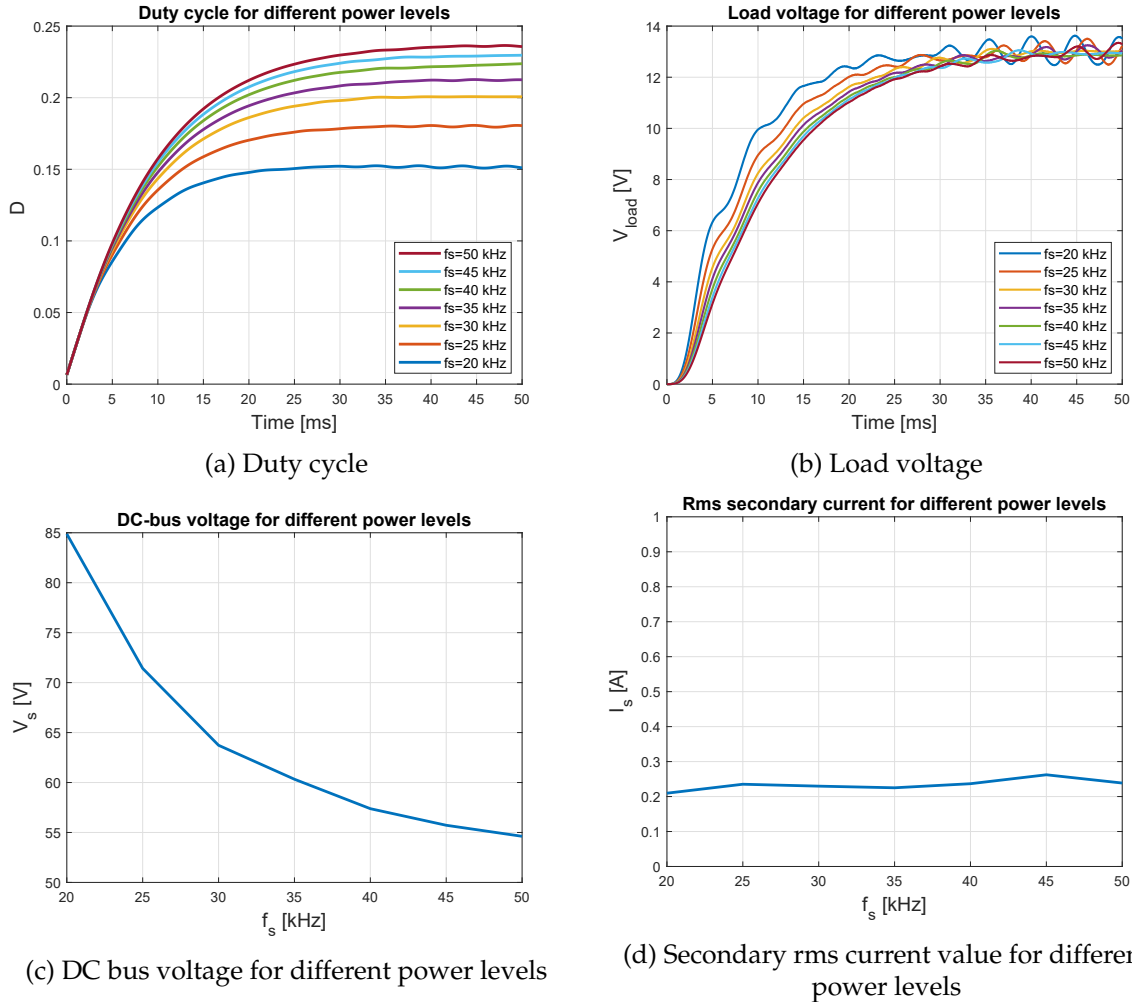

(a) Duty cycle

(b) Load voltage

(c) DC bus voltage for different power levels

(d) Secondary rms current value for different power levels

Figure 5.21: Results from the symulink model of the smart pot system, with a focus on the controlled buck converter, $R_l = 20\,\Omega$

Since in this case $R_l = 20\,\Omega$, the duty cycle range vary from 0.15 to 0.24 and the DC bus voltage from 80 to 47, compared to the range 0.16-0.26 and 85-55 V obtained for $R_l = 16\,\Omega$.

5.6   Conclusions

In this chapter a circuital model of the smart pot have been provided and validated. The results are very accurate, even if the parameters of the circuit must be mapped (with a fem simulation) due to their high saturation dependency. Also the design of a DC/DC buck converter together with a PI controller have been showed. The concept of the smart pot can be applied to the supply of a broad set of different loads: mixers, infrared lights, vacuum pumps.
Generally talking, the more is the power transferred to the auxiliary device, the less is the heat

generated in the pot. With the theory developed in this chapter, 500 W that can be needed to supply an infrared lamp can be achieved by increasing the number of turns to 20 and putting an adequate secondary resonant capacitor C_s that in this case is useful due to the consistent currents. On the other hand, a battery with more capacity must be included due to the resricted range of frequency where the 500 W are achieved. In general it is always better to increase the coil voltage and then decrease it by means of a buck converter, in order to have low currents flowing in the hottest part of the pan and keep a low wire cross section.

Another thing to explain is that if the bottom of the pan is bigger than the inductor in the hob, the amount of magnetic flux linked with the secondary coil drastically decrease and so the power transfer capabilities of the system, because all the magnetic flux is linked with the pot. So the pan mustn't be larger than the inductor if the auxiliary devices require more than 100 W.

Chapter 6

Remarks and future trends

Among the conclusions and overall considerations that have been written at the end of each chapter, some remarks must be given. The FEM model made of the induction-pot system is 2D axial-symmetric. This is accurate to model the inductor and the pot, but not the ferrite. In fact, the ferrite that is placed below the inductor comes in form of bars that are radially placed around the centre of the inductor, as can be seen in figure 6.1. This effect can be perfectly modelled only through a 3D simulation. However, the system behaviour shown in this thesis as well as the methodologies developed are still valid. The error is only about few percent in the parameters such as L_{eq} and R_{eq}.

Figure 6.1: View of the bottom part of the inductor where the ferrite bars are placed

The difference between having a disc of ferrite or bars is that the bars have a slightly lower flux concentration effect. So the power induced in the pot is less compared to the 2D axial-symmetric case.

The metodologies developed throughout the chapters, allow to deeply model and analyse the behaviour of the system, since all the possible cause of parameters variation have been taken into account.

Multiple research trends in induction cooking are still being developed, in a varied field of different aspects [1]:

- the efficiency of the power electronic stages can still be upgraded by means of direct ac-ac conversion of the power and high efficiency converter [29], [30];
- heating of high-conductivity non magnetic materials such as aluminium or copper [31];

- new adaptive control strategies, to control not only the output power but also the pot temperature [32];
- flexible cooking surface technology: in the total active surface concept the user can place any pot, with any shape, anywhere in the cooking surface [33]. A special effort is required to design multiple-output power converters and compact coils. In figure 6.2 an overview of such technology can be seen.
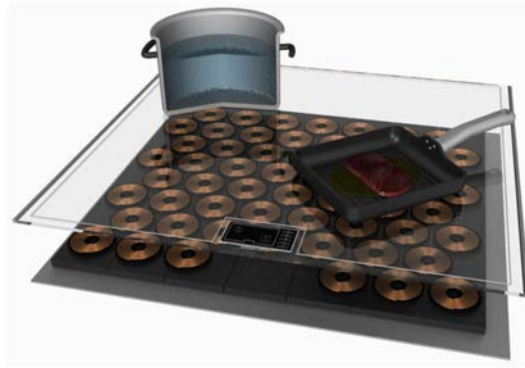

Figure 6.2: Total active surface concept overview [33]

Bibliography

[1] O. Lucía, P. Maussion, E. J. Dede, and J. M. Burdío, "Induction heating technology and its applications: Past developments, current technology, and future challenges," *IEEE Transactions on Industrial Electronics*, vol. 61, pp. 2509–2520, May 2014.

[2] H. W. Ott, *Electromagnetic Compatibility Engineering*. John Wiley and Sons Inc., 2009.

[3] F. Luo, D. Boroyevich, P. Mattevelli, K. Ngo, D. Gilham, and N. Gazel, "An integrated common mode and differential mode choke for emi suppression using magnetic epoxy mixture," in *2011 Twenty-Sixth Annual IEEE Applied Power Electronics Conference and Exposition (APEC)*, pp. 1715–1720, March 2011.

[4] N. Mohan, T. M. Undeland, and W. P. Robbins, *Power electronics*. Hoepli, 2005.

[5] J. Acero, J. M. Burdio, L. A. Barragan, D. Navarro, R. Alonso, J. Ramon, F. Monterde, P. Hernandez, S. Llorente, and I. Garde, "Domestic induction appliances," *IEEE Industry Applications Magazine*, vol. 16, pp. 39–47, March 2010.

[6] H. Sarnago, O. Lucía, A. Mediano, and J. M. Burdío, "High-efficiency power converters for domestic induction heating applications," in *IECON 2012 - 38th Annual Conference on IEEE Industrial Electronics Society*, pp. 3268–3273, Oct 2012.

[7] J. Jittakort, S. Yachiangkam, and S. Kleangsin, "The implementation of the full bridge inverter for the series resonant load," in *2014 11th International Conference on Electrical Engineering/Electronics, Computer, Telecommunications and Information Technology (ECTI-CON)*, pp. 1–4, May 2014.

[8] D. V. Bhaskar and N. Vishwanathan, "Full bridge series resonant inverter for induction cooking application," in *2012 IEEE 5th India International Conference on Power Electronics (IICPE)*, pp. 1–5, Dec 2012.

[9] J. Tian, G. Berger, T. Reimann, M. Scherf, and J. Petzoldt, "A half-bridge series resonant inverter for induction cookers using a novel fpga-based control strategy," in *2005 European Conference on Power Electronics and Applications*, pp. 9 pp.–P.9, Sept 2005.

[10] H. W. Koertzen, J. D. van Wyk, and J. A. Ferreira, "Design of the half-bridge, series resonant converter for induction cooking," in *Proceedings of PESC '95 - Power Electronics Specialist Conference*, vol. 2, pp. 729–735 vol.2, June 1995.

[11] J. Avellaned, C. Bernal, A. Otin, P. Molina, and J. M. Burdio, "Half-bridge resonant inverter with sic cascode applied to domestic induction heating," in *2013 Twenty-Eighth Annual IEEE Applied Power Electronics Conference and Exposition (APEC)*, pp. 122–127, March 2013.

[12] A. Beato, C. Bocchiola, and S. Frattesi, "Modelling and design of the half-bridge resonant inverter for induction cooking application," in *2006 14th Mediterranean Conference on Control and Automation*, pp. 1–6, June 2006.

[13] H. W. E. Koertzen, J. A. Ferreria, and J. D. van Wyk, "A comparative study of single switch induction heating converters using novel component effectivity concepts," in *PESC '92 Record. 23rd Annual IEEE Power Electronics Specialists Conference*, pp. 298–305 vol.1, June 1992.

[14] A. Spagnolo, *Auto-adaptive multi-coil inductors for transverse flux induction heating of metal strips*. PhD thesis, University of Padua, 2010.

[15] M. Adler, "A field-theoretical approach to magnetic induction heating of thin circular plates," *IEEE Transactions on Magnetics*, vol. 10, pp. 1118–1125, December 1974.

[16] S. Lupi, "The calculation of planar circular coils for the induction heating of bimetalliic plates," *Archiv für Elektrotechnik*, vol. 60, pp. 313–318, Nov 1978.

[17] J. P. C. Smeets, *Contactless transfer of energy : 3D modeling and design of a position-independent inductive coupling integrated in a planar motor*. PhD thesis, Technische Universiteit Eindhoven, 2015.

[18] A. S. for Metals, "Properties and selection: Stainless steels, tool materials and special-purpose metals," *Metals Handbook Ninth Edition*, vol. 3, pp. 597–614, 1980.

[19] O. Lucia, J. M. Burdio, I. Millan, J. Acero, and D. Puyal, "Load-adaptive control algorithm of half-bridge series resonant inverter for domestic induction heating," *IEEE Transactions on Industrial Electronics*, vol. 56, pp. 3106–3116, Aug 2009.

[20] O. Lucía, J. M. Burdío, I. Millán, J. Acero, and L. A. Barragán, "Efficiency-oriented design of zvs half-bridge series resonant inverter with variable frequency duty cycle control," *IEEE Transactions on Power Electronics*, vol. 25, pp. 1671–1674, July 2010.

[21] O. Lucia, H. Sarnago, D. Boroyevich, P. Mattavelli, and F. C. Lee, "Optimal trajectory control for series resonant converters applied to domestic induction heating," in *2013 Twenty-Eighth Annual IEEE Applied Power Electronics Conference and Exposition (APEC)*, pp. 2534–2540, March 2013.

[22] N. Park, D. Lee, and D. Hyun, "A power-control scheme with constant switching frequency in class-d inverter for induction-heating jar application," *IEEE Transactions on Industrial Electronics*, vol. 54, pp. 1252–1260, June 2007.

[23] I. Millan, D. Puyal, J. M. Burdio, C. Bemal, and J. Acero, "Improved performance of half-bridge series resonant inverter for induction heating with discontinuous mode control," in *APEC 07 - Twenty-Second Annual IEEE Applied Power Electronics Conference and Exposition*, pp. 1293–1298, Feb 2007.

[24] "Unipd patent database, https://www.unipd.it/en/research/results-research/patents."

[25] "https://www.amazon.it/yosoo%c2%ae-dc12-80-kpa-della-miniatura/dp/b00vptiqw4."

[26] "https://www.ebay.it/itm/pacco-batteria-a-litio-ricaricabile-12v-3ah-celle-aaa-caricabatterie-12v-0-5ah-/272292124724."

[27] *Inductor calculation for buck converter*. Rohm semiconductor, 2012.

[28] *Litz wire - technical information*. New England wire technologies.

[29] H. Sarnago, O. Lucía, A. Mediano, and J. M. Burdío, "High-efficiency power converters for domestic induction heating applications," in *IECON 2012 - 38th Annual Conference on IEEE Industrial Electronics Society*, pp. 3268–3273, Oct 2012.

[30] H. Sarnago, A. Mediano, and . Lucia, "High efficiency ac–ac power electronic converter applied to domestic induction heating," *IEEE Transactions on Power Electronics*, vol. 27, pp. 3676–3684, Aug 2012.

[31] A. Fujita, H. Sadakata, I. Hirota, H. Omori, and M. Nakaoka, "Latest developments of high-frequency series load resonant inverter type built-in cooktops for induction heated all metallic appliances," in *2009 IEEE 6th International Power Electronics and Motion Control Conference*, pp. 2537–2544, May 2009.

[32] D. Paesa, C. Franco, S. Llorente, G. Lopez-Nicolas, and C. Sagues, "Adaptive simmering control for domestic induction cookers," *IEEE Transactions on Industry Applications*, vol. 47, pp. 2257–2267, Sep. 2011.

[33] H. Sarnago, J. M. Burdío, and . Lucía, "High-performance and cost-effective zcs matrix resonant inverter for total active surface induction heating appliances," *IEEE Transactions on Power Electronics*, vol. 34, pp. 117–125, Jan 2019.